Control-Structure Interaction

Nonlinear coupling of flexible structure and power hydraulic system.

Gabriel Follet

Delft University of Technology

TU Delft

Control-Structure Interaction

Nonlinear coupling of flexible structure and power hydraulic system.

by

Gabriel Follet

to obtain the degree of Master of Science
at the Delft University of Technology,
to be defended publicly on September 24th, 2025

Student number: 6073654
Project duration: February 12, 2025 – September 24, 2025
Thesis committee:

Prof.dr. A.V. Metrikine ,	TU Delft, Chair
Dr. A. Tsetas,	TU Delft, Supervisor
Dr. A. Cabboi,	TU Delft, Evaluation Committee

Cover: Image credit:https://www.crosswindhkn.nl/news/2023/01/faunaguard-and-bubble-curtain

An electronic version of this thesis is available at http://repository.tudelft.nl/.

TU Delft

Preface

Quiero agradecer enormemente a mi familia por todo el apoyo incondicional que me dieron a lo largo de este proceso, desde la decisión de hacer un magíster, hasta el hecho de hacerlo a más de 10.000 kilómetros de ustedes. Aunque estábamos lejos, su motivación, apoyo y amor siempre estuvieron cerca y me acompañaron en todo momento.

En especial, quiero agradecer a mi papá Philippe y a mi mamá Pamela, por la confianza que siempre tuvieron en mí. Esa fe fue mi principal fuente de motivación durante estos dos años. Sin ustedes, no habría sido posible.

Gabriel Follet
Delft, September 2025

Summary

The growing number and increasing size of Offshore Wind Turbines (OWTs) in Europe have raised significant challenges for monopile foundation design. As turbines become larger and are installed in deeper waters, structural demands and foundation requirements have also increased. Additionally, stricter noise regulations have been established, limiting the use of traditional impact driving techniques and further increasing the complexity of installation procedures.

To address these challenges, vibratory methods like Gentle Driving of Piles (GDP) have recently gained traction. However, when powered by hydraulic shakers, they can experience dynamic coupling with the structure, which interferes with both the generation and control of the vibrations needed for effective driving.

To this end, a nonlinear model incorporating the dynamic interactions between the electrical, hydraulic, and structural subsystems has been developed. A parametric study was conducted to determine the minimum pressure required to operate and control the structure when utilizing a PID-based control system.

It was determined that the primary nonlinear dynamic behavior was due to the velocity-pressure coupling and its impact on the nonlinear flow. To address this, a controller was designed that effectively mitigated these effects. Specifically, it was found that the supply pressure could be reduced by up to 25% while still maintaining effective sinusoidal displacement control. Additionally, the conditions under which synchronization between the shaker-structure could occur were identified, along with ways to avoid this phenomena, as synchronization can lead to system damage and a loss of control authority over the structure.

This study demonstrates the effectiveness of using a PID controller to reduce the coupling between subsystems, thereby enhancing the efficiency of vibratory pile driving methods, promoting their use in monopile installation.

Contents

List of Figures

List of Tables

Nomenclature

Abbreviations

Abbreviation	Definition
CFD	Computational Fluid Dynamics
CPT	Cone Penetration Test
DAE	Differential Algebraic Equation
DAQ	Data Acquisition
EKF	Extended Kalman Filter
FEM	Finite Element Method
FFT	Fast Fourier Transform
FRF	Frequency Response Function
GDP	Gentle Driving of Piles
HPU	Hydraulic Power Unit
IAE	Integral of Absolute Error
KF	Kalman Filter
LTI	Linear Time Invariant
MIMO	Multiple-Inputs Multiple-Output
MDOF	Multiple Degree of Freedom
ODE	Ordinary Differential Equation
OWT	Offshore Wind Turbine
PDE	Partial Differential Equation
PID	Proportional Integral Derivative
P-C	Predictor-Corrector
Re	Reynolds Number
SDOF	Single Degree of Freedom
SISO	Single Input - Single Output
THD	Total Harmonic Distortion
TF	Transfer function

Symbols

Symbol	Definition	Unit
A_A	Piston face area in chamber A	[mm]
A_B	Piston face area in chamber B	[mm]
A_{emb}	Embedded area of structure in soil	[m^2]
b_L	Hydraulic system damping coefficient	[Ns/m]
b_{DZ}	Spool valve dead-zone threshold	[%]
c	Arbitrary constant	[-]
C_1	Linear valve geometry gradient coefficient	[-]
C_{eq}	Equal percentage geometry coefficients	[-]
d_Q	Value of $1-\eta$ at which spline is fitted	[-]
i	Current	[mA]
K	Arbitrary gain	[-]
K_{aw}	Anti Windup gain	[-]
K_{comp}	Flow compensator gain	[-]
K_e	Flow-Force rate gain	[mm^3/s/N]

Symbol	Definition	Unit
K_{ff}	Feedforward gain	[-]
K_{iU}	Current gain	[mA/V]
K_l	Flow-Force gain	[mm^3/N]
K_q	Flow gain	[mm^{3}s/%]
$K_{ix_{sp}}$	Spool valve gain	[%/mA]
k_L	Piston stiffness	[N/m]
L	Solenoid Inductance	[H]
L_L	Actuator chamber length	[mm]
L_{emb}	Embedded length	[m]
m_L	Piston mass	[kg]
p	Fluid pressure scalar field	[Pa]
P	Pressure drop across piston chambers	[MPa]
P_{atm}	Atmospheric pressure	[MPa]
P_A	Pressure in chamber A	[MPa]
P_B	Pressure in chamber B	[MPa]
P_b	Load back-pressure	[MPa]
P_r	Return pressure	[MPa]
P_s	Supplied pressure	[MPa]
P_{struct}	Perimeter of structure cross section	[m]
Q	Flow across valve	[mm3/s]
Q_{Tanh}	Tanh backflow modifier	[-]
Q_{spline}	Spline backflow modifier	[-]
t	Time	[s]
U	Voltage signal	[V]
U_{ff}	Feedforward voltage signal	[V]
U_{sat}	Saturated control signal	[V]
V_A	Volume of piston chamber A	[mm^3]
V_{A0}	Volume of piston chamber A at $x_{sp} = 0$	[mm^3]
V_B	Volume of piston chamber B	[mm^3]
V_{B0}	Volume of piston chamber A at $x_{sp} = 0$	[mm^3]
V_L	Total volume of piston chambers	[mm^3]
x_L	Piston displacement	[m]
x_{sp}	Valve opening	[%]
x'_{sp}	Deadband-affected valve opening	[%]
x''_{sp}	Actual valve opening	[%]
$\mathbf{u}$	Fluid velocity vector	[m/s]
$\mathbf{f}$	Body forces acting on fluid	[m/s^2]
$\mathbf{x}$	Structural degrees of freedom	[m,rads]
$\mathbf{x_u}$	Translational degrees of freedom	[m]
$\mathbf{x}_\varphi$	Rotational degrees of freedom	[rads]
$\mathbf{C}$	Structure damping matrix	[N/m/s]
$\mathbf{F}_{fr}$	External Friction Force Matrix	[N]
$\mathbf{K}$	Structure stiffness matrix	[N/m]
$\mathbf{M}$	Structure mass matrix	[kg]
$\mathbf{\Psi}$	Mode Matrix	[-]
α	Pressure supply factor	[-]
β_e	Oil bulk modulus	[N/m^2]
β_Q	Back flow tanh coefficient	[mm^3]
Δ_b	Backlash gap	[%]
ρ	Fluid density	[kg/m^3]
ρ_{struct}	Structure material density	[kg/m^3]
$\hat{\rho}(x, y)$	Pearson correlation coefficient between x and y	[-]
ϱ	Embedded length ratio	[-]
μ	Fluid dynamic viscosity	[Pa· s]

Symbol	Definition	Unit
μ_m	Mass ratio	[-]
η	Ratio of cylinder pressure to supplied pressure	[-]
η_{total}	Total power efficiency of the system	[-]
τ	Arbitrary time constant	[s]
$\tau_{\text{catch-up}}$	Backlash catch up time	[s]
τ_{Kd}	Filtered derivative time constant for PID	[s]
τ_{iU}	Voltage-Current delay	[s]
$\tau_{ix_{sp}}$	Current-Spool valve delay	[s]

Operators, Logical symbols & Others

Symbol	Definition
$\mathbb{Z}$	Set of the Integers
$\mathcal{L}$	Laplace Transform
$\Re$	Real Part Operator
$\Im$	Imaginary Part Operator
$\mathcal{Z}$	Z-Transform
$\mathcal{F}$	Fourier Transform
∇	Gradient Operator
$\mathcal{D}_{filtered}$	Laplace transform of the derivative action
$\mathcal{E}$	Laplace Transform of the error/residual signal
∇^2	Laplacian
$\mathcal{J}$	Jacobian
$*$	Convolution operator
$\propto$	Linearly proportional to
$\partial/\partial x$	Partial derivative with respect to x
$\int$	Integral operator. May represent single or multiple integrals, as indicated by the differential (e.g., dx, dA, dV)
$\angle$	Angle of complex number
$H(t)$	Heaviside function

1

Introduction

1.1. Context

Europe's growing energy demands, along with current shift towards renewable energy sources required to meet current climate goals [1], have led to the rapid expansion of offshore energy production, predominantly through the use of Offshore Wind Turbines (OWTs) [2].

Given the wide variety of site conditions, met-ocean environments, and project-specific constraints, there is not a universal solution for selecting and installing OWT. Instead, foundation selection is decided on a case-by-case basis using Multi-Criteria Decision Analysis (MCDA), which incorporates factors such as structural performance, installation complexity, cost, logistics and noise pollution [3, 4]. Among all types of foundations, bottom-fixed OWTs, in particular monopile systems are currently the dominant solution within Europe [5].

Offshore wind turbines (OWTs) are getting larger and are being installed in deeper waters [6, 7]. This trend creates major challenges for both the design and installation of monopile foundations. As turbine size and water depth increase, so do the structural demands and associated costs. Foundation systems alone can account for up to 30% of the total structural cost [8], making them a critical focus for optimization.

Impact driving is the most common technique used to install monopile foundations. However, recent studies have shown that the noise generated during pile driving can permanently harm marine ecosystems [9, 10]. In response, several European countries have implemented strict regulations and noise thresholds for offshore pile installation [11]. Noise reduction during pile installation can be achieved through two main approaches [9]. The first, involves mitigation strategies, such as bubble curtains, pile casings, or noise-reduction screens [12, 13]. The second approach, is to use non-impact driving techniques, such as vibratory driving [14, 15].

Traditional vibratory driving methods typically use axial vibrations [16, 17]. However, their application in offshore environments has been limited, largely due to the lack of predictive models for installation performance and post-installation assessment [18].

A recently proposed technique for monopile installation is Gentle Driving of Piles (GDP), which applies high-frequency torsional and low-amplitude axial vibrations [19]. A key benefit of using torsional vibrations is that they produce shear waves, which do not propagate in water. As a result, this method significantly reduces underwater noise emissions during installation [20].

The working mechanisms and theoretical models behind GDP have been described in recent literature [21], and preliminary tests have demonstrated promising drivability [22] and post-installation capacity [23]. Despite initial successes, a key limitation of the Gentle Driving of Piles technique is the challenge of generating and transmitting torsional vibrations to the pile in an effective, reliable, and efficient manner [24]. Specifically, shaker systems that rely on counter-rotating masses often experience frequency–amplitude coupling, which restricts the range of frequencies and amplitudes necessary for optimal pile

driving performance [25]. Furthermore, the use of GDP in offshore environments introduces additional constraints on shaker design, including the need for high reliability, compactness, reduced weight, and low power consumption.

1.2. Research Problem

Building on the context outlined above, this research focuses on modeling the coupling between a structure and the excitation system (shaker). The aim is to explore the interactions that occur when a harmonically excited structure influences the system driving it. By understanding these dynamics, we can better address the challenges associated with efficient and reliable pile driving in offshore environments.

Two primary methods exist for exciting a structure:

- **Indirect forcing:**
  In this method, a shaker is rigidly attached to the structure and itself starts to vibrate, typically through counter-rotating masses. Due to the rigid mechanical coupling, the structure responds to the inertial forces generated by the shaker and vibrates in sync with the shaker. Although effective, this method has some challenges, often arising from the interface between the shaker and the structure, particularly with respect to the efficient transfer of inertial forces. Moreover, counter-rotating mechanisms are limited in bandwidth and dynamic responsiveness, especially in terms of acceleration, amplitude and jerk
- **Direct forcing:**
  In this approach, the shaker produces a force that is directly applied to the structure. Depending on requirements such as power, robustness or controllability, the excitation force can be generated using either electromagnetic or power-hydraulic systems.

This study focuses on the latter method, *Direct Forcing using a Power-Hydraulic System*. Particular emphasis is placed on the coupling effects that arise between the hydraulic actuator and the structure, specifically due to the pressure and velocity feedback imparted by the structure onto the hydraulic system.

These coupling effects are often neglected in civil engineering, as the force-producing systems are typically much stronger and stiffer than the structures they excite. As a result, the force-generating systems and the forces they produce are usually treated as independent systems, with the forces being considered as prescribed. Moreover, the dynamic excitation of structures is typically limited to linear and quasi-static regimes, where such coupling interactions are minimal and can be ignored.

Although hydraulic power systems are inherently nonlinear, quasi-linear behavior can be achieved by oversizing the system. However, given the constraints outlined earlier, oversizing is not a feasible option. As a result, coupling between the structure and the shaker will occur, causing the system's response to remain inherently nonlinear. This directly conflicts with the harmonic displacement used in GDP technology. Therefore, implementing a control scheme capable of managing the system's nonlinear behavior becomes essential [21].

Similar challenges arise in fields such as aerospace and mechanical engineering. However, the specific demands of structural engineering such as model reliability, instrumentation limitations, cost, weight, and required force magnitudes make the challenges associated with this problem unique. Therefore, a focused investigation from a structural engineering perspective is essential to adequately address these particular needs.

While this research is motivated by the vibratory driving of monopiles for offshore wind turbines, its findings are broadly applicable to any system involving a flexible structure coupled with a power-hydraulic system.

1.3. Objectives and scope

The research gap addressed in this thesis arises from the lack of consistency and consensus regarding modeling assumptions and techniques, particularly when applying principles of civil engineering and structural dynamics to complex, multidisciplinary problems such as the one explored here. The problem

at hand requires the integration of models and techniques from power hydraulics and control theory, which may be unfamiliar to civil engineers. Therefore, this work will be structured as follows:

Firstly, concepts, models and techniques that may not be commonplace in civil engineering will be introduced and explained; secondly, commonly used assumptions will be reviewed and their relevance and validity will be assessed; and finally, these models and techniques will be applied to the problem at hand.

As it was previously mentioned, the the system to be studied consists of three interacting subsystems, as shown in Figure 1.1.

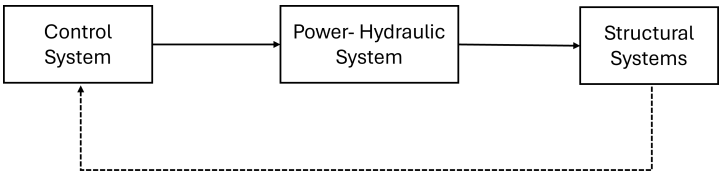

Figure 1.1: High level overview of coupled system

Each subsystem is described and modeled based on the characteristics of its individual components. Since these subsystems exhibit distinct dynamics, a clear understanding of the underlying assumptions and component behavior is crucial for analyzing the overall coupled system.

A pragmatic approach will be adopted throughout this thesis. Rather than reinterpreting concepts from other disciplines into the structural dynamics framework or re-explaining well-established techniques, this work focuses on identifying the relevant methods and models, providing concise explanations, and applying them effectively.

Therefore, the main question this work seeks to answer is.

What dynamic phenomena arises from the coupling of a flexible structure with a power hydraulic system

Additionally, the following sub-questions will also be tackled

- What are the sources of the nonlinear behaviors, how can they be minimized?
- How does the system behave near resonance? Can the system be controlled when the structure is in resonance?
- What is the minimum control strategy needed to achieve a harmonic response over a range of frequencies and amplitudes.

1.4. Thesis Outline

This thesis is organized into 5 chapters, following an inductive structure where each chapter builds upon the previous one. A brief summary of each chapter is provided below:

- **Chapter 1: Introduction**
  Introduces the broader context, motivation, and scope of the research. It formulates the main problem, defines the system under study, and outlines the research objectives and methodological approach.
- **Chapter 2: Framework**
  Presents the mathematical methods, notation, and theoretical frameworks used throughout the thesis. This includes modeling approaches for the power-hydraulic system, structural subsystem, and control system, focusing on their individual characteristics and interactions.
- **Chapter 3: Dynamics of the Coupled System** This chapter analyzes the dynamics of the coupled system. It explores various modeling assumptions and compares simplified versus more complex models to gain a deeper understanding of the system's response.

- **Chapter 4: Results**
  This chapter focuses on the design and implementation of control strategies for the coupled system. It investigates how closed-loop control can achieve the desired harmonic responses while managing nonlinearities and coupling effects.

  The presentation is structured as follows: first, the open-loop responses of the systems are analyzed to establish a baseline response. This is followed by the closed-loop results, where the performance, effectiveness and limitations of the implemented control strategies is presented and analyzed.
- **Chapter 5: Conclusion**
  Summarizes the key findings, reflects on the results, and discusses their implications. This chapter also provides recommendations for future research and practical applications.

2

Framework

This chapter presents the foundational concepts, mathematical tools, and theoretical models that underpin the work presented on this thesis. It introduces the notation and conventions used, and presents the key frameworks for modeling the power-hydraulic system, the structural dynamics, and control system. By providing a clear and consistent framework, this chapter lays the groundwork for the subsequent analysis of the coupled system and its control.

2.1. Mathematical Framework

This section presents the fundamental mathematical principles, definitions, and notation employed throughout the thesis. Since this work lies at the intersection of multiple engineering disciplines, each with its own notation and terminology, it is essential to clearly and explicitly define the key concepts, assumptions, and nomenclature that will be adopted throughout the thesis. Additionally, this section will serve as a reference point for commonly used concepts, enabling concise explanations elsewhere by referring back to this established framework.

2.1.1. Linear Time-Invariant System

A system is said to be **Linear Time-Invariant** (LTI) if it satisfies two key properties:

- **Linearity**: The response to a linear combination of inputs is the same linear combination of the individual responses.
- **Time-Invariance**: The system's behavior does not change over time; a time-shifted input produces a time-shifted output.

In the time domain, a continuous-time LTI system is typically represented using the convolution integral:

$$y(t) = (h * u)(t) = \int_{-\infty}^{\infty} h(\tau)u(t-\tau)\,d\tau \tag{2.1}$$

where $h(\tau)$ is the system's impulse response and $u(t)$ is the input.

2.1.2. State-Space Systems

A common way to model LTI systems is through the **State-Space** representation, which is defined by:

$$\dot{\mathbf{x}}(t) = \mathbf{A}\mathbf{x}(t) + \mathbf{B}\mathbf{u}(t), \tag{2.2}$$

$$\mathbf{y}(t) = \mathbf{C}\mathbf{x}(t) + \mathbf{D}\mathbf{u}(t), \tag{2.3}$$

where:

- $\mathbf{x}(t) \in \mathbb{R}^n$: State vector
- $\mathbf{u}(t) \in \mathbb{R}^m$: Input vector

- $\mathbf{y}(t) \in \mathbb{R}^p$: Output vector
- $\mathbf{A} \in \mathbb{R}^{n \times n}$: System matrix
- $\mathbf{B} \in \mathbb{R}^{n \times m}$: Input matrix
- $\mathbf{C} \in \mathbb{R}^{p \times n}$: Output matrix
- $\mathbf{D} \in \mathbb{R}^{p \times m}$: Feed-through matrix

This formulation is particularly useful because it provides a compact representation of a system's dynamics. Additionally, it enables analytical solutions and facilitates straightforward analysis. For example, given an initial state $\mathbf{x}(0) = \mathbf{x}_0$, the state vector can be analytically determined by

$$\mathbf{x}(t) = e^{\mathbf{A}t}\mathbf{x}_0 + \int_0^t e^{\mathbf{A}(t-\tau)}\mathbf{B}\mathbf{u}(\tau)\, d\tau, \tag{2.4}$$

with

$$e^{\mathbf{A}t} = \sum_{k=0}^{\infty} \frac{(\mathbf{A}t)^k}{k!}. \tag{2.5}$$

Once the state vector $\mathbf{x}(t)$ is obtained, the desired system output can be easily computed using the Output and Feed-through matrices

$$\mathbf{y}(t) = \mathbf{C}\mathbf{x}(t) + \mathbf{D}\mathbf{u}(t).$$

While this formulation is typical for linear systems, the state-space representation can be generalized to nonlinear systems by replacing the coefficient matrices with nonlinear vector functions, as follows:

$$\dot{\mathbf{x}}(t) = \mathbf{f}(\mathbf{x}(t), \mathbf{u}(t)), \tag{2.6}$$
$$\mathbf{y}(t) = \mathbf{g}(\mathbf{x}(t), \mathbf{u}(t)), \tag{2.7}$$

where $\mathbf{f}(\cdot)$ and $\mathbf{g}(\cdot)$ are nonlinear functions describing the system dynamics.

Even for nonlinear systems, where an analytical solution is generally not possible, the State-Space formulation facilitates the implementation of known numerical schemes for solving the system.

Solving a system in Space-State formulation can be done using traditional ODE solvers. In particular, the `scipy.solve_ivp()` solver is used, utilizing the 'RK45' and 'RADAU' methods depending on the characteristics of the system [26].

2.1.3. Laplace Transform

The **Laplace Transform** converts a time-domain signal into the complex frequency domain, the transform is defined by:

$$\mathcal{L}\{h(t)\}(s) = \int_0^{\infty} h(t)e^{-st}\, dt. \tag{2.8}$$

The following notation will be used interchangeably

$$\mathcal{L}\{h(t)\} = \mathcal{H}(s) = \mathcal{H} \tag{2.9}$$

Some key properties include:

- **Linearity**:
$$af(t) + bh(t) \leftrightarrow a\mathcal{F}(s) + b\mathcal{H}(s)$$
- **Derivative**:
$$\frac{d^n}{dt^n}h(t) \leftrightarrow s^n\mathcal{H}(s) - \sum_{k=0}^{n-1} h^{(k)}(0)s^{n-k-1}$$

- **Convolution**:

$$(f * h)(t) \leftrightarrow \mathcal{F}(s) \cdot \mathcal{H}(s)$$

The discrete-time analogue of the Laplace Transform is the **Z-transform**, denoted as $\mathcal{Z}\{\cdot\}(z)$. This thesis assumes that all *necessary assumptions* are met, such that the differences between the Laplace and Z-transform are not of practical significance,

2.1.4. Fourier Transform

The **Fourier Transform** (FT) is an operator that once applied to a time signal, result in its decomposition into its frequency components, enabling analysis in the frequency domain, it is defined as :

$$\mathcal{F}\{f(t)\}(\omega) = \int_{-\infty}^{\infty} f(t)e^{-j\omega t}\,dt, \tag{2.10}$$

with its inverse defined by:

$$f(t) = \frac{1}{2\pi}\int_{-\infty}^{\infty} F(\omega)e^{j\omega t}\,d\omega. \tag{2.11}$$

Its shorthand or abbreviated notation is

$$\mathcal{F}\{f(t)\} = \mathcal{F}(\omega) = \mathcal{F} \tag{2.12}$$

A few key properties are:

- **Linearity**:

$$af(t) + bg(t) \leftrightarrow aF(\omega) + bG(\omega)$$

- **Derivative**:

$$\frac{d^n}{dt^n}f(t) \leftrightarrow (j\omega)^n F(\omega)$$

- **Convolution**:

$$(f * g)(t) \leftrightarrow F(\omega) \cdot G(\omega)$$

Under the *necessary conditions*, the Fourier Transform can be viewed as a special case of the Laplace Transform by performing the following substitution:

$$\mathcal{F}\{g(t)\} = \mathcal{L}\{g(t)\}\big|_{s=j\omega} \tag{2.13}$$

For discrete signals of length N, we define the Discrete Fourier Transform (DFT) and its inverse as:

$$X[k] = \sum_{n=0}^{N-1} x[n]e^{-j2\pi kn/N}, \quad x[n] = \frac{1}{N}\sum_{k=0}^{N-1} X[k]e^{j2\pi kn/N}.$$

Although the term Fast Fourier Transform (FFT) refers to a specific algorithm for computing the Discrete Fourier Transform [27], in this work, FFT, FT, and DFT will be used interchangeably, referring to the process of decomposing a signal into its frequency components.

2.1.5. Frequency Response Function

The **Frequency Response Function** (FRF) describes how a LTI system responds to a set of sinusoidal excitations

Consider the State-Space representation:

$$\dot{\mathbf{x}}(t) = \mathbf{A}\mathbf{x}(t) + \mathbf{B}\mathbf{u}(t), \tag{2.14}$$

$$\mathbf{y}(t) = \mathbf{C}\mathbf{x}(t) + \mathbf{D}\mathbf{u}(t) \tag{2.15}$$

The system is being excited by an input of the form

$$\mathbf{u}(t) = \Re\{\hat{\mathbf{u}}e^{j\Omega t}\} \tag{2.16}$$

Since LTI systems commute with the exponential function, a complex exponential input leads to a steady-state output of the form:

$$\mathbf{y}(t) = \Re\{G(j\Omega)\hat{\mathbf{u}} \cdot e^{j\Omega t}\}$$

Here, $G(j\Omega)$ is the frequency response (Transfer function at $s = j\Omega$). This implies that, for linear systems, the FRF defines how the gain (amplitude) and phase change across input frequencies. Thus, it can also be expressed as:

$$\mathbf{y}(t) = |G(j\Omega)| \cdot |\hat{\mathbf{u}}| \cdot \cos(\Omega t + \angle\hat{\mathbf{u}} + \angle(G(j\Omega))) \tag{2.17}$$

This shows that the output has:

- The same frequency Ω as the input,
- Scaled amplitude $|G(j\Omega)| \cdot |\hat{\mathbf{u}}|$,
- Phase shift $\angle(G(j\Omega))$.

Then, the frequency response function of the LTI system is:

$$G(j\Omega) = H(\Omega) = \mathbf{C}(j\Omega I - \mathbf{A})^{-1}\mathbf{B} + \mathbf{D} \tag{2.18}$$

Numerically, for $\Omega_k \in \Omega$,

$$H(j\omega_k) = \mathbf{C}(j\omega_k\mathbf{I} - \mathbf{A})^{-1}\mathbf{B} + \mathbf{D}.$$

FRF from Numerical model

For nonlinear systems, the FRF can be numerically estimated under the following procedure:

1. **Input Signal**
   Apply a sinusoidal input corresponding to a set of discrete frequencies.
2. **Time-Domain Simulation**
   Numerically compute the system's response to all the different input frequencies.
3. **FFT**
   Extract the steady-state responses and apply the FT to the responses.
4. **Estimate FRF**:
   Estimate the FRF by computing the ratio between the response and and input signal, for all excitation frequencies
   $$\hat{H}(\omega) = \frac{\hat{\mathbf{Y}}(j\omega)}{\hat{\mathbf{U}}(j\omega)}.$$

2.2. Power-Hydraulics

Hydraulic circuits can incorporate a wide variety of components, resulting in numerous possible configurations. Since the main objective of this work is to investigate the coupling of a hydraulic-powered shaker and a flexible structure, the simplest circuit that can accurately model the dynamics of the coupled system will be adopted.

To that end, the five-element circuit shown in Figure 2.1 is considered:

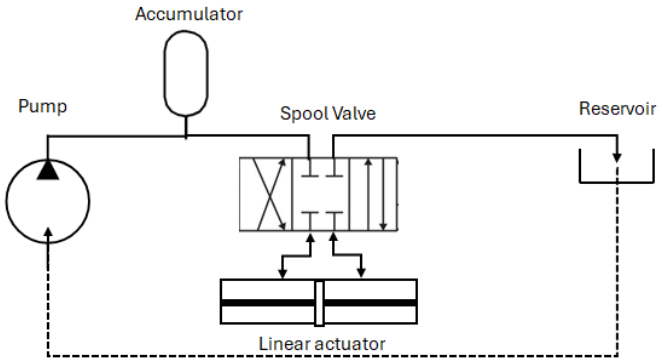

Figure 2.1: Diagram of hydraulic circuit

The following subsections present a brief description and modeling assumptions of each component depicted in Figure 2.1

2.2.1. Pump

A pump is an element that generates a pressure gradient, which drives a flow through the hydraulic circuit.

Pumps are generally classified according to the characteristics of the flow that they produce. Two primary types are commonly recognized in the literature [28].

- **Hydrodynamic Non-Positive Displacement**
  This type of pump produces a flow rate that is highly dependent on the back pressure (P_b). Any resistance encountered downstream will directly affects the pump's performance, therefore, this type of pump is best suited for high-flow, low-pressure applications.
- **Hydrodynamic Positive Displacement**
  Positive displacement pumps displace a fixed volume of fluid per cycle, thereby generating a pressure gradient. As a result of the fixed-volume mechanism, their flow rate is largely insensitive to variations in load pressure, making them suitable for applications that require a constant flow rate.

Given the requirements of the hydraulic circuit for driving a linear actuator, a hydrostatic positive displacement pump is required. Accordingly, the pump is assumed to deliver a flow that is independent of the back pressure in the system, effectively decoupling it from the dynamics of the rest of the circuit. Therefore, the pump will be modeled as:

$$\frac{dQ_{pump}}{dP_b} = 0 \quad \text{for} \quad P_b < P_s \tag{2.19}$$

An in depth discussion of the various types of positive displacement pumps, including their internal mechanisms, non-ideal dynamic behavior, robustness, and other characteristics, can be found in [29].

2.2.2. Accumulator

Equation (2.19) assumes an idealized, constant flow pump behavior. While this does not capture the full complexity of real pump dynamics, the assumption can serve as a reasonable approximation when the pump operates together with a properly designed **Accumulator** that mitigates the effects pressure transients.

An accumulator is a hydraulic component designed to store energy in the form of pressurized fluid, which is released as the system demands it in order to maintain a constant flow at a constant pressure.

Therefore, in a hydraulic system, the stored energy in an accumulator helps smooth out pressure and flow transients, which are caused by the nonlinear response of the downstream system. As a result, under the operating conditions of a properly designed pump-accumulator system, the supplied pressure (P_s) behaves quasi-statically as expressed in equation (2.19).

A simple way to model the dynamics introduced by an accumulator can be seen in equation (2.20). The equation, is derived from the conservation of mass, by considering the net flow and the equivalent compliance of the accumulator (compressibility of fluid and/or gas depending on the type of accumulator)[30]

$$\frac{dP}{dt} = \frac{1}{C_{eq}} \left(Q_{in} - Q_{out} - C_{leak}(P - P_{atm})\right) \tag{2.20}$$

Nevertheless, expression (2.19) will be employed in this thesis.

2.2.3. Valves

Hydraulic valves are generally divided into two main types based on how they regulate flow:

1. **Directional Valves**
   These valves have a finite number of states, permitting full, partial, or no flow. While essential to any hydraulic system, directional valves are not explicitly modeled in this work, as their states remain fixed during operation and do not affect the system's dynamics.
2. **Control Valves**
   Control valves can continuously adjust their internal state during operation. They are further categorized based on what they regulate:
   - Flow Control
   - Pressure Control

The detailed modeling of the flow within a valve is intrinsically complex and typically necessitates the use of Computational Fluid Dynamics (CFD) analysis [31]. In this work, an Eulerian framework is adopted, wherein the flow is analyzed at the upstream and downstream boundaries of the valve. To reduce computational complexity, the internal flow domain of the valve is excluded from the model. This approximation holds as long as the operating conditions stay within the valve's rated range, which is determined by the manufacturer through prior analysis. Within these limits, the dynamics are predictable and well described.

Starting from the Navier-Stokes equations [32], the fluid velocity can be described by the following expression:

$$\rho\left(\frac{\partial \mathbf{u}}{\partial t} + \mathbf{u}\cdot\nabla\mathbf{u} - \mathbf{f}\right) = -\nabla p + \mu\nabla^2\mathbf{u} \tag{2.21}$$

Neglecting viscosity ($\mu \approx 0$), body forces ($\mathbf{f} \approx 0$), and assuming locally steady conditions, the equation can be simplified to

$$\rho(\mathbf{u}\cdot\nabla)\mathbf{u} = -\nabla p \tag{2.22}$$

Assuming unidirectional flow along $\hat{x}$, and integrating along a streamline, the 1D Bernoulli equation is obtained

$$p + \frac{1}{2}\rho u_x^2 = c \tag{2.23}$$

Then, if the velocity profiles across in the in-ports and out-ports (boundaries of control volume) are uniform, the flow can be computed as

$$Q = \int u_x dA \tag{2.24}$$

$$Q = u_x \int dA \tag{2.25}$$

Valve-Port Geometry

The predominant mechanism by which control valves can regulate flow dynamically is by modulating the port area by gradually obstructing/covering it. As a result, the area differential (dA) can be conveniently expressed in terms of a single variable (x_{sp}).

Rearranging equation (2.22) for u_x and replacing it in the flow equation yields

$$Q = u_x \int dA \tag{2.26}$$

$$Q = \sqrt{\frac{2c\Delta P}{\rho}} \int \left(\left(\frac{\partial A}{\partial x_{sp}} \right) \cdot \left(\frac{\partial x_{sp}}{dt} \right) \right) dt \tag{2.27}$$

With ΔP the pressure drop across the valve.

Equation (2.26) demonstrates that the flow through the valve is linearly proportional ($\propto$) to the *Area-Rate*.

The Area-Rate function characterizes the variation of the port area over time. This function is influenced by two factors: the geometric factor and the dynamic factor, as shown in equation (2.28).

$$Q \propto \text{Area Rate} = \underbrace{\left(\frac{\partial A}{\partial x_{sp}} \right)}_{\text{Valve Geometry}} \cdot \underbrace{\left(\frac{\partial x_{sp}}{\partial t} \right)}_{\text{Spool Dynamics}} \tag{2.28}$$

The effects of the port geometry can be analyzed by comparing three commonly used geometries: [33]

$$\text{Proportional:} \quad A(x_{sp}) = cx \tag{2.29}$$

$$\text{Quick Opening:} \quad A(x_{sp}) = c\sqrt{x_{sp}} \tag{2.30}$$

$$\text{Equal Percentage:} \quad A(x_{sp}) = \frac{\exp(C_{equal} x_{sp}) - 1}{\exp(C_{equal}) - 1} \tag{2.31}$$

A graphic comparison of the effect of the different geometries can be seen in Figure 3.5

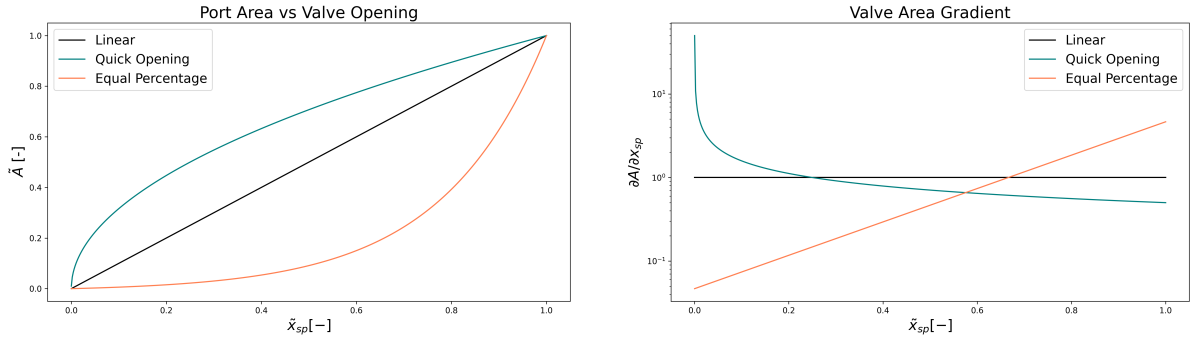

(a) Port area geometry

(b) Port area gradient

Figure 2.2: Geometric characteristics of valves.

For active hydraulic control applications, Quick Opening valves are less suitable due to their highly sensitive flow characteristics. Minor deviations in pressure relative to the supplied pressure (P_s), can

produce large changes in flow rate, leading to poor controllability. Additionally, their response is often too abrupt, potentially creating flow surges and transient pressure waves that are difficult to control and could potentially lead to instability and increased mechanical stress on system components.

In contrast, Equal Percentage valves provide improved control resolution across a wide range of flow conditions, particularly at higher flow rates. Their nonlinear flow characteristic allows finer control near the lower end of the stroke and more aggressive flow increase near full valve opening, making them suitable for systems with variable flow demands and high operating pressures. This makes them appropriate for applications requiring consistent control performance across a broad operating range. However, their gradual response prioritizes stability over fast response, making them more appropriate for systems with well-defined and relatively slow dynamics.

Both valve types introduce nonlinear relationships between Q and x_{sp} ,thereby increasing the complexity of the control algorithm. To analyze their dynamic behavior, it is useful to evaluate the response to a step and harmonic inputs.

$$\begin{aligned} \text{Step Response:} \quad & U(t) = H(t) \\ \text{Harmonic Response:} \quad & U(t) = \sin(2\pi f t) \end{aligned}$$

Defining that x_{sp} takes a time τ to respond to the control signal and that

$$\tilde{Q} = \frac{Q}{Q(x_{sp} = 1)}$$
$$\tilde{t} = \frac{t}{\tau}$$

The following dynamic responses are obtained

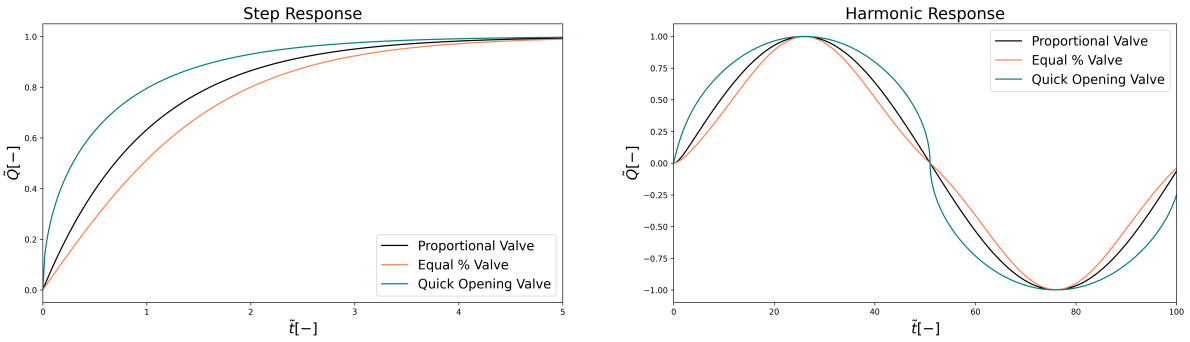

(a) Response to step signal

(b) Response to harmonic signal

Figure 2.3: Dynamic response of different port geometries

As shown in Figure 2.4a, Quick Opening valves reach near-maximum flow early in the control range, closely following the control input, whereas the Equal Percentage valve produces a more gradual flow increase. It is important to note that this comparison assumes identical actuator response times; the observed differences are solely due to the flow characteristics determined by valve geometry.

For hydraulic cylinder applications, a sinusoidal input provides a meaningful indicator of operational performance. As shown in Figure 2.4b, although all valves follow the same command opening, Quick-Opening valves produces an early overshoot in flow due to its nonlinear port geometry.

This results in a flow response that deviates from the intended target, even though the valve opening follows the commanded input. The effect becomes more pronounced when

- The command valve signal deviates from a pure sinusoidal shape

- Command signal is result of closed-loop control, where the control input is typically influenced by downstream flow and pressure feedback.

In contrast, Equal-Percentage valves exhibits a more gradual flow characteristic, which, despite introducing a slight lag, provides a response that more closely aligns with the desired flow profile.

Given that the valve response time is fixed for each valve and generally independent of the port geometry, its dynamic performance can be characterized by the dimensionless ratio τf, where τ is the valve's intrinsic response time and f is the frequency of the control signal. This ratio provides a measure of the valve's ability to respond relative to the input signal's period, with smaller values indicating better tracking performance.

A small value of this ratio indicates that the valve can respond rapidly to changes in the control signal, whereas a larger value implies that the valve may lag behind, reducing controllability. This ratio is particularly important for Quick-Opening valves, whose fast but highly sensitive response can produce flow overshoots and transient instabilities under rapidly varying inputs. In contrast, Equal Percentage valves, with a more gradual response, exhibit a larger temporal lag for higher-frequency inputs, but their smoother behavior provides improved control stability across a wide range of operating conditions.

Consider the following parameters range, corresponding to typical values of commercially available hydraulic valves [34].

$$\tau \in (0.1, 0.001)s$$
$$f \in (1, 100)Hz$$

These ranges provide a basis for evaluating the τf ratio, and its performance.

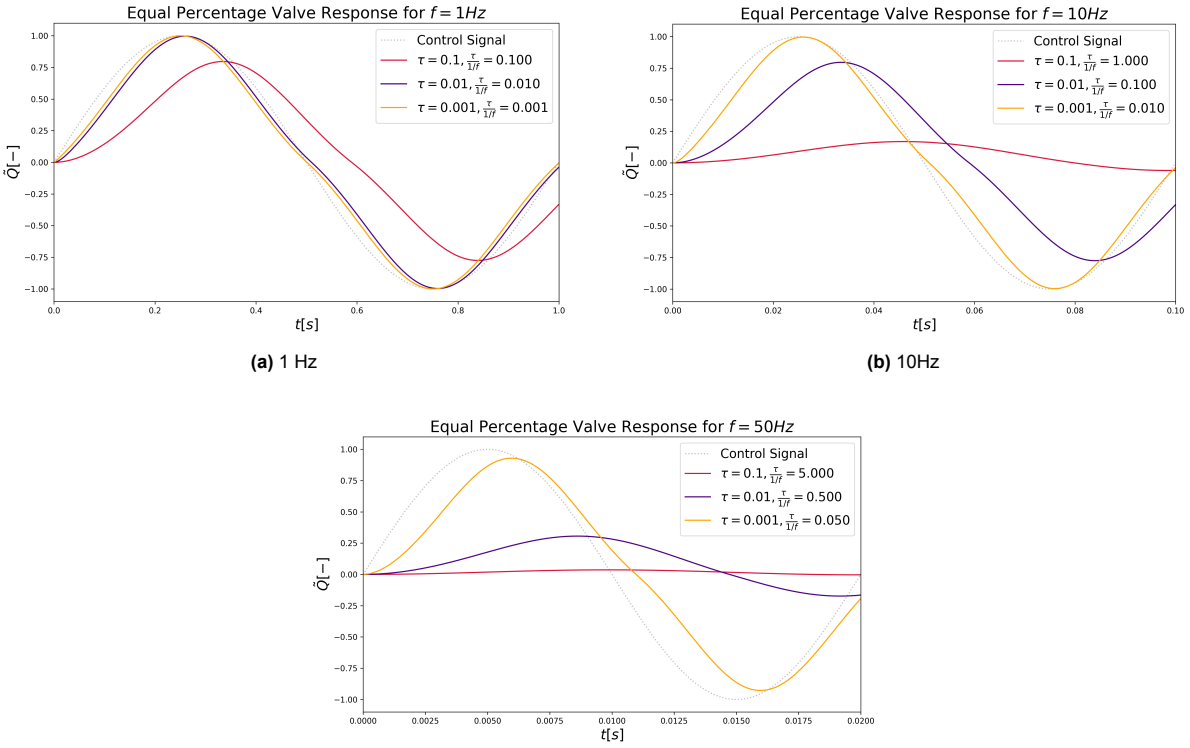

(a) 1 Hz

(b) 10Hz

(c) 50 Hz

Figure 2.4: Equal Opening flow response to harmonic valve command at different frequencies

The responsiveness of Quick-Opening valves can be beneficial in high-performance systems, provided that overshoot is adequately controlled. This can be achieved through the use of servo-valves and flow-pressure-controlled valves, and/or advanced control schemes.

As previously discussed, Quick-Opening are highly nonlinear as a result that the port opening is a nonlinear function of the valve position, as shown in Figure 2.5.

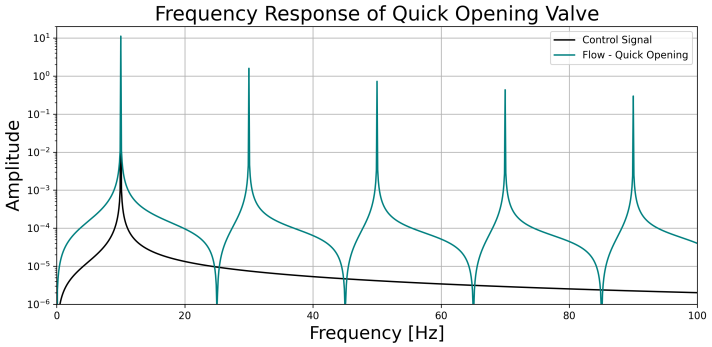

Figure 2.5: Flow Frequency Response of Quick Opening valve to 10Hz control signal

This nonlinearity is not inherently limiting, and the fast response can be advantageous for controlling system transients. However, this depends on the specific of the control system and more importantly on the accuracy of the valve model dynamics, which is challenging to model if it is affected by additional nonlinear effects such as dead zone, backlash, and hysteresis.

Consequently, due to their simplified design, lower cost, and ease of maintenance, Proportional valves are often preferred in industrial control applications, over Quick-Opening and Equal-Percentage.

In the subsequent analysis, all valves will be modeled as Proportional valve. Substituting the Proportional valve geometry into (2.26) yields the following expression:

$$Q(t) = |x_{sp}|(t)K_q\sqrt{1-\frac{P(t)}{P_s}} = x_{sp}(t)K_q\sqrt{1-\eta(t)} \tag{2.32}$$

It is important to reiterate, that expression (2.32) ignores inertial effects associated with transient flows and viscous forces.

Valve Stages

In addition to port geometry, valves can also be classified based on the number of flow paths (or stages) that they have, as well as the mechanism used to modulate the flow area [33]. In this work, a 4-way spool valve, illustrated in Figure 2.6, is considered.

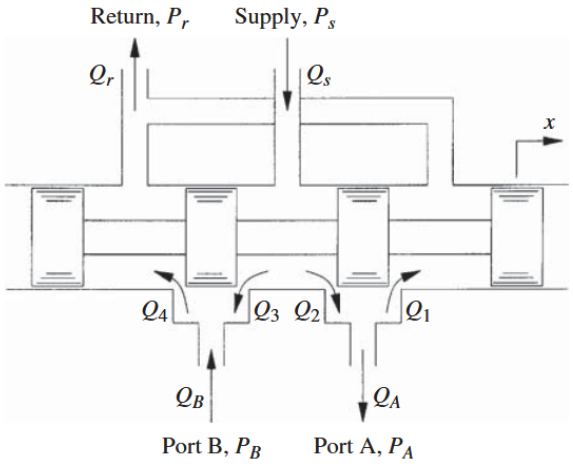

Figure 2.6: Diagram of 4-way spool valve [28]

As shown in Figure 2.6, flow can be directed to either Port A or Port B, enabling fluid to move from the pump to the actuator chambers or return from the chambers back towards the pump. In the case of a symmetric linear actuator, where both chambers have equal volumes and piston areas, the modeling is simplified by considering only the net flow and pressure differential, as chamber-specific effects cancel out. This simplification is valid provided that pressure loss due to cross-chamber leakage is accounted for [35].

Thus, the resulting flow can be represented in a compact form as:

$$Q(t) = |Q| \cdot \text{Polarity} \cdot \text{Directionality} \tag{2.33}$$

The flow polarity defines the flow direction by specifying which actuator chamber receives fluid based on the spool displacement, assuming a critically centered spool (all flow paths are fully blocked at the neutral position) .

$$\text{Polarity} = sgn(x_{sp}) \tag{2.34}$$

The directionality coefficient defines the flow path, either towards the pump or actuator. This behavior can be expressed as:

$$\text{Directionality} = \begin{cases} 1, & \text{if } P < P_s \\ -Q_{\text{backflow}}, & \text{if } P > P_s \end{cases} \tag{2.35}$$

In accordance with equation (2.35), a negative pressure drop across the valve can reverse the flow direction. However, complete flow reversal is generally unrealistic for two main reasons:

- Although spool valves are not inherently unidirectional, practical hydraulic circuits often include components, such as check valves, intended to prevent flow reversal.
- Due to the high bulk modulus of hydraulic oil, the fluid upstream of the valve behaves as a highly stiff column, resisting compression and thereby limiting backflow during transient pressure reversal.

Nevertheless, this work aims to operate the hydraulic system at the lowest possible supply pressure, which increases the likelihood of temporary flow reversal, highlighting the need for accurate modeling of this phenomenon.

To address this, two models are introduced to represent the flow behavior under potential transient backflow. These models are designed to provide a continuous transition between partial backflow and no backflow, ensuring that the simulation remains physically realistic while capturing the effects of flow reversal."

$$Q_{\text{tanh}} = \frac{1 + \tanh\left(-\beta_Q \left(\eta - 1\right)\right)}{2}$$

$$Q_{\text{spline}} = \left(3 - 2\left(\frac{(1-\eta) + d_Q}{2d_Q}\right)\right) \cdot \left(\frac{(1-\eta) + d_Q}{2d_Q}\right)^2$$

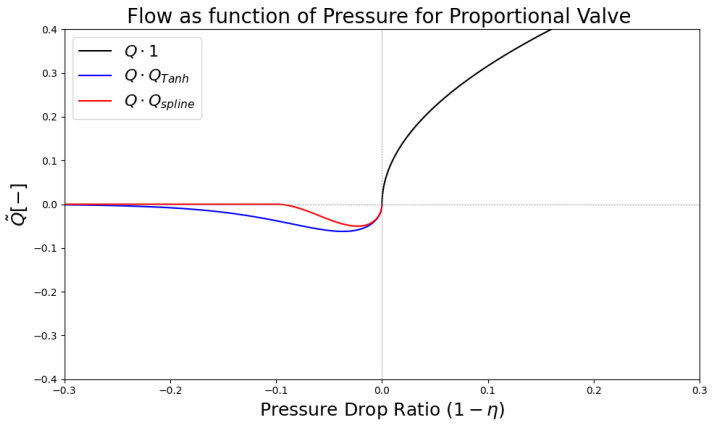

Figure 2.7: Flow reversal models

Pressure Control Valves

Up to this point, only flow control valves have been considered. However, pressure regulation can also be achieved by incorporating a compliant mechanism such as a spring within the valve assembly. This design enables the spool to respond not only to the control signal but also to pressure forces arising from the flow through the valve, thereby enabling a form of passive pressure control.

Alternatively, pressure regulation can be accomplished using servo valves, which integrate dedicated feedback and control systems. Servo valves offer higher precision, faster response, and minimal hysteresis due to their tight manufacturing tolerances and built-in position and pressure sensors. These features make them well suited for applications requiring high dynamic performance and repeatability, and well defined plant dynamics[36].

However, they are more complex and costly, require regular maintenance and are generally less suitable for high-load or high-power-density systems, and therefore will not be part of the system being studied. Aditionally, they are prone to:

- **Increased Valve Dead-Zone:**
  The spool must overcome the spring's pretension before any motion occurs, resulting in a larger dead-zone and reduced control sensitivity around the neutral position.
- **Nonlinear Control Response:**
  The relationship between the control signal and spool displacement becomes nonlinear, requiring advanced control strategies for accurate valve operation.
- **Introduction of Additional Dynamics:**
  Adding spool compliance introduces a new degree of freedom, significantly increasing model complexity. The spool now responds to pressure forces, and inertial effects, viscous damping, and other internal fluid-structure interactions must be considered. These interactions influence system performance and are difficult to capture analytically, often requiring empirical characterization or numerical simulation [37].

In contrast, flow control valves are simpler but precise, typically operating in open-loop or limited-feedback configurations. Their relative robustness, lower cost, and reduced maintenance requirements make them a practical choice for industrial applications [38], and for the system being studied.

2.2.4. Linear Actuator

Lets consider the case of a two chamber linear actuator, such as the one shown in Figure 2.8

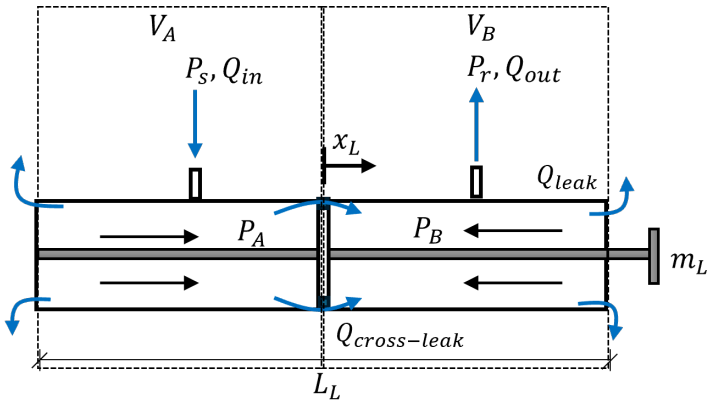

Figure 2.8: Diagram of linear actuator

The net force exerted by the hydraulic system is determined by considering a rigid piston assembly and applying the Second Newton's law to it

$$\sum F = \frac{d(m_L \dot{x}_L)}{dt}$$

$$\underbrace{F_P}_{\text{Hydraulic Pressure}} + \underbrace{F_k}_{\text{Actuator Stiffness}} + \underbrace{F_c}_{\text{Actuator Damping}} + \underbrace{F_{fr}}_{\text{Internal Friction}} = m_L \ddot{x}_L$$

$$(P_A A_A - P_B A_B) - k_L x_L - c_L \dot{x}_L - f_{fr} = m_L \ddot{x}_L \tag{2.36}$$

The friction forces within a hydraulic actuator can be described using Coulomb, viscous, or mixed wet–dry friction models. However, accurately modeling these effects is challenging, as the dominant friction regime depends on several factors, such as stroke velocity, fluid viscosity, seal type, maintenance condition,surface roughness, etc [39].

As a result, when modeling a generic hydraulic system it is common to approximate the friction effect with a linear viscous damping term. This simplification effectively captures the system's overall energy dissipation characteristics without introducing excessive model complexity [40].

Additionally, particularly in control oriented problems, this approach can be extended to include additional nonlinearities such as backlash and dead-zone effects, which together provide a more representative model of actuator response under practical operating conditions, without explicitly modeling the full tribological response of the actuator.

Therefore, the expression (2.36) can be simplified to

$$m_L \ddot{x}_L + b\dot{x}_L + kx_L = A(P_A - P_B) \tag{2.37}$$

Pressure Balance

The pressure in each chamber is determined by applying the conservation of mass principle to the control volumes shown in figure 2.8 and described by

$$V_A(t) = V_{A_0} + A_A \cdot x_L(t)$$
$$V_B(t) = V_{B_0} - A_B \cdot x_L(t)$$

With $V_{A_0} = V_{B_0} = 0.5V_L$

The hydraulic oil within the actuator is modeled as a compressible fluid with effective bulk modulus β_e.

Several factors influence the compressibility of hydraulic oil, including:

- Gas content (trapped or dissolved)
- Temperature
- Pressure

Trapped or dissolved gases, such as air, can significantly affect the compressibility of hydraulic oil [41, 42]. Additionally, thermal effects, which interact with these trapped gases, further influence the oil's compressibility [43].

However, for the purposes of this study, both the effects of entrained air and thermal performance are neglected. Instead, the compressibility due to pressure effects will be modeled as follows::

$$\beta_e = \rho \frac{dP}{d\rho} \longrightarrow \frac{d\rho}{dt} \approx \frac{\rho}{\beta_e} \dot{P} \tag{2.38}$$

Then, the net mass flow rate can be expressed in terms of volumetric flow

$$\dot{m}_{net} = \rho Q_{net}$$

Applying Reynold's Transport Theorem ([32])to the control volumes, results in:

$$\frac{d}{dt} \int_{V_A(t)} \rho \, dV = \rho Q_{net}$$

Using Leibniz integral rule

$$\frac{d}{dt} \left[\rho(t) V_A(t) \right] = \rho Q_{net}$$
$$V_1 \frac{d\rho}{dt} + \rho \frac{dV_1}{dt} = \rho Q_{net}$$
$$\frac{V_A}{\beta_e} \dot{P}_A + \dot{V}_A = Q_{net}$$

$$\left(\frac{V_{A0} + A_A x_L}{\beta_e} \right) \dot{P}_A + A_A \dot{x}_L = Q_{net} \tag{2.39}$$

The net flow can be easily determined by examining Figure 2.8, is evident that the net flow is:

$$Q_{net} = \sum_{i}^{n} Q_i$$
$$Q_{net} = Q_A - Q_B - Q_{leak}$$

In each chamber, two sources of leakage are considered: external leakage and cross-chamber leakage. External leakage occurs between the pressure difference between the chamber and atmospheric pressure, while cross-chamber leakage occurs between the difference in pressure between the two chambers [28].

If the chambers, seals, and leak coefficients are symmetrical, and

$$x_L \ll L_L \longrightarrow V_A \approx V_{A_0}$$

The net flow in the actuator can be described by:

$$Q_{net} = [c_1(P_s - P_A) - c_2(P_A - P_{atm}) - c_3(P_A - P_B)] - [c_4(P_B - P_r) - c_5(P_B - P_{atm}) + c_6(P_A - P_B)] \tag{2.40}$$

The expression can be simplified by grouping the actuator-dependent coefficients. Thus, combining expressions (2.39) and (2.40) results in:

$$Q = c_1 \dot{P} + c_2 P + A_L \dot{x}_L \tag{2.41}$$

This expression provides a concise way of expressing the net flow in terms of pressure, pressure rate and piston velocity, which together represent the conservation of mass for a compressible fluid in a moving and leaking control volume.

2.2.5. Tank reservoir

The tank reservoir is an element that receives the flow after it has passed through the system. It is typically connected to the pump, providing a constant volume of hydraulic fluid. In this work, unless otherwise stated, it is assumed that the reservoir is vented, meaning that its pressure is maintained at atmospheric conditions:

$$P_r = P_{atm}$$

2.2.6. Hydraulic Lines

In hydraulic systems, hydraulic lines serve as flow paths connecting various components. Energy losses also occur at transition elements such as joints and connections, characterized by loss coefficients under steady-state conditions. Additionally, viscous forces acting along fluid boundaries cause energy losses, commonly expressed per unit length of the line. These effects become more complex and pronounced in flexible hose systems, where dynamic deformation and hose geometry further influence system behavior.

Extensive research has examined the influence of hose characteristics such as length, stiffness, and configuration on system dynamics and efficiency [44, 45]. However, in this thesis, the hydraulic lines are not explicitly modeled. Given the assumptions regarding the accumulator design and valve configuration, the hydraulic line effects are assumed to have a negligible impact on the system dynamics

2.2.7. Solenoid

As previously described in equation (2.32) and illustrated in Figure 2.6, a flow control spool valve can be operated using a single control variable, x_{sp}, which typically corresponds to the axial displacement of a spool over the valve in-port [33]. This axial displacement, which directly modulates the flow area, is commonly achieved via a solenoid-actuated mechanism, due to its simplicity, compactness, cost-effectiveness, and fast response characteristics, making it well-suited for control systems.

Consequently, the axial displacement of the spool, serves as the primary control input for the actuator, linking the valve dynamics directly to the flow and subsequently pressure and force. Thereby providing a direct mapping from control signals to actuator motion.

To better understand the dynamics of the spool, consider a current-operated spool valve subject to the control signal ($U(t)$). Because the solenoid is current-operated but the control input is commonly expressed in terms of a voltage signal, a Voltage-Current transformer subsystem is used to convert the input voltage into a coil current that drives the solenoid. The dynamics of this subsystem can be captured using a first-order transfer function [46].

$$\mathcal{H}_{Ui}(s) = \frac{\mathcal{L}\{i\}}{\mathcal{L}\{U\}} = \frac{K_{IU}}{\tau_{iU}s + 1} \tag{2.42}$$

For electrical systems, the dynamics of components such as the Voltage-Current transformer are often described in the complex (Laplace) domain. However, since the hydraulic system dynamics are defined in the time domain, it is convenient to adopt a unified domain for modeling both subsystems. Accordingly, the electrical subsystem is also represented in the time domain by applying the Inverse Laplace Transform to expression (2.42).

$$\frac{di(t)}{dt} = \frac{1}{\tau_{iU}}\left(-i(t) + K_{iU}U(t)\right)$$

The dynamics of the spool can be understood by analyzing the forces acting on it. Accordingly, the following equation represents the balance of forces on the solenoid-actuated spool

$$m\ddot{x}_{sp} + b\dot{x}_{sp} + kx_{sp} = F_{solenoid}$$

The force produced by the solenoid can be approximated using the following expression [46]:

$$F_{solenoid} = -\nabla E_{mag} \tag{2.43}$$

$$F_{solenoid} = -\nabla \left(\frac{1}{2} L i^2 \right) \tag{2.44}$$

$$F_{solenoid} = -\frac{1}{2} i^2 \frac{dL}{dx_{sp}} \tag{2.45}$$

For small spool displacements, the inductance can be approximated by [47]:

$$L(x_{sp}) \approx \frac{c}{x_{sp}} \tag{2.46}$$

Therefore, the dynamics of the spool are described by

$$m\ddot{x}_{sp} + b\dot{x}_{sp} + kx_{sp} = \frac{1}{2} i^2 \frac{cte}{x_{sp}^2} \tag{2.47}$$

Although this represents a nonlinear ODE, flow control spool valves are designed such that, within the manufacturer's specified range, the spool dynamics can be accurately modeled by a first-order transfer function [28].

$$\mathcal{H}_{isp}(s) = \frac{\mathcal{L}\{i\}}{\mathcal{L}\{x_{sp}\}} \frac{K_{isp}}{\tau_{isp} s + 1} \tag{2.48}$$

Expression with a time domain counterpart of

$$\frac{dx_{sp}(t)}{dt} = \frac{1}{\tau_{ix_{sp}}} \left(-x_{sp}(t) + K_{ix_{sp}} i(t) \right) \tag{2.49}$$

2.3. Structure

The dynamics of the plant (i.e., the system or structure being excited by the power hydraulic system) are first described using a single degree of freedom (SDOF) model and subsequently extended to a multi degree of freedom (MDOF) system corresponding to an Euler–Bernoulli (EB) beam.

The dynamics of a continuous Euler–Bernoulli beam can be described by the following partial differential equation (PDE):

$$EI \frac{\partial^4 u}{\partial x^4} + \rho A \frac{\partial^2 u}{\partial t^2} = q(x,t), \tag{2.50}$$

where

- $u(x,t)$ is the transverse displacement of the beam
- $q(x,t)$ represents the distributed external load per unit length.

2.3.1. Finite Element Discretization

As is common in structural dynamics, the PDE can be discretized using Galerkin's method. By considering cubic Hermite interpolating functions and two-node, four-degrees-of-freedom elements, the PDE is transformed into a system of ODEs [48]:

$$\mathbf{M}\ddot{\mathbf{x}}(t) + \mathbf{K}\mathbf{x}(t) = \mathbf{F}(t) \tag{2.51}$$

Here, $\mathbf{M}$,and $\mathbf{K}$ are the mass and stiffness matrices of the discretized system and $\mathbf{x}(t)$ is the vector of nodal displacements,

The system matrices $\mathbf{M}$ and $\mathbf{K}$ are assembled from the corresponding local (element) matrices. For a two-node, four-degrees-of-freedom beam element of length L_e, these local matrices are given by [48]:

$$\mathbf{K}_e = \frac{EI}{L_e^3}\begin{bmatrix} 12 & 6L_e & -12 & 6L_e \\ 6L_e & 4L_e^2 & -6L_e & 2L_e^2 \\ -12 & -6L_e & 12 & -6L_e \\ 6L_e & 2L_e^2 & -6L_e & 4L_e^2 \end{bmatrix},$$

$$\mathbf{M}_e = \frac{\rho A L_e}{420}\begin{bmatrix} 156 & 22L_e & 54 & -13L_e \\ 22L_e & 4L_e^2 & 13L_e & -3L_e^2 \\ 54 & 13L_e & 156 & -22L_e \\ -13L_e & -3L_e^2 & -22L_e & 4L_e^2 \end{bmatrix}.$$

The global matrices $\mathbf{M}$ and $\mathbf{K}$ for the entire structure are obtained by assembling the local element matrices according to the connectivity of the nodes.

Damping ($\mathbf{C}$) can be included using standard proportional or modal damping assumptions. In this case, Rayleigh damping will be used.

Consider the homogeneous form of equation (2.50) and assume a solution of the form

$$\mathbf{x} = \mathbf{\Psi} e^{j\omega t}.$$

Substituting this into the undamped equation of motion yields

$$-\omega^2 \mathbf{M}\mathbf{\Psi} e^{j\omega t} + \mathbf{K}\mathbf{\Psi} e^{j\omega t} = 0, \tag{2.52}$$

$$\left(\mathbf{K} - \omega^2 \mathbf{M}\right)\mathbf{\Psi} = 0. \tag{2.53}$$

Solving this eigenvalue problem allows us to determine the mode shapes ($\mathbf{\Psi}$) and natural frequencies (ω_n) of the structure.

Then, Rayleigh damping is defined by [48]:

$$\mathbf{C} = \alpha \mathbf{M} + \beta \mathbf{K},$$

where α and β are coefficients determined by solving the system

$$\xi_i = \frac{1}{2}\left(\frac{\alpha}{\omega_i} + \beta\,\omega_i\right),$$

$$\xi_k = \frac{1}{2}\left(\frac{\alpha}{\omega_k} + \beta\,\omega_k\right),$$

which imposes prescribed modal damping ratios ξ_i and ξ_k corresponding to two specific modes with natural frequencies ω_i and ω_k.

2.3.2. Soil Damping

In addition to internal damping, a non-conservative force corresponding to the skin friction between the structure and the surrounding soil is considered. This friction is modeled as a velocity-dependent distributed force acting along the embedded length of the structure.

In the discretized model, the friction force per node, F_c, is derived from the continuous distribution of friction along the embedded portion of the structure, which primarily affects its translational degrees of freedom. Assuming a constant unit skin friction τ_c acting on the structural perimeter P_{struct}, the differential frictional force over an infinitesimal depth element dz is expressed as:

$$dF_c = \tau_c\, P_{\text{struct}}\, dz, \tag{2.54}$$

where P_{struct} denotes the perimeter of the structural cross-section.

Integrating along the embedded length L_{emb}, the total friction force becomes:

$$F_c = \int_0^{L_{\text{emb}}} \tau_c \, P_{\text{struct}} \, dz = \tau_c \, A_{\text{emb}}, \tag{2.55}$$

where A_{emb} is the total contact area between the structure and the soil.

The embedded length of the pile in the soil can be more conveniently expressed as the ratio between the current embedded length and the total length, using the coefficient ϱ:

$$\varrho = \frac{L_{\text{emb}}}{L} \tag{2.56}$$

To account for the velocity dependence of friction and to ensure numerical stability, the friction force applied at each node is modeled as:

$$\tau_c = q_c \, \tanh\left(\frac{\dot{x}_u}{v_s}\right), \tag{2.57}$$

where $\dot{x}_u$ is the nodal velocity and v_s is a scaling velocity parameter that controls the smoothness of the transition between static and fully mobilized friction.

The unit frictional resistance (q_c) along an embedded element is not constant, it varies with depth and time due to changes in stress distribution in the soil and soil-structure interaction mechanisms. Consequently, the total friction force can be expressed as:

$$\mathbf{F}_{\text{fric}} = \int_0^L \tau(z, \Lambda) \, \tanh\left(\frac{\dot{z}}{v_s}\right) \, P_{\text{struct}} \, dz \tag{2.58}$$

Here, z represents the depth, Λ denotes the loading path or penetration history. The dependence of q_c on depth reflects variations in soil properties and stress conditions, while the parameter Λ captures path-dependent (memory) effects such as cyclic degradation or changes induced by installation.

Time-related effects are primarily associated with the dissipation of excess pore water pressure and, to a lesser extent, soil aging and recovery [49]. In addition, repeated load cycles may lead to a phenomenon often referred to as *friction fatigue* , which reduces the mobilized frictional resistance when driving [50].

Therefore, due to the nonlinear, non-conservative, and history-dependent nature of frictional forces, in some cases it is convenient to represent their overall effect using an equivalent viscous damping ratio.

Consider the work during a cycle as

$$E_d = \oint F \, dx,$$

The elastic strain energy in the system is defined by

$$E_{elastic} = \frac{1}{2} k u^2$$

Then, the equivalent viscous damping coefficient is:

$$c_{\text{eq}}^X = \frac{E_d}{2\pi\omega X^2},$$

expressed in terms of damping ratio associated to cycle frequency

$$\xi^X = \frac{1}{4\pi} \frac{E_d}{E_{elastic}}$$

Although the actual damping mechanism is nonlinear, this equivalent representation provides a normalized and comparable measure of energy dissipation, which is particularly useful for comparing and classifying systems.

2.4. Control System

Accurate control of hydraulically actuated structural systems presents significant challenges due to the inherent nonlinear behavior of hydraulic components. Additionally, as the actuator excites the structure, the structure simultaneously reacts back onto the piston, introducing a dynamic back-loading/back-pressure effect. This interaction imposes additional time-varying forces on the actuator, further increasing the complexity of the response.

The primary sources of nonlinearity in hydraulic systems include fluid compressibility, nonlinear flow–pressure relationships, and friction in moving components. As mentioned in Section 2.2, fluid compressibility introduces compliance into the hydraulic circuit, affecting the dynamic stiffness of the actuator. Valve flow characteristics are typically nonlinear and depend on both the pressure drop and the spool position. Friction and internal leakage further contribute to non-smooth behavior, particularly at low velocities.

An additional layer of complexity arises from uncertainties in the plant, particularly in the soil–structure interaction. Soil modeling and characterization are inherently uncertain; while a full geotechnical exploration is required for accurate characterization, in practice, it is often based on correlations from Cone Penetration Tests (CPTs), which provide only approximate estimates.

Environmental and logistical constraints in offshore conditions further complicate implementation. These include limitations in the number and placement of sensors, robustness and reliability of data acquisition (DAQ) systems, communication delays, and challenges in maintaining stable control under variable environmental conditions.

Given these challenges, control strategies must be robust to both the nonlinear dynamics of the hydraulic system and uncertainties in the structural and soil parameters. While advanced methods, such as nonlinear frequency-shaping schemes, robust/adaptive control, and model predictive control, can theoretically provide improved performance, they typically require precise plant modeling, extensive feedback and/or careful tuning, factor may not be feasible to implement givent the system requirements [51, 52].

The system must instead be adaptable to real-world conditions with minimal sensors and feedback, enabling straightforward modification and reliable implementation in industry

Considering these practical constraints, this thesis employs a Proportional-Integral-Derivative (PID) controller, a widely used control strategy in industry due to its simplicity, ease of tuning, and robustness to modeling inaccuracies. Despite its straightforward nature, PID control can achieve satisfactory performance even in systems exhibiting nonlinearities and uncertainties, making it a practical and reliable choice for hydraulic-actuated structural applications [53].

PID controllers are estimated to account for approximately 90% of all control schemes in industrial applications, owing to their low cost, simplicity, and ease of hardware implementation [**PID_tuning**]. A significant advantage of PID controllers is that they do not require an explicit mathematical model of the plant dynamics to operate effectively, thereby enhancing their robustness

A PID-based controller operates by continuously computing the error between a desired trajectory or set-point, $y_{\text{ref}}(t)$, and a measured process state, $y(t)$. A correction is then applied to the input based on three components: the **Proportional (P)**, **Integral (I)**, and **Derivative (D)** terms.

Mathematically, the control signal for the PID controller is defined as follows:

$$e(t) = y_{\text{ref}}(t) - y(t) \tag{2.59}$$

$$u(t) = K_P e(t) + K_I \int_0^t e(\tau)\, d\tau + K_D \frac{d}{dt} e(t) \tag{2.60}$$

$$u(t) = K_P \cdot P + K_I \cdot I + K_D \cdot D \tag{2.61}$$

Where:

- K_P is the proportional gain, determining the response to the current error.
- K_I is the integral gain, determining the response based on the accumulated error over time.

- K_D is the derivative gain, determining the response to the rate of change of the error.

Alternatively, the gains can be expressed in the 'Time Constant Formulation'

$$u(t) = K_C \left[e(t) + \frac{1}{T_i} \int_0^t e(\tau)\, d\tau + T_d \frac{de(t)}{dt} \right] \tag{2.62}$$

$$u(t) = K_C \cdot P + \frac{K_C}{T_i} \cdot I + K_C T_d \cdot D \tag{2.63}$$

Here, K_C is the controller gain T_i the integral time, and T_d the derivative time.

This formulation expresses the gains in terms of response times, indicating how quickly each action affects the system. This formulation can lead to a more intuitive tuning, as it time-based and does not use dimensionless gains.

2.4.1. PID Enhancements

The PID controller is inherently linear, therefore, its performance for nonlinear processes may not be satisfactory on its own, and often needs to be supplemented with feed-forward terms, gain scheduling, adaptive tuning methods, or other advanced techniques [54].

In particular, the following modifications are implemented to improve the performance of the controller:

- **Feedback linearization**
  Let us consider a nonlinear process described by

  $$\dot{\mathbf{x}} = f(\mathbf{x}) + g(\mathbf{x})\mathbf{u},$$

  where $\mathbf{x}$ is the state vector, $\mathbf{u}$ is the control input, and f and g are nonlinear functions of the state.

  If the nonlinear function $g(\mathbf{x})$ can be accurately identified and modeled, the system can be linearized through a nonlinear input transformation:

  The process can be linearized as follows [1]

  $$\mathbf{u} = g(\mathbf{x})^{-1} \left(-f(\mathbf{x}) + \mathbf{v} \right) \tag{2.64}$$

  here $\mathbf{v}$ is a new control input designed for the linearized system.

- **Feed-forward**
  Given that a feedback controller relies solely on the error $e(t)$ to compute the control signal $U(t)$, it cannot predict or anticipate process behavior. This limitation means that the controller cannot anticipate changes in the system's behavior. As a result, the system may experience overshoot, where the output temporarily exceeds the target value, or oscillations during the transient phase before settling at steady state. These effects can complicate the tuning process, as the system may exhibit undesirable dynamics until it reaches equilibrium.

  By adding a feed-forward term, which directly accounts for known reference changes or predictable disturbances, the controller can act proactively rather than reactively. This helps reduce overshoot, improve response time, and ease the tuning. The feed-forward term is mathematically expressed as

  $$U_{ff}(t) = K_{ff}\, y_{\text{ref}}(t),$$

  where K_{ff} is the feed-forward gain.

- **Filtered Derivative**
  To improve robustness against measurement noise and to prevent excessive control action from the derivative term, a filtered version of the derivative is typically used. A common approach is to apply a first-order low-pass filter to the derivative action [53]:

  $$\mathcal{D}_{\text{filtered}}(s) = \frac{K_d\, s}{\tau_{K_d} s + 1} \mathcal{E}(s), \tag{2.65}$$

[1] $g(\mathbf{x})$ could be non-invertible (most likely discontinuous or non-differentiable), therefore computing a true inverse may not be possible and a pseudo inverse is used.

where τ_{Kd} is the filter time constant, and $\mathcal{E}(s)$ is the Laplace transform of the error signal. Alternatively, traditional approaches involve either using causal filters or setting a threshold for the maximum derivative action [54].

- **Anti-Windup**
  Integral windup occurs when the integral term continues to accumulate error after the control action reaches saturation, leading to excessive overshoot and delayed recovery. To prevent this, a simple *anti-windup* strategy can be employed.

$$\frac{d}{dt}(I) = K_I e(t) + K_{aw}\left(U_{sat}(t) - u(t)\right)$$

  with

  - $I(t)$: the integral state,
  - K_i: the integral gain,
  - $e(t)$: the control error,
  - $u(t)$: the control signal before applying actuator saturation,
  - $U_{sat}(t)$: the actual (saturated) control signal,
  - K_{aw}: the anti-windup gain, which tunes how fast the correction acts.

2.4.2. Block Diagrams

Control systems are often represented using block diagrams, which provide a visual framework for understanding the relationships between components and the flow of signals through feedback loops. Each block typically corresponds to a specific subsystem, described mathematically by a transfer function or operator. While the blocks with the transfer function will generally be self-evident, there are a few specific cases that require further clarification.

To facilitate understanding, a set of standard symbols and connection elements are used to represent common operations, such as summation, feedback, and signal branching. The following conventions will be adopted throughout this work:

- **Addition**: Represent addition or subtraction of signals

Figure 2.9: Addition junction

- **Multiplication** Represent multiplication of signals

Figure 2.10: Multiplication junction

- **Gain** Represent multiplication by a constant (K)

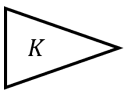

Figure 2.11: Gain block

Other blocks such as integrators, derivatives, and general transfer functions will also be included and labeled as needed. It is important to note that the block diagrams may include signals represented in either the time domain or the Laplace (complex) domain, depending on the context. The domain will be chosen to best clarify the behavior or relationship described by each block.

2.4.3. State Determination

Accurately determining the state of a dynamic system is essential for implementing a control system . System states can be predicted using numerical integration techniques, such as time-stepping schemes, while nonlinear systems typically require iterative prediction methods. Several strategies are available, with the following being commons approaches[55].

Predictor-Corrector Method

The Predictor-Corrector(P-C) method improves the accuracy of whichever numerical integration is used by combining a prediction step with a correction step.

Consider a system described by

$$\dot{\mathbf{x}}(t) = f(\mathbf{x}(t), \mathbf{u}(t)), \tag{2.66}$$

where $\mathbf{x}(t)$ is the state vector and $\mathbf{u}(t)$ is the input. The predictor step estimates the next state using an explicit method, for example forward Euler:

$$\mathbf{x}_{k+1}^{\text{pred}} = \mathbf{x}_k + \Delta t\, f(\mathbf{x}_k, \mathbf{u}_k), \tag{2.67}$$

and the corrector step refines this estimate using the derivative at the predicted state:

$$\mathbf{x}_{k+1} = \mathbf{x}_k + \frac{\Delta t}{2}\Big(f(\mathbf{x}_k, \mathbf{u}_k) + f(\mathbf{x}_{k+1}^{\text{pred}}, \mathbf{u}_{k+1})\Big), \tag{2.68}$$

where Δt is the time step.

Kalman Filter

Similar to the P-C method, the Kalman filter (KF) also employs a prediction and correction strategy. However, it provides a recursive algorithm based on Bayesian estimation for determining the system states in the presence of measurement noise, defined as follows:

Consider a discrete-time linear system:

$$\mathbf{x}_{k+1} = A\mathbf{x}_k + B\mathbf{u}_k + \mathbf{w}_k, \tag{2.69}$$

$$\mathbf{y}_k = C\mathbf{x}_k + \mathbf{v}_k, \tag{2.70}$$

where $\mathbf{w}_k$ and $\mathbf{v}_k$ are process and measurement noise with covariances Q and R, respectively. The Kalman filter alternates between a prediction step:

$$\hat{\mathbf{x}}_{k|k-1} = A\hat{\mathbf{x}}_{k-1|k-1} + B\mathbf{u}_{k-1}, \tag{2.71}$$

$$P_{k|k-1} = AP_{k-1|k-1}A^\top + Q, \tag{2.72}$$

and a correction step:

$$K_k = P_{k|k-1}C^\top\big(CP_{k|k-1}C^\top + R\big)^{-1}, \tag{2.73}$$

$$\hat{\mathbf{x}}_{k|k} = \hat{\mathbf{x}}_{k|k-1} + K_k\big(\mathbf{y}_k - C\hat{\mathbf{x}}_{k|k-1}\big), \tag{2.74}$$

$$P_{k|k} = (I - K_kC)P_{k|k-1}, \tag{2.75}$$

where K_k is the Kalman gain, $\hat{\mathbf{x}}_{k|k}$ is the corrected state estimate, and $P_{k|k}$ is the corresponding error covariance.

The KF method can be extended to nonlinear system by considering modified version such as Extended Kalman Filter (EKF) and Unscented Kalman Filter (UKF) [56].

3

Dynamics of the Coupled System

3.1. SDOF System

Having characterized the individual subsystems, we now focus on analyzing the coupled system, specifically the Single Degree of Freedom (SDOF) structure. The system under consideration consists of an mass-stiffness oscillator coupled to a power-hydraulic system, where the valve is excited by a voltage input $U(t)$, which is illustrated in Figure 3.1.

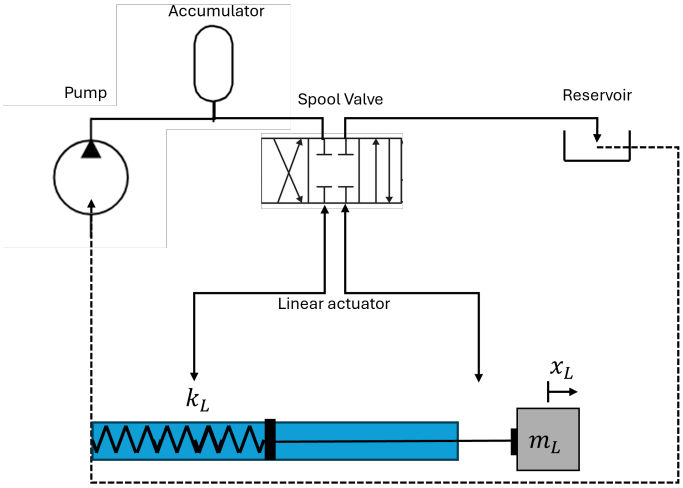

Figure 3.1: SDOF coupled to power hydraulic

Lets consider that the input signal is defined as

$$U(t) = A\cos(2\pi t + \phi)$$

3.1.1. Linearized System

As a first approach, let's consider the linearized system, that can be represented by the diagram in figure 3.2

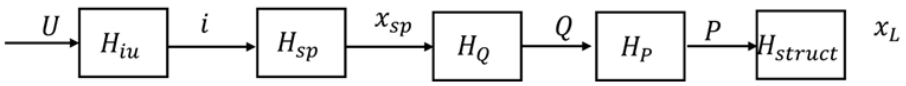

Figure 3.2: Linearized SDOF system

Given that the system is linear and cascading, the solution can be easily obtained in the complex domain, as determine by

$$\frac{\mathcal{L}\{x_L\}}{\mathcal{L}\{U\}} = \mathcal{H}_{Ux_L} = \prod_{k=1}^{n} \mathcal{H}_k \tag{3.1}$$

with $\mathcal{H}_i$ the transfer function of the subsystems between U and x_L.

The transfer function of each of the individual systems can be obtained from the models of each component, as described in Chapter 2, specifically:

1. **Control Signal - Current**
   The Transfer Function i s directly extracted from the modeling equation (2.42), as the dynamics describing the subsystem were originally defined in the Laplace domain

   $$\mathcal{H}_{Ui} = \frac{K_{iU}}{\tau_{iU}s + 1} \tag{3.2}$$

2. **Current - Spool**
   The linearized dynamics, ignoring the polarity and directionality effects, can be directly extracted from the original formulation in expression (2.48)

   $$\mathcal{H}_{ix_{sp}} = \frac{K_{ix_{sp}}}{\tau_{ix_{sp}}s+1} \tag{3.3}$$

3. **Spool - Flow and Pressure**
   The Transfer Function between the spool opening and flow cannot be directly obtained, as Q depends on P which is a variable down the line. This can be easily fixed by instead considering the transfer function between x_{sp} and P.

   However, as it was shown in equation (2.32) the relationship between Q and P is nonlinear. And, the notion of transfer function is traditionally only applicable for linear systems, therefore it is necessary to linearize the expression by consider a small perturbation around the operating point (x_{sp}^0, P^0) defined by

   $$P = P^0 + \delta P$$
   $$x_{sp} = x_{sp}^0 + \delta x_{sp}^0$$

   Then, the linearized flow is

   $$Q(t) = x_{sp}K_q\sqrt{1 - \frac{P}{P_s}} \tag{3.4}$$

   $$Q \approx x_{sp}K_q \left(\sqrt{1 - \frac{P^0}{P_s}} - \frac{x_{sp}^0}{2\sqrt{1 - \frac{P_0}{P_s}}} \frac{\Delta P}{P_s} \right) \tag{3.5}$$

   Then, following expression is obtained.

   $$\mathcal{H}_{spP} = \frac{\frac{K_q}{K_l}\sqrt{1 - \frac{P^0}{P_s}}}{s - \frac{K_e}{K_l} + \frac{K_q/K_l}{2P_s\sqrt{1 - \frac{P^0}{P_s}}}} \tag{3.6}$$

   A common simplification is to consider that $P_0 \ll P_s$ such that the systems does not produce any feedback, meaning that the actuator is *stronger* than the structure [57, 35].

Which simplifies the expression to

$$\mathcal{H}_{spP} = \frac{\frac{K_q}{K_l}}{s - \frac{K_e}{K_l} + \frac{K_q}{K_l}}$$

4. **Pressure - Displacement**
   The Transfer Function can be directly obtained by applying the Laplace Transform to the ODE describing the force balance of the piston.

$$\mathcal{H}_{Px_L} = \frac{A}{m_L s^2 + cs + k} \tag{3.7}$$

Then, solution for the linearized system is obtained by inverting the Transfer Function of the whole system:

$$\begin{aligned} \mathcal{L}\{x_L\} &= \mathcal{H}_{Ux_L}\,\mathcal{U} \\ x_L &= \mathcal{L}^{-1}\left\{\mathcal{H}_{Ux_L}\,\mathcal{U}\right\} \\ x_L &= \mathcal{L}^{-1}\left\{\prod_{i=1}^{n}\mathcal{H}_i\right\} \end{aligned}$$

Although useful for characterizing the full system, determining poles, evaluating stability, and designing potential control schemes, expressing the solution in the complex domain has several limitations. Primarily, it can only be applied to linear systems. As such, it is used exclusively for benchmarking purposes and to verify the results obtained by solving the system using other methods.

In contrast, the system will be expressed in the time domain as a set of coupled first-order ordinary differential equations (ODEs), using the State Space formulation as defined in 2.2. This representation offers a few advantages such as

- It allows easy adaptation and expansion to a nonlinear system.
- It provides a natural framework for extending the system to a MIMO system.
- It facilitates the analysis of time-varying systems.

Space State Formulation

The state vector is defined as

$$\mathbf{x}_A^T = \begin{bmatrix} x_L & \dot{x}_L & P & x_{sp} & i \end{bmatrix} \tag{3.8}$$

It must be mentioned that the second order ODE representing the dynamics of the piston (equation (2.37) was converted to two coupled first order ODEs, by incorporating a new state and using a dummy variable, as it is commonly done to reduce the order of linear ODEs.

Utilizing the convention established in Section 2.1 and the dynamics of each subsystems defined in Section 2.2, the State Space representation of the linearized SDOF system can be defined as

$$\dot{\mathbf{x}}_A = \mathbf{A}_A\mathbf{x}_A + \mathbf{B}\mathbf{y} \tag{3.9}$$

$$\frac{d}{dt}\begin{bmatrix} x \\ \dot{x} \\ P \\ x_{sp} \\ i \end{bmatrix} = \begin{bmatrix} 0 & 1 & 0 & 0 & 0 \\ 0 & -b/m_L & A/m_L & 0 & 0 \\ 0 & -A/K_l & K_e/K_l & K_q/K_l & 0 \\ 0 & 0 & 0 & -1/\tau_{ix_{sp}} & K_{ix_{sp}}/\tau_{ix_{sp}} \\ 0 & 0 & 0 & 0 & -1/\tau_{Ui} \end{bmatrix}\begin{bmatrix} x \\ \dot{x} \\ P \\ x_{sp} \\ i \end{bmatrix} + \begin{bmatrix} 0 \\ 0 \\ 0 \\ 0 \\ K_{iU} \end{bmatrix} U(t) \tag{3.10}$$

with the following system properties:

Table 3.1: System properties

Description	Symbol	Value	Units
SDOF mass	x_L	52.7	Kg
SDOF viscous damping	b_L	225	Nm/s
SDOF stiffness	k_L	$2.11 \cdot 10^5$	N/m
Chamber cross section	A	1303	mm
Flow-Force rate gain	K_l	$7.89 \cdot 10^{-2}$	mm^3/N
Flow-Force gain	K_e	3.24	mm^3/s/N
Flow rate gain	K_q	$5 \cdot 10^{-3}$,	$m^3/s/\% \cdot 10^{-6}$
Current gain	K_{Ui}	2	mA/V
Time constant of current	τ_{Ui}	0.0018	s
Time constant of spool	τ_{ix}	0.002	s
Excitation amplitude	$\|U\|$	10	V

The parameters listed in Table 3.1 are derived from the system described in [40], which includes experimental results. These parameters serve as a benchmark for our implementation, allowing for a comparison with the linear SDOF model before extending to the nonlinear system.

3.1.2. Features of the Linear System

In this section, the main characteristics of the system response are identified, and methods for analyzing and post-processing the results are proposed. The objective is to establish a systematic framework for evaluating the system's dynamic behavior under linear assumptions, which will serve as a reference point for comparison against the nonlinear case. .

Considering the system defined by equation (3.9) and the properties stated in Table 3.1, the steady state response is expected to be linear (see equation (2.17)), prediction which aligns with the response shown in Figure 3.3.

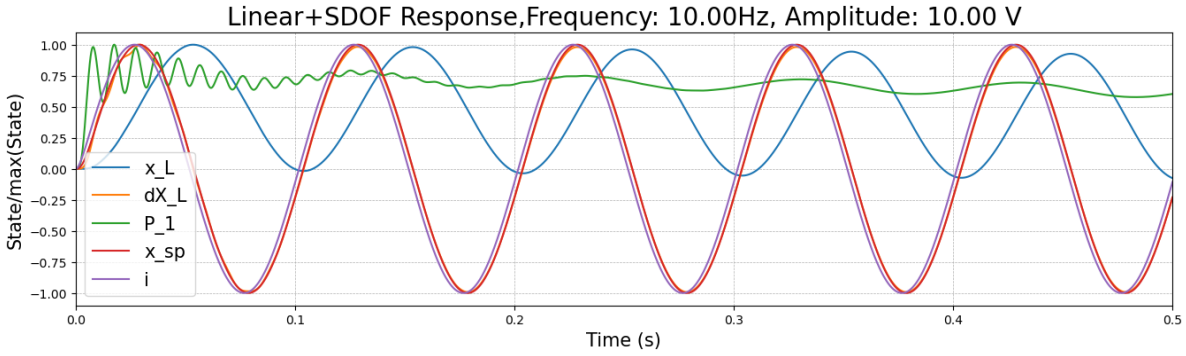

Figure 3.3: Time response of the linear system to voltage signal

Figure 3.3 presents the normalized time response of the system. The initial transient pressure response lasts approximately 0.2 s before decaying to its steady-state behavior. A minor phase delay is observed between i and x_{sp}, which aligns with the expected time constant ($\tau_{ix_{sp}}$) governing their interaction.

A greater phase shift is evident between the electrical and hydraulic subsystems, causing the valve opening and pressure response to lag behind the voltage signal. This response align with the experimental result describe in [40]

Naturally, it is essential to characterize the system across the full frequency range to capture its dynamic characteristics. To this end, the Frequency Response Function (FRF), is computed and shown in Figure 3.4.

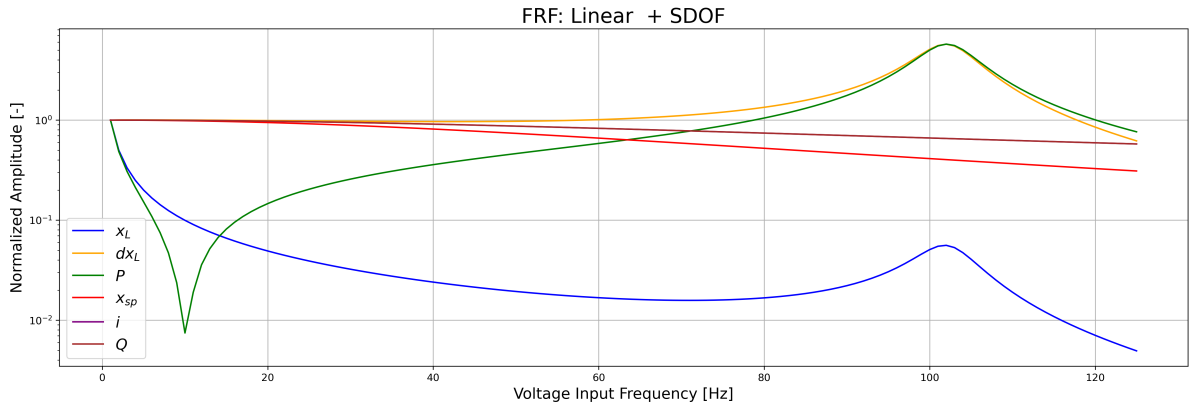

(a) Normalized Amplitude FRF

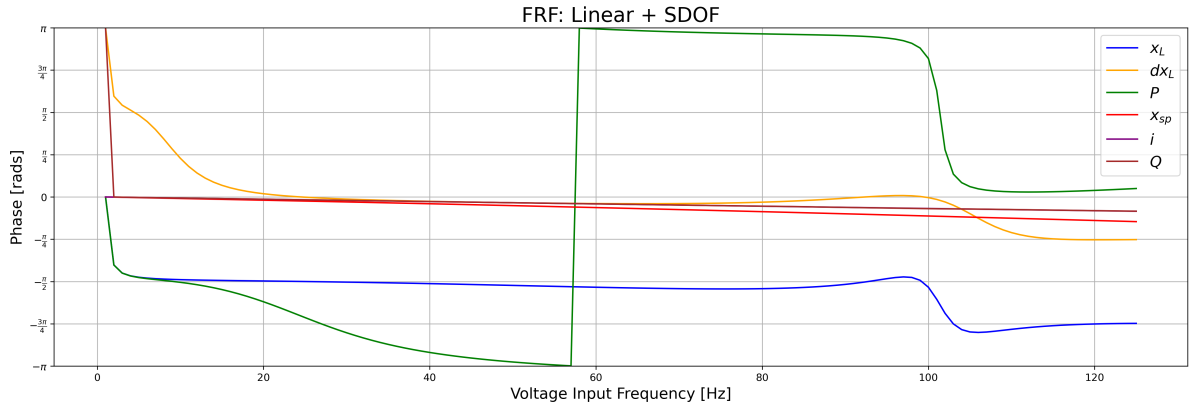

(b) Phase FRF

Figure 3.4: Frequency Response Function of the linear system.

Given that we are interested in a general characterization of the response, the amplitude spectrum is normalized as follows

$$\mathcal{H}_i^{norm} = \frac{\mathcal{H}_i(jf_k)|}{\mathcal{H}_i(jf_0)}$$
$$x_i \in \mathbf{x}_a$$
$$f_k \in f = (f_0, f_f)$$

In Figure 3.4, two distinct dynamics can be observed

1. **SDOF Resonance**
   It can be seen that around $f = 10.5$ Hz, the pressure experiences an anti-resonance, this is caused by the resonance mass-stiffness of the SDOF, determined by

   $$f_{n=1} = \frac{1}{2\pi}\sqrt{\frac{k_L}{m_L}} = 10.5Hz$$

   This anti-resonance, can be also treated as classical resonance if it is considered that the input of the systems is the force (pressure) and the displacement of the piston mass is the output.

   $$\mathcal{H}_{\text{uncoupled}} = \frac{\mathcal{L}\{\ x_L\}}{\mathcal{L}\{P\}} \tag{3.11}$$

   However, this framing is not appropriate in this work because while structural dynamics typically treats externally applied forces (e.g., piston force) as prescribed inputs, this work explicitly models

the coupling between the piston and the structure. This coupling becomes non-negligible when the relative *strength* the subsystems do not differ significantly, which is the central point of this thesis.

Henceforth, the force (pressure) is a resulting variable from the interaction between the hydraulic and structural subsystem and not as an externally imposed input. Therefore, treating force as an input is conceptually incorrect. A more accurate representation of the system input is the voltage or control signal driving the valve.

Additionally, this aligns with the physical interpretation that an input is a quantity that carries energy into the system. In the case of the coupled system, the input is the control signal to the valve, which governs the pressurized flow entering the system. This flow represents the actual transfer of power into the structure, making the control signal, not the force or pressure, the appropriate input from both a conceptual, modeling and energy standpoint.

The physical mechanism that explains why the $|x_L| - |P|$ resonance is observed as $|P| - |U|$ anti-resonance in because at resonance, the piston experiences larger displacements, which increase the chamber volume, leading to a corresponding decrease in pressure.

2. **Oil Column Resonance**
   At $f \approx 101.5Hz$ a resonance peak can be observed in the pressure, displacement and velocity response. This phenomena is undesirable as it could amplify unwanted frequency that otherwise would have a very small response. In practice, it is recommended to avoid exciting frequency that are in $(0.8f_{oil}, 1.2f_{oil})$ range [58].

   This is caused by the compressibility of the oil, the value at which this occurs can be estimated by

$$f_{oil} = \frac{1}{2\pi}\sqrt{\frac{4\beta_e A_L}{L_L m_L}} \approx 101.5Hz \tag{3.12}$$

Flow as Intermediate Variable

It is important to note that Figure 3.4 presents the FRF for six variables, whereas the state vector defined in equation (3.8) consists of five states. The additional variable corresponds to the flow response, which is included even though it is not part of the state vector.

This difference arises from the inclusion of the flow variable (Q), which is reconstructed after solving the system, in this particular case the linearized form of equation (2.32), according to what was established in subsection 3.1.1.

Evidently, Q is proportional to x_{sp}, scaled only by the Flow Gain in the linearized SDOF case. However, in nonlinear systems, the relationship between flow, pressure, and valve opening becomes significantly more complex and plays a critical role in the development of an effective control strategy. Specifically, reconstructing the flow signal becomes important for two main reasons:

1. **Degree of nonlinearity**
   As previously mentioned, the nonlinear flow relationship is the primary source of nonlinearity in the system. Therefore, analyzing its behavior is essential to understanding the overall system dynamics. In particular, plotting the valve characteristics, represented by $x_{sp}(t)$ vs $Q(t)$, provides a means to estimate the degree of nonlinearity.

   For a weakly nonlinear response, this can be further quantified by computing the Pearson correlation coefficient ($\hat{\rho}$).

   Figure 3.5 shows the flow characteristic corresponding to the response of the system described in Figure 3.3

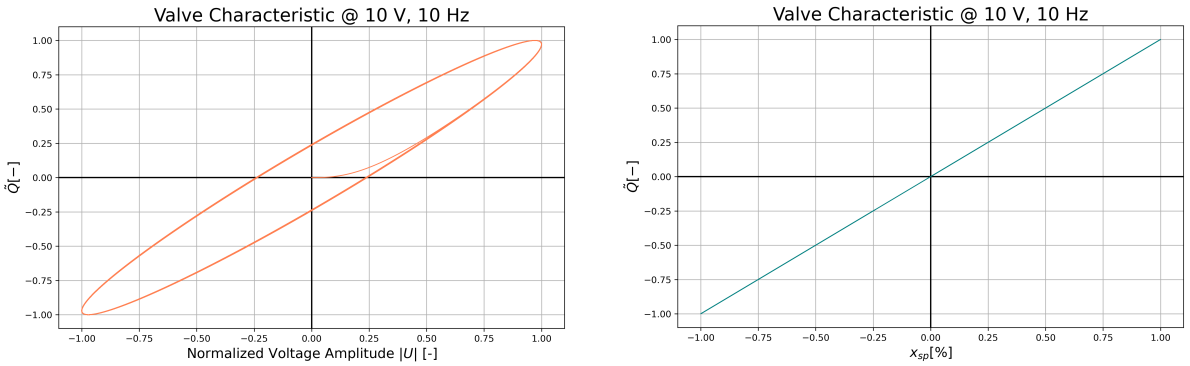

(a) Input - Flow Characteristic

(b) Valve opening - Flow Characteristics

Figure 3.5: Flow Characteristics

Figure 3.5 illustrates two possible ways to define the valve characteristics, corresponding to different Lissajous curves.

(a) The first approach, shown in Figure 3.5a, depicts the relationship between the input signal (voltage) and the flow to the actuator. This curve corresponds to an ellipse, which is characteristic of a linear systems with delay.

(b) The second approach, shown in Figure 3.5b, represents the relationship between the valve opening $x_{sp}(t)$ and the resulting flow $Q(t)$. In our model (see equation 2.32), the flow responds linearly and instantaneously to changes in the valve opening.

By analyzing both types of Lissajous curves, it is possible to quantify system behavior in terms of delay and nonlinearity.

For weakly nonlinear responses, the Pearson correlation coefficient defined in (3.13), provides a metric that quantifies deviation from linearity.

$$\hat{\rho}(Q, x_{sp}) = \frac{\sum_{i=1}^{n}(Q_i - \bar{Q})(x_{sp,i} - \overline{x}_{sp})}{\sqrt{\sum_{i=1}^{n}(Q_i - \bar{Q})^2}\sqrt{\sum_{i=1}^{n}(x_{sp,i} - \overline{x}_{sp})^2}} \tag{3.13}$$

Although, as will be demonstrated, the relationship between input voltage and valve opening is nonlinear, the use of expression (3.13) implicitly assumes the absence of other significant nonlinear effects. Under the assumption that the primary source of nonlinearity in the system comes from the flow equation, this metric provides a reasonable approximation of the system's overall degree of nonlinearity.

Furthermore, it is crucial to note that, as indicated by equation (2.32), the flow depends on both the pressure (P) and valve opening (x_{sp}). However, this approach only quantifies the relationship between flow and valve opening, not pressure directly.

Therefore, as the nonlinear behavior of the system becomes more pronounced, the coupling between pressure and flow begins to have non-negligible effects, making the correlation a less representative metric of the quantification of the overall system nonlinearity.

2. **Power Consumption**
Within the coupled system only two sub-systems directly consume power, the pump that pressurizes the systems and the spool valve. However, the spool valve power consumption is negligible (5V @ 2 mA) compared to the power consumption of the pump , therefore it will be assumed that the total power consumption of the system is equivalent to the power consumption of the pump.

The instantaneous power consumed by the pump can be estimated by

$$P^{\text{hydraulic}}(t) = \frac{dW}{dt} \tag{3.14}$$

$$P^{\text{hydraulic}}(t) = \frac{PdV}{dt} \tag{3.15}$$

Given that the supplied pressure can be considered to be constant (see expression (2.19)), and considering that the efficiency of the system is η_{total}, the power consumed by the system is

$$P^{\text{pump}}(t) = \frac{1}{\eta_{\text{total}}} P_s Q(t)$$

In some circumstances, instantaneous power may not provide the most meaningful measure of system performance, as it does not account for effects such as the accumulator dynamics and unmodeled pump behavior. In these cases, the average power provides a more appropriate metric, defined aa

$$\bar{P}^{\text{pump}}(\Delta t) = \frac{P_s}{\eta_{\text{eff}}} \cdot \frac{1}{\Delta t} \int_t^{t+\Delta t} Q(t)\, dt$$

Besides power consumption, it is important to consider how power is transferred and transformed within the system. A simplified schematic illustrating the different stages of power flow is presented in Figure 3.6.

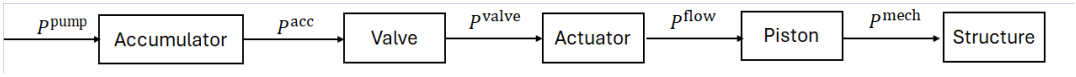

Figure 3.6: Diagram of power flow through the system

Figure 3.6 distinguishes between the power supplied to the actuator and the power transferred to the structure. This distinction is particularly important in the nonlinear system and is defined by

$$P^{\text{actuator}}(t) = P(t)Q(t) \tag{3.16}$$

$$P^{\text{mech}}(t) = [P(t)A]\, \dot{x}_L(t) \tag{3.17}$$

Naturally, by conservation of energy, the following inequality holds:

$$\bar{P}^{\text{pump}} \geq \bar{P}^{\text{acc}} \geq \bar{P}^{\text{valve}} \geq \bar{P}^{\text{flow}} \geq \bar{P}^{\text{mech}} \tag{3.18}$$

A more accurate representation of the power flow from the pump to the structure can be expressed as

$$\bar{P}^{\text{mech}} = \bar{P}^{\text{pump}} \prod_j \eta_j \tag{3.19}$$

where η_j represents the efficiency of each subsystem. Although this formulation provides the correct approach for estimating mechanical power transfer, it is not directly applicable to the present work, since the power efficiency of each subsystem is typically determined empirically. Nevertheless, it is important to state this relationship for completeness.

3.1.3. Nonlinear System

To more accurately represent the system dynamics, several sources of nonlinearity will be added to the model. This will capture behaviors often neglected in linear formulations, which assume no actuator-plant coupling, an assumption that does not apply here.

The following nonlinear elements will be included:

1. **Non Linear Flow**
   The flow through the valve will now be modeled considering the coupling of the pressure in the actuator and flow provided to it . Additionally, a directionally coefficient taking into account flow reversal effects will be considered, in specific the hyperbolic tangent model, as shown in Figure(3.20)

$$Q(t) = \begin{cases} \left(x_{sp}(t) K_q \sqrt{1 - \left| \frac{P(t)}{P_s} \right|} \right) sgn(x_s), & \text{if } P(t) > P_s, \\ \left(x_{sp}(t) K_q \sqrt{1 - \left| \frac{P(t)}{P_s} \right|} \right) sgn(x_s) \left(\frac{1 + \tanh\left(-\beta_Q \left(\frac{P(t)}{P_s} - 1 \right) \right)}{2} \right), & \text{otherwise.} \end{cases} \tag{3.20}$$

   Although two valve reversal models were initially considered (2.7), the difference in their effects on the system dynamics was found to be minimal. Therefore, the hyperbolic formulation was chosen

2. **Valve Dead-zone** A dead-zone is a nonlinearity commonly found in control systems, especially in actuators and valves, where an increase in the magnitude of the control signal around an operating point does not produce any output response. This phenomena is usually the result of manufacturing tolerances, friction, stiction, imperfections,etc [59].

   This phenomenon usually appears as a lack of responsiveness in the region where the control signal is near zero. For the system under study, the dead zone can be modeled as:

$$x'_{sp}(t) = x_{sp} \cdot DZ(x_{sp}(t)) = \begin{cases} x_s \left(m_r \cdot (x_{sp}(t) - b_{DZ} \right) & \text{if } x_{sp}(t) > b_{DZ}, \\ 0 & \text{if } |x_{sp}(t)| \leq b_{DZ}, \\ x_{sp} \left(m_t \cdot (x_{sp}(t) + b_{DZ}) \right) & \text{if } x_{sp}(t) < -b_{DZ}, \end{cases} \tag{3.21}$$

   - b_{DZ}: Dead-zone threshold (as a percentage of the maximum x_{sp}), below which the system produces no output response.
   - m_r and m_t: Gains of the system for positive and negative inputs, respectively.

   For simplicity, and assuming a critically centered valve, it is reasonable to set $m_r = m_t = 1$. This assumption makes the dead-zone-affected region symmetric around the condition $|x_{sp} - b_{DZ}| < 0$.

3. **Valve Hysteresis**
   Another nonlinear effect that could potentially affect the valve's dynamics is hysteresis. This phenomenon arises from the same underlying physical mechanisms as backlash. Hysteresis causes the valve to respond not only to its current input but also to its previous states, resulting in path-dependent behavior. A variety of models exist to describe hysteresis in mechanical and hydraulic systems, such as the Prandtl-Ishlinskii and the Preisach model, among others [60, 61].

   Identifying and estimating the specific hysteresis characteristics of a given valve or actuator is a complex and non-trivial task. Nevertheless, accurate modeling of hysteresis is crucial, as it can significantly impact overall system dynamics, thereby degrading both controllability and response [59, 62].

   Therefore, in the absence of a detailed valve model or experimental data, the simplest hysteretic model, backlash, is implemented.

$$BK(x'_{sp}, x''_{sp}) = \frac{dx''_{sp}}{dt} = \begin{cases} 0, & \text{if } |x'_{sp}(t) - x''_{sp}(t)| \leq \Delta_b \\ \dfrac{x'_{sp}(t) - x''_{sp}(t)}{\tau_{\text{catch up}}}, & \text{otherwise} \end{cases}$$

   Where

   - $x''(t)$: Internal state, corresponding to the actual position of the valve

- $x'_{sp}(t)$: Commanded position of the valve
- Δ_b: Backlash/play gap,
- τ_{back}: Time constant that governs how quickly the backlash state catches up with the commanded state once outside the gap.

The individual effects of backlash and dead-zone can be seen in Figure 3.7

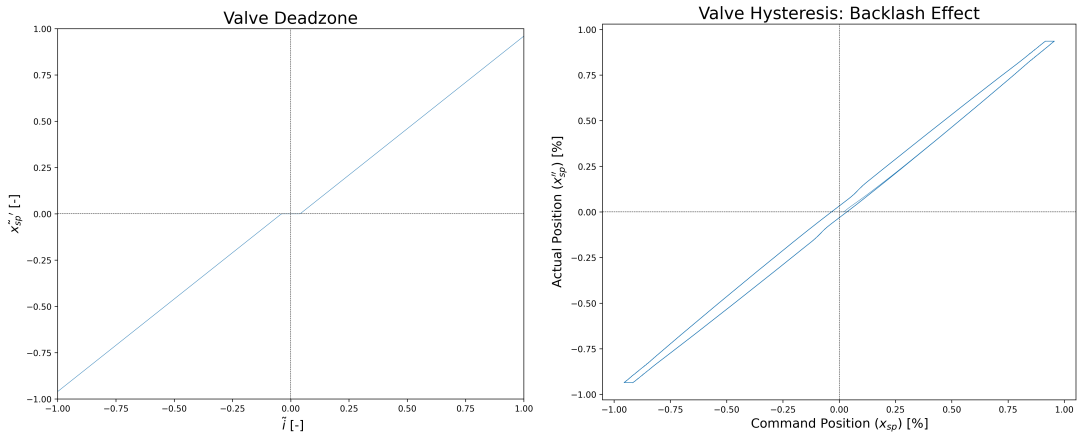

(a) Valve Dead-zone **(b)** Valve Backlash

Figure 3.7: Valve nonlinearities

An their combined effects are evident in Figure 3.8

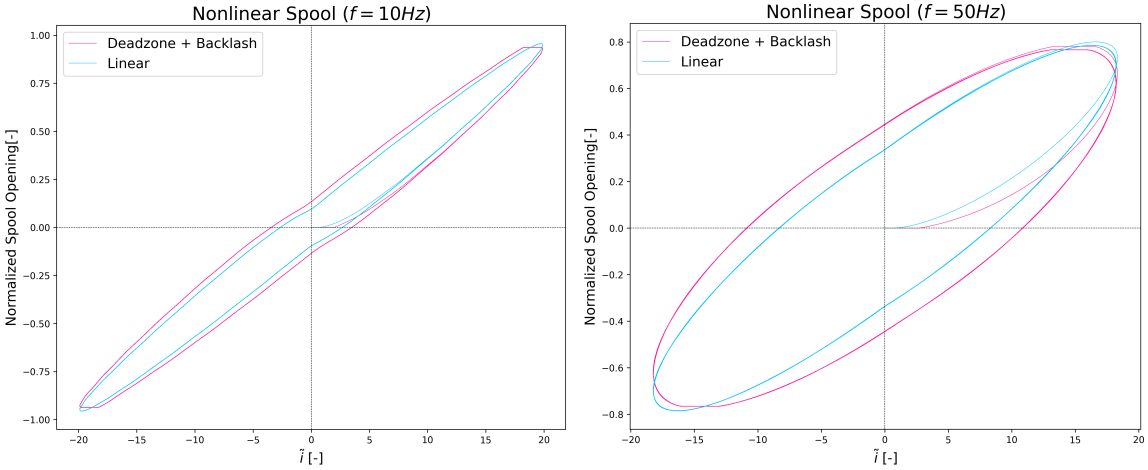

(a) $\Omega = 10Hz$ **(b)** $\Omega = 50Hz$

Figure 3.8: Effect of valve nonlinearities

At low frequencies, the effects of hysteresis and backlash are minimal, and the linear approximation remains a good representation of the system's behavior. However, as the command frequency increases, the fixed time constants ($\tau_{ix_{sp}}, \tau_{\text{catch up}}$) become more influential, and the spool's ability to respond accurately to the input diminishes. This results in a progressively larger mismatch between the input signal and the valve's output, highlighting the limitations of the system's dynamic response.

The open-loop effects of spool nonlinearity are generally smaller than those of nonlinear flow. However, these effects become more pronounced during closed-loop control, especially because they involve non-differentiable expressions, which diminish the effectiveness of pre-compensation techniques [60].

Dither Signal

Additionally, it is common practice to superimpose a dither signal, a high-frequency, low-amplitude signal, onto the control input to reduce stiction in hydraulic valves [63].

However, since a specific valve is not being studied and the valve hysteresis is explicitly modeled, a dither signal is not incorporated in the model. Accurately representing the interaction between dither and the valve dynamics would require a detailed valve-specific model, including a full tribological model of the piston and valve, which is beyond the scope of this work [64, 65].

State - Space Representation

A schematic representation of the system is shown in Figure 3.9.

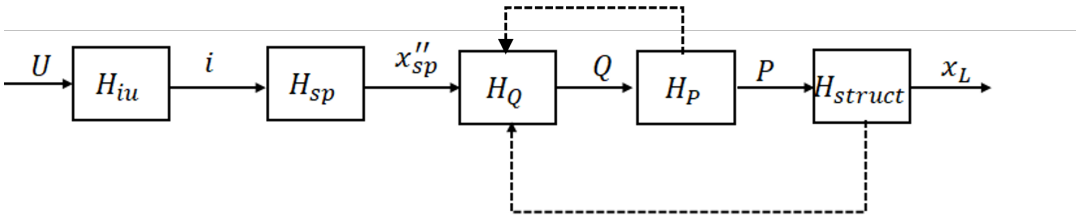

Figure 3.9: Nonlinear SDOF system

, Although at first glance the schematic appears similar to that of the linear system, but two main differences exist:

1. **Current-Valve Subsystem**
   In the nonlinear representation of the system, H_{sp} corresponds to the subsystem that transforms the input current i into a commanded spool position x_{sp}. This position is then affected by the dead zone, producing a modified spool position x'_{sp}, and subsequently by backlash, resulting in the actual spool position x''_{sp}, which corresponds to the position realized in the system.
2. **Pressure-Flow-Velocity Coupling**
   As mention before, the flow is dependent on the pressure in the system, and in the velocity of piston, therefore they are coupled, forming a nonlinear system.

Incorporating these elements, the State-Space representation of the nonlinear systems is defined by

$$\dot{\mathbf{x}}_A = \mathbf{A}_A\mathbf{x}_A + \mathbf{B}U(t) + f_{nl}(\mathbf{x}_A)$$

$$\frac{d}{dt}\begin{bmatrix} x \\ \dot{x} \\ P \\ x_{sp} \\ x''_{sp} \\ i \end{bmatrix} = \begin{bmatrix} 0 & 1 & 0 & 0 & 0 & 0 \\ 0 & -\frac{b_L}{m_L} & \frac{A}{m_L} & 0 & 0 & 0 \\ 0 & -\frac{A}{K_l} & \frac{K_e}{K_l} & 0 & 0 & 0 \\ 0 & 0 & 0 & -\frac{1}{\tau_{ix_{sp}}} & 0 & 0 \\ 0 & 0 & 0 & 0 & 0 & 0 \\ 0 & 0 & 0 & 0 & 0 & -\frac{1}{\tau_{Ui}} \end{bmatrix} \begin{bmatrix} x \\ \dot{x} \\ P \\ x_{sp} \\ x''_{sp} \\ i \end{bmatrix} + \begin{bmatrix} 0 \\ 0 \\ 0 \\ 0 \\ 0 \\ K_{iU} \end{bmatrix} U(t) + \begin{bmatrix} 0 \\ 0 \\ \frac{Q(x_{sp},P)}{K_l} \\ \frac{K_{ix_{sp}}}{\tau_{ix_{sp}}} Dz(x_{sp}) \\ BK(x'_{sp}, x''_{sp}) \\ 0 \end{bmatrix} \tag{3.22}$$

As mentioned in the introduction and reiterated in the previous section, the dominant source of nonlinearity in the system corresponds to the nonlinear relationship between flow and pressure, given by:

$$Q \propto \sqrt{1 - \frac{P}{P_s}}$$

This relationship presents a trade-off between two conflicting design objectives:

- **High supply pressure** (P_s):
  Reduces the degree of nonlinearity, making the system response more predictable and closer to linear. However, it increases energy consumption, mechanical stress, and the cost of components due to the requirements of having a sufficiently capable HPU.

- **Low supply pressure** (P_s):
  Minimizes power usage and mechanical load, but increases the nonlinear effects in the flow dynamics, which can distort the desired actuator response.

To balance these objectives, the goal is to determine the *minimum supply pressure* P_s that still allows the system to produce a *harmonic displacement response* $x_L(t)$.

This formulation aims to find the lowest viable pressure ratio that achieves an acceptable approximation of linear behavior in the actuator output, ensuring efficient performance without excessive power requirements.

In order to find this value of P_s we will start by prescribing a supplied pressure of P_{max} corresponding to the maximum operating pressure of the systems, meaning that P_s can be parametrized as

$$P_s = \alpha P_{max}, \quad \alpha \leq 1 \tag{3.23}$$

By varying α, the system can be analyzed under different supply pressure levels, and subsequently different degrees of nonlinearity.

Lets consider the system defined by the parameters specified in Table 3.1 and additional parameters corresponding to the nonlinear relationships from from Table 3.2

Table 3.2: System properties of nonlinear elements

Description	Symbol	Value	Units
Maximum Pressure	P_{max}	20.684	MPa
Dead-zone width	b_{DZ}	3	[%]
Backlash width	Δ_b	2	[%]
Backlash catch up time	$\tau_{\text{catch up}}$	0.007	[s]

Lets consider the nonlinear response at the maximum supply pressure ($\alpha = 1$)

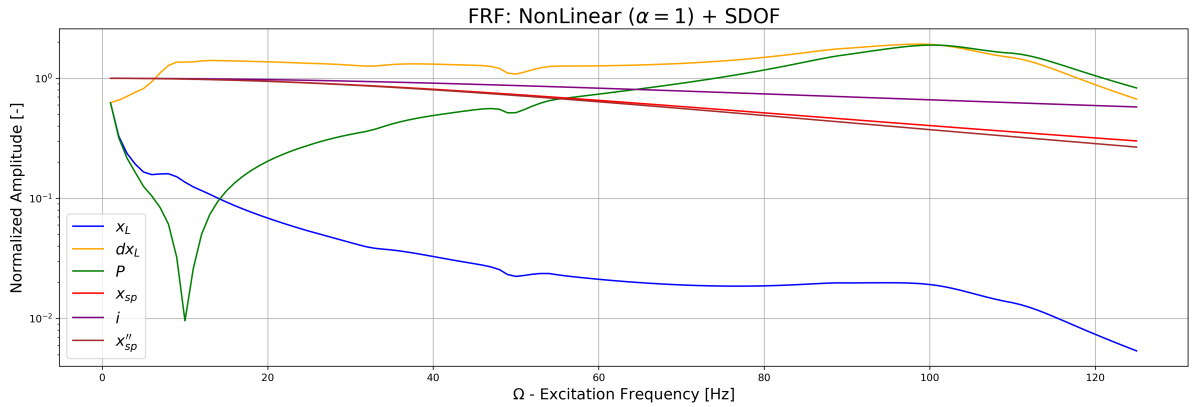

(a) Normalized Amplitude FRF

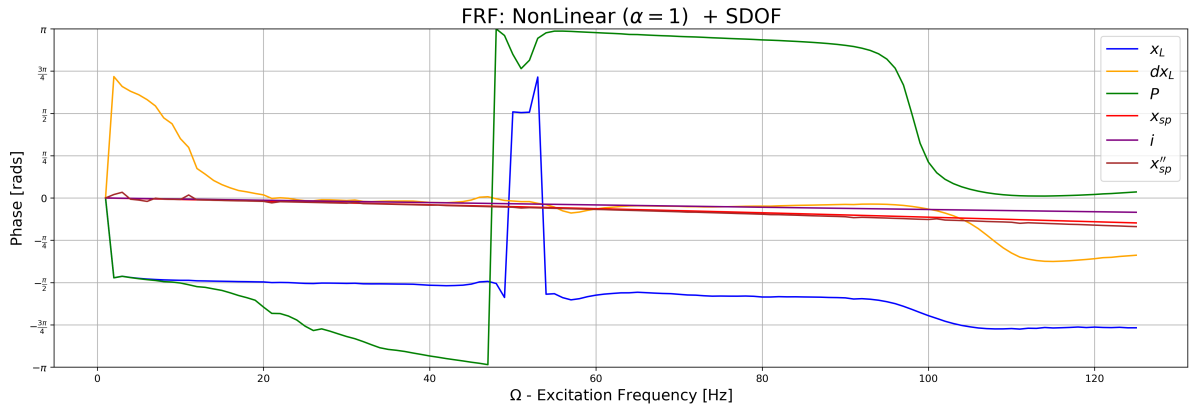

(b) Phase FRF

Figure 3.10: Frequency Response Function (FRF) to $\alpha = 1$

A preliminary analysis reveals that,when operating at the system's maximum rated pressure, the response is largely similar to the linear case, with the exception of two minor differences.

- As expected, the state corresponding to the actual spool position x''_{sp} responds akin to the commanded spool position, with a small gain and phase difference, as expected from the modeled hysteric behavior
- There exist a phase difference with respect to the linear case. This phase anomaly manifests around half the oil column resonance frequency around $f = 50hz$. Around this frequency band, some effects can be seen in the |FRF|, in particular a slight decrease in amplitude.

Frequency Response Surface

For nonlinear systems, the traditional construction of the Frequency Response Function is limited and fails to fully capture the underlying dynamics. This is because the classical FRF evaluates the system's response only at the forcing frequency, which, in the case of linear systems, is guaranteed to be the only output frequency (see equation (2.17)). However, for nonlinear systems, the response may contain multiple frequency components

Therefore, a better way to characterize the frequency contents of a nonlinear system is by examining the full spectral response of the system at each input frequency, this procedure will be defined as constructing the **2D-FRF** or Frequency Response Surface and mathematically expressed

$$\mathbf{H}(j\boldsymbol{\omega}_k) = \frac{\mathbf{Y}(j\boldsymbol{\omega}_k)}{\mathbf{U}(j\Omega_k)}$$

with $\boldsymbol{\omega}_k$ the response spectrum (FFT) corresponding to a harmonic input with frequency Ω_k.

3.2. MDOF System

Lets consider now the case of a multi-degree of freedom system (MDOF) coupled to the power hydraulic system the hydraulic sub system is coupled to a MDOF system, as Figure 3.11 shows

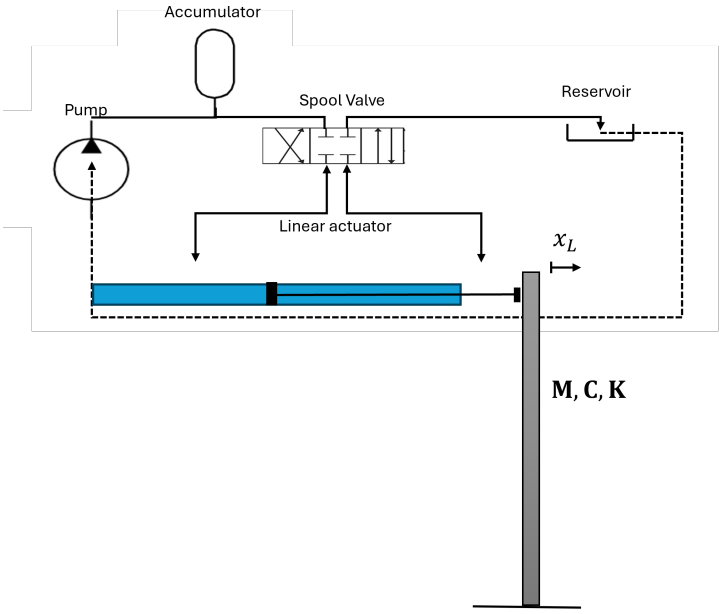

Figure 3.11: MDOF coupled to power hydraulic

The principles established for the SDOF system can be extended to the MDOF system by replacing the scalar parameters with their respective matrices and vectors.

$$k_L \longrightarrow \mathbf{K}$$
$$m_L \longrightarrow \mathbf{M}$$
$$b_L \longrightarrow \mathbf{C}$$

This formulation naturally lends itself to a substructuring approach, where the hydraulic subsystem and the structural MDOF system are treated a separate but interconnected subsystems,

3.2.1. Coupling of Subsystems

Consider that the structural system is an EB beam defined by

$$\mathbf{M}\ddot{\mathbf{x}}_B + \mathbf{C}\dot{\mathbf{x}}_B + \mathbf{K}\mathbf{x}_B = \mathbf{F}(t), \tag{3.24}$$

With $\mathbf{M}, \mathbf{C}, \mathbf{K}, \mathbf{F}$ corresponding to the matrices defined in Section 2.3.

and a state vector corresponding to structural displacement and velocities defined by:

$$\mathbf{x}_B = \begin{bmatrix} \mathbf{x}_B \\ \dot{\mathbf{x}}_B \end{bmatrix}, \quad \dot{\mathbf{x}}_B = \begin{bmatrix} \dot{\mathbf{x}}_B \\ \ddot{\mathbf{x}}_B \end{bmatrix}. \tag{3.25}$$

Then the system can be expressed as

$$\dot{\mathbf{x}}_B = \begin{bmatrix} \mathbf{0} & \mathbf{I} \\ -\mathbf{M}^{-1}\mathbf{K} & -\mathbf{M}^{-1}\mathbf{C} \end{bmatrix} \mathbf{x}_B + \begin{bmatrix} \mathbf{0} \\ \mathbf{M}^{-1} \end{bmatrix} \mathbf{F}(t). \tag{3.26}$$

Next, consider a system ($\mathbf{x_c}$) composed of two *uncoupled subsystems*: the power-hydraulic subsystem ($\mathbf{x}_A$) and the structural subsystem ($\mathbf{x_b}$) .

Utilizing the sub-structuring approach the full system is simply defined by

$$\mathbf{x}_C = \begin{bmatrix} \mathbf{x}_A \\ \mathbf{x}_B \end{bmatrix}. \tag{3.27}$$

With a state-space representation corresponding to

$$\dot{\mathbf{x}}_C = \mathbf{A}_C \mathbf{x}_C + \mathbf{B}_C U(t) + f_{nl}(\mathbf{x}_C), \tag{3.28}$$

$$\frac{d}{dt}\begin{bmatrix} \mathbf{x}_A \\ \mathbf{x}_B \end{bmatrix} = \begin{bmatrix} \mathbf{A}_A & \mathbf{O} \\ \mathbf{O} & \mathbf{A}_B \end{bmatrix}\begin{bmatrix} \mathbf{x}_A \\ \mathbf{x}_B \end{bmatrix} + \begin{bmatrix} \mathbf{B}_A \\ \mathbf{B}_B \end{bmatrix} U(t) + \begin{bmatrix} f_{nl}(\mathbf{x}_A) \\ f_{nl}(\mathbf{x}_B) \end{bmatrix}. \tag{3.29}$$

To couple the hydraulic and structural systems, displacement compatibility is enforced at the interface of the chosen degrees of freedom, piston displacement and top nodal displacement of the beam.

Let the node in the MDOF structure that is coupled to the piston of the hydraulic subsystem be denoted as n_k. As described in Chapter 2, the structure is discretized using N nodes, with each node having two degrees of freedom (translational and rotational, $[u, \phi]$). Consequently, the system dimensions are given by

$$\text{dim}(\mathbf{M}) = 2N \longrightarrow \text{dim}(\mathbf{A}_C) = 4N.$$

$$\text{dim}(\mathbf{M}) = 2N \longrightarrow \text{dim}(\mathbf{A}_C) = 4N.$$

Let us now enforce a rigid coupling, where the displacement and velocity of the piston are set equal to those of node n_k, thisis equivalent to

$$\mathbf{x}_A^0 = \mathbf{x}_B^{2k}, \tag{3.30}$$

$$\mathbf{x}_A^1 = \mathbf{x}_B^{2k+2N}. \tag{3.31}$$

There are several mathematical methods to enforce this dynamic coupling, such as:

1. **Lagrange multiplier method**

   The coupling between DOFs can be generalized as

   $$u_a^* = G u_a, \quad u_b^* = E u_b, \quad g(u_a, u_b) = G^T u_a - E^T u_b = 0, \tag{3.32}$$

   where G and E are selection matrices that pick the appropriate DOFs for coupling. In this approach, Lagrange multipliers λ are introduced to enforce the constraint, resulting in the following coupled system:

   $$\mathbf{M}\ddot{u}_a + \mathbf{C}\dot{u}_a + \mathbf{K}u_a + G^T\lambda = f_a(t), \tag{3.33}$$

   $$\dot{u}_b = f(u_b, U) + E^T\lambda, \tag{3.34}$$

   $$g(u_a, u_b) = G^T u_a - E^T u_b = 0. \tag{3.35}$$

   This method is generalizable to multiple or complex interface constraints, and between domains that may have different dynamics, but it increases the size of the system due to additional unknowns(λ) [66].

2. **Direct substitution**

   Direct substitution enforces the coupling by explicitly replacing the coupled DOFs of one subsystem with those of the other:

   $$u_b^* = (E^T)^{-1} G^T u_a, \quad \dot{u}_b^* = (E^T)^{-1} G^T \dot{u}_a. \tag{3.36}$$

   This eliminates the need for Lagrange multipliers and reduces the system size. It is efficient when the coupling involves only a small number of DOFs or when the inverse of E^T is straightforward to compute. However, for large-scale systems or multiple coupling constraints, bookkeeping can become cumbersome.

In the system being studied, the hydraulic piston is coupled to a single structural node of the MDOF system, with only displacement and velocity constraints at that node. Therefore, direct substitution is a natural and efficient choice for enforcing the coupling.

Another key difference lies in the type of solver required to solve each formulation of the coupled system . The Lagrange multiplier method results in a Differential Algebraic Equation (DAE) system, which requires specialized solvers that can be more cumbersome to implement and tune [67]. In contrast, Direct Substitution converts the system to a standard ODE form, allowing the use of highly optimized and readily available ODE solvers. This further supports the choice of direct substitution for the current study.

Description of Structure

The structural system considered in this study is modeled as a discretized Euler-Bernoulli (EB) beam. The beam is divided into N elements, with each element characterized by uniform material and geometric properties. The parameters defining the properties of the beam are presented in Table 3.3.

Table 3.3: Structural parameters of the Euler-Bernoulli beam

Description	Symbol	Value	Units
Number of nodes in the discretization	N	20	[-]
Material density of structure	ρ_{struct}	7850	kg/m^3
Young's modulus	E	200×10^9	Pa
Cross-sectional area	A	2124×10^{-6}	m^2
Moment of inertia	I	3.492×10^{-6}	m^4
Element length	l	$4/N = 0.2$	m
Boundary conditions at end 1	–	[Fixed, Fixed]	[-,-]
Boundary conditions at end 2	–	[Free, Free]	[-,-]
Prescribed damping ratio	ω_1, f_1	5,1	Hz,%
Prescribed damping ratio	ω_2, f_2	120,1	Hz,%

This properties define a structural system such that exhibits the following mode shapes:

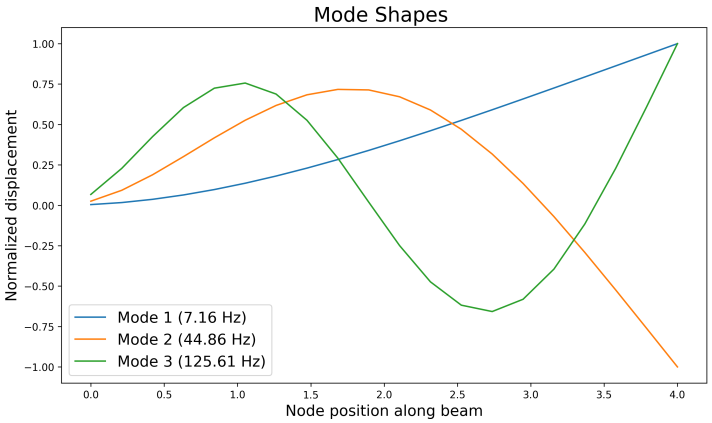

Figure 3.12: Modes shapes of structure

3.3. Close Loop control

A control system is said to operate in a **Closed-Loop** configuration when the control signal is a function of one or more variables of the system, rather than being independent of them. In essence, the simplest possible closed-loop system uses feedback from the response of a target variable and compares it to its desired state, or setpoint. The resulting error between the actual and desired values is then used to compute the control action.

This structure allows the system to automatically adjust its behavior in response to disturbances or changes in operating conditions, thereby improving accuracy and robustness. The basic block representation of a closed-loop control system corresponds to a systems where the target variable is measured and fed back into a system that determines the control signal, as illustrated in Figure 3.13.

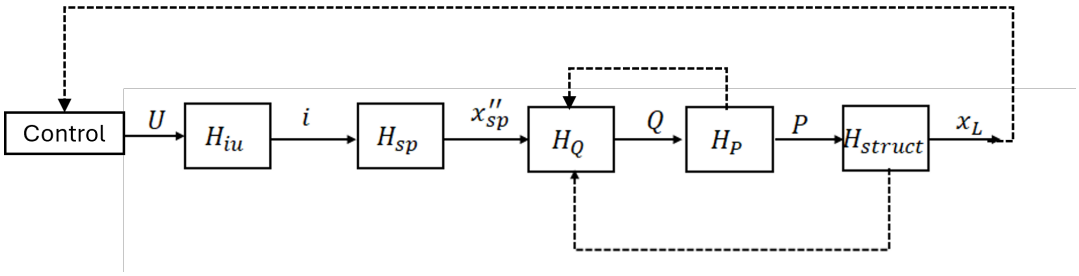

Figure 3.13: Simplified control block diagram

Figure 3.13 illustrates the control scheme in the context of **position control**, where the target variable corresponds to the displacement (or position) of the plant. However, this framework can be modified for **force control**, in which the variable of interest is the acceleration of the mass. More generally, any state variable can serve as the control target. For instance, in some applications, controlling the pressure P may be advantageous, as it would correspond to prescribing a specific force onto the structure.

In the configuration shown, a single feedback loop is employed. Nevertheless, more advanced controllers can incorporate multiple feedback signals, where the primary control variable is supplemented by intermediate state variables to compute the most appropriate control action.

Another important consideration in designing a control scheme is that every variable fed back to the control algorithm must first be measured and transmitted, making it susceptible to measurement noise, transmission noise, and delays. While transmission noise is generally low and negligible compared to other sources of uncertainty in the system, measurement noise can be significant, particularly because it depends on the nature of the measured signal and in the method on which this variable can be measured. For example, displacement and acceleration can usually be measured with high accuracy using LVDTs, optical sensors, or accelerometers, whereas pressure measurements in hydraulic systems are challenging to measure due to pulsations and sensor limitations [68].

In cases where direct measurement is impractical or noisy, state estimation techniques (see Section 2.4.3) can be employed to estimate the state from other easily measurable quantities, such as upstream/downstream pressures, flows, or structural displacements and velocities. This allows the controller to account for nonlinearities and otherwise states that are impractical to measure, enabling effective and flexible feedback control schemes.

3.3.1. Control Scheme

With all the considerations discussed above in mind, a PID-based controller is employed in this work for position control. The block diagram representation of the system and the corresponding control scheme are shown in Figure 3.13.

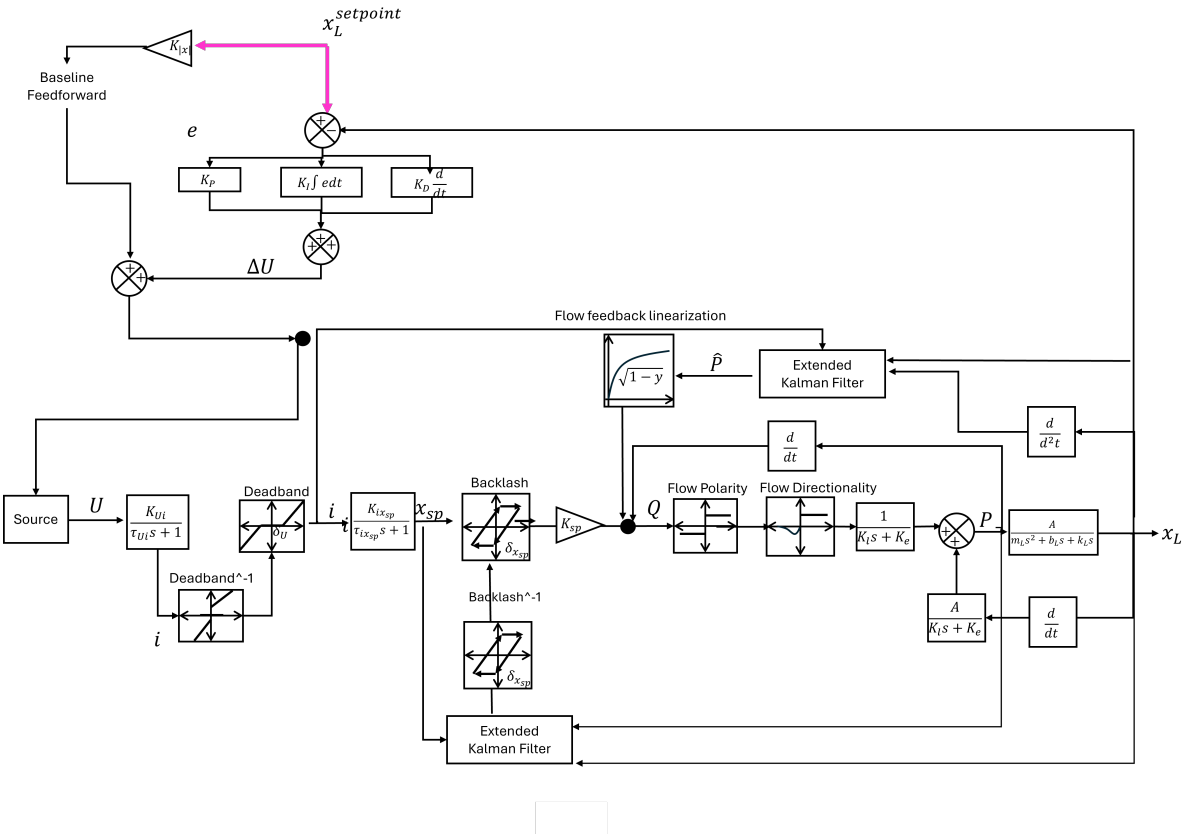

Figure 3.14: System representation

This block diagram represents the complete control scheme. While it may initially appear somewhat complex, it is a more detailed version of the diagram presented in Figure 3.13

In comparison with the open response systems some new subsystems and dynamics have been introduced, specifically

- **Setpoint+PID**
  The PID controller consists of three block corresponding to the P,I and D components as defined in Section 2.4. These components act the difference between the chosen setpoint and the measured displacement
- **Flow Feedback Linearization**
  Given that the nonlinear flow is the main source of nonlinearity in the system, applying an inverse compensator can significantly reduce nonlinear behavior. The compensated flow is defined as:

$$Q = x_{sp} K_q \left(\sqrt{1 - \frac{P}{P_s}} \right) \left(\sqrt{1 - \frac{\hat{P}}{P_s}} \right)^{-1} K_{\text{comp}} \tag{3.37}$$

  where:

  – $\hat{P}$ is the estimated Pressure.
  – K_{comp} is a tuning gain that compensates for modeling errors and measurement uncertainties.

  Expanding the parentheses, this can be rewritten as:

$$Q = x_{sp} K_q K_{comp} \sqrt{\frac{1 - \frac{P}{P_s}}{1 - \frac{\hat{P}}{P_s}}}. \tag{3.38}$$

In the ideal case, where $\hat{P} = P$ and $K_{comp} = 1$, the nonlinear square-root terms cancel out, effectively linearizing the flow-pressure relationship: In practice, $\hat{P}$ is estimated using a EKF from other measured variables, which are subject to both noise and a small delay in the signal. For the excitation frequencies of interest in this study (typically $f < 100$ Hz), the delay associated with measurement, transmission, and processing of the compensator input is negligible, since typical data acquisition rates and sampling frequencies are orders of magnitude higher [69].

With respect to the variables that are measured and used to compute the pressure compensator, they are subject to Gaussian measurement error and uncertainty. Without specifying a particular sensor, it is assumed that the mean $\mu_i = 0$ for an unbiased measurement and the standard is assumed to be $\sigma_i = 1\%$ [70].

- **FeedForward + Saturation**
  The control voltage signal is computed based on the PID action as well as a baseline feedforward voltage. This signal is then subjected to saturation to ensure that its amplitude does not exceed the maximum voltage the system can safely handle. The gain is then defined as a fraction of amplitude of the open loop response.
- **Dead-band compensator**
  Utilizing a pseudo inverse of the dead zone function define in equation (3.21)

$$x'_{sp} \approx DZ(i)^{-1} \left(DZ(i) G_{i x_{sp}} \right)$$

  The dead-band can be pre-compensated, such that its effects are adequately handled.
- **Backlash handling**
  In order to compensate the backlash, a measurement of the actual position of the spool is needed, but, physically this is impractical to achieve. Therefore, a state determination is necessary to be able to inverting the backlash behavior, in particular an EKF is used to determine $\hat{x}''_{sp}$ [61].

  Extended Kalman Filter
  Given that the processes being estimated are nonlinear, the Kalman filter formulation described in Subsection 2.4.3 is not suitable, as it corresponds to linear processes. This can, however, be extended to nonlinear processes by considering the extended version, as described in [71]. The procedure is outlined below.

  Consider the discrete-time nonlinear system:

$$\mathbf{x}_k = f(\mathbf{x}_{k-1}, \mathbf{u}_{k-1}) + \mathbf{w}_{k-1}, \tag{3.39}$$

$$\mathbf{y}_k = h(\mathbf{x}_k) + \mathbf{v}_k \tag{3.40}$$

  where $\mathbf{x}_k$ is the hidden state, $\mathbf{u}_k$ is the control input, and $\mathbf{y}_k$ is the measurement vector. The noise terms $\mathbf{w}_k$ and $\mathbf{v}_k$ are zero-mean Gaussian with covariance matrices $\mathbf{Q}$ and, $\mathbf{R}$ respectively.

  Since $f(\cdot)$ and $h(\cdot)$ are nonlinear, the EKF linearizes these functions at the current estimate $\hat{\mathbf{x}}_{k-1|k-1}$ using Jacobian matrices

$$\mathbf{F}_{k-1} = \left. \frac{\partial f}{\partial \mathbf{x}} \right|_{\hat{\mathbf{x}}_{k-1|k-1}, \mathbf{u}_{k-1}}, \quad \mathbf{H}_k = \left. \frac{\partial h}{\partial \mathbf{x}} \right|_{\hat{\mathbf{x}}_{k|k-1}}.$$

  Then, states can be estimated suing a two-step process:

  Prediction Step:

$$\hat{\mathbf{x}}_{k|k-1} = f(\hat{\mathbf{x}}_{k-1|k-1}, \mathbf{u}_{k-1}), \tag{3.41}$$

$$\mathbf{P}_{k|k-1} = \mathbf{F}_{k-1} \mathbf{P}_{k-1|k-1} \mathbf{F}_{k-1}^{\top} + \mathbf{Q}. \tag{3.42}$$

Update Step:

$$\mathbf{K}_k = \mathbf{P}_{k|k-1}\mathbf{H}_k^\top \left(\mathbf{H}_k\mathbf{P}_{k|k-1}\mathbf{H}_k^\top + \mathbf{R}\right)^{-1}, \tag{3.43}$$

$$\hat{\mathbf{x}}_{k|k} = \hat{\mathbf{x}}_{k|k-1} + \mathbf{K}_k \left(\mathbf{y}_k - h(\hat{\mathbf{x}}_{k|k-1})\right), \tag{3.44}$$

$$\mathbf{P}_{k|k} = (\mathbf{I} - \mathbf{K}_k\mathbf{H}_k)\mathbf{P}_{k|k-1}. \tag{3.45}$$

By linearizing the nonlinear dynamics and measurements at each time step, the Extended Kalman Filter (EKF) recursively estimates the hidden state, $\mathbf{x}_k$, minimizing the estimation error covariance.

Once the state has been determined, it can be used to design an inverse compensator to counteract effects such as dead-band and nonlinear flow

4

Results

Now that the model has been fully defined and the key features of the system response identified, we proceed to a detailed analysis of the results, focusing on the relevant response characteristics and their significance.

4.1. SDOF

Lets first analyze the full nonlinear power hydraulic systems coupled to a single degree of freedom structural system.

4.1.1. Open Loop

Lets re-consider the 2D-FRF, this surface plot has on the x-axis the voltage input frequency, and in the y-axis the FFT of the response.

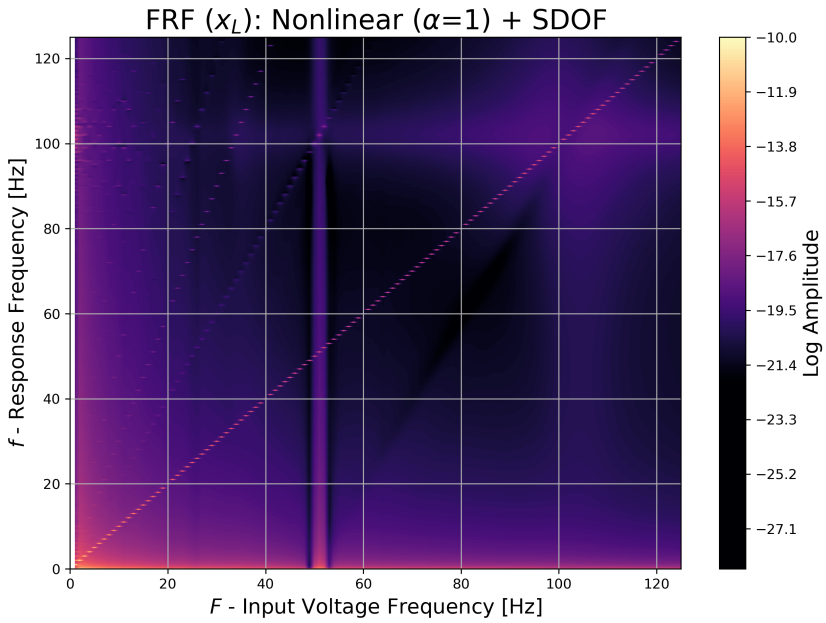

(a) SDOF displacement x_L

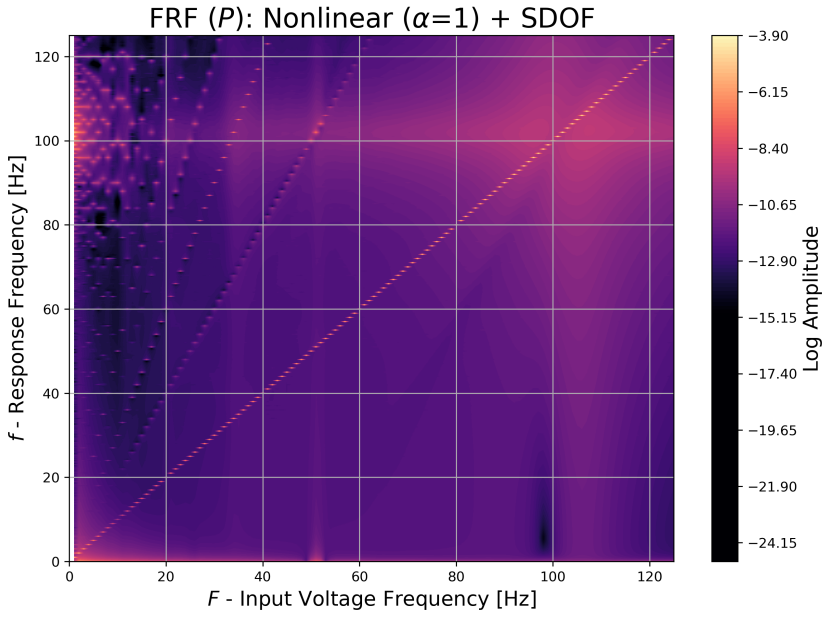

(b) Pressure P

Figure 4.1: 2D Frequency Response Functions (FRF) for $\alpha = 1$.

As expected from a nonlinear system, given a single-harmonic input, a multi-harmonic response is observed, in particular, the following phenomena can be observed

1. **Response at forcing frequency**
   The system, similar to the linear model, response at the forcing frequency, this can be seen by the response at curve defined by

   $$f = F$$

   Which correspond to the diagonal line with and angle of $45°$.
2. **Response at forcing super-harmonics**
   The system (less noticeable for the displacement response) responds at super-harmonics of the

input signal, this is represented by the curves corresponding to the lines with a slope different than 1, more specifically

$$f = n \cdot F \qquad n \in \mathbb{Z}$$

As evident from the figure the response does not present more than $n = 4$ super-harmonics.

3. **Response at oil-column frequency**
   Similar to the linear case, the system strongly responds when excited at the oil-column frequency, this is represented increase of response intensity around the oil-column resonant frequency.

$$f = f_{\text{oil}} = 101.5\text{Hz}$$

4. **Response at half the oil frequency**
   Additionally, at sub-harmonics of the oil-column frequency, where system strongly responds.

Lower Supply Pressure

Now consider the same analysis for lower values of α, which parametrizes the effects of nonlinear flow, as mentioned in expression (3.23).

In this context, the parameter α represents a normalized operating pressure. When $\alpha = 1$, the system operates at its maximum supply pressure, corresponding to the minimum nonlinear behavior. In contrast, $\alpha = 0$ represents a system with no supply pressure.

By progressively reducing α, the supply pressure is lowered, which decreases power consumption but increases the relative influence of nonlinear effects. Therefore, analyzing the system at different α values provides a useful way to study the transition between near-linear and highly nonlinear regimes.

First, consider the FRF of the piston displacement(x_L), as shown in Figure 4.2

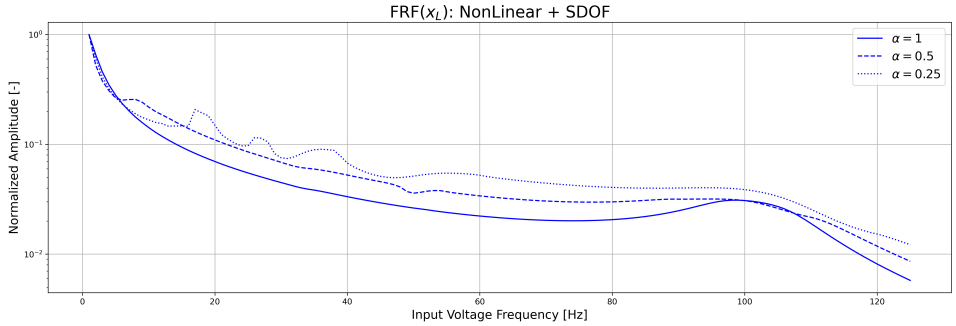

(a) |FRF(x_L)|

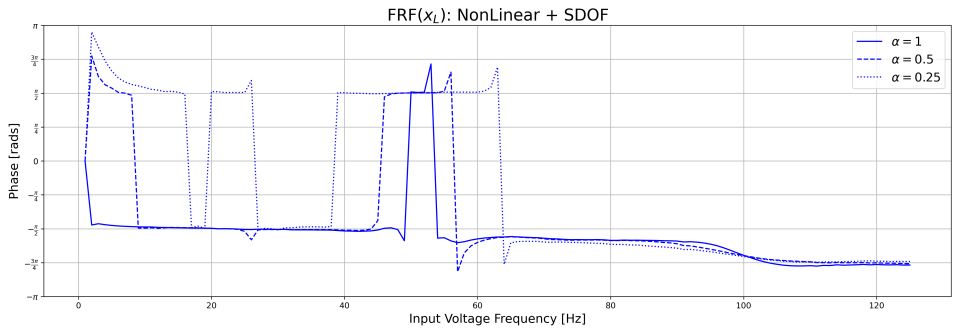

(b) Phase FRF(x_L)

Figure 4.2: Comparison of FRF(x_L) for different values of α

Contrary to the 2D FRF, the super-harmonics of the input signal cannot be directly inferred from the plot, however oil column sub-harmonics are indirectly evident, even though the magnitude of these peaks is minor.

On the other hand, the effects of the oil-column resonance are discernible in the phase response.

The analysis is similar for the velocity response. However, it is important to explicitly examine the velocity behavior, as the coupling between the structural and hydraulic subsystems occurs through velocity feedback. Specifically, the piston velocity directly influences the chamber pressure, as described by the state-space formulation (see Equation 3.1.3). Therefore, understanding the velocity response is critical for interpreting the system's overall dynamics.

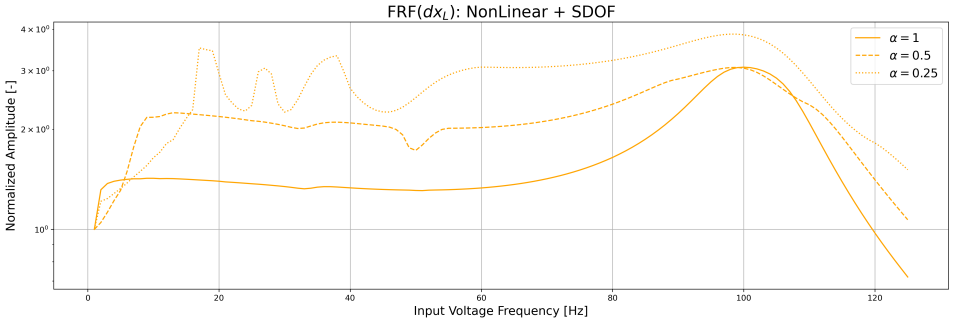

(a) |FRF(dx_L)|

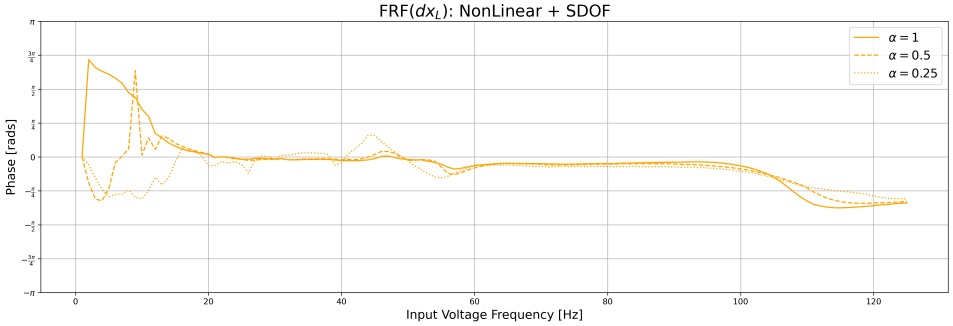

(b) Phase FRF(dx_L)

Figure 4.3: Comparison of FRF(dx_L) for different values of α

As expected, the nonlinear effects are more pronounced in the velocity response.

Finally, with respect to the pressure response

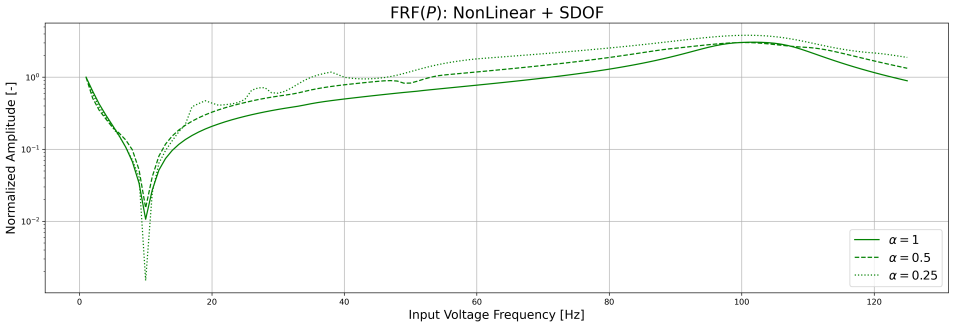

(a) $|P|$

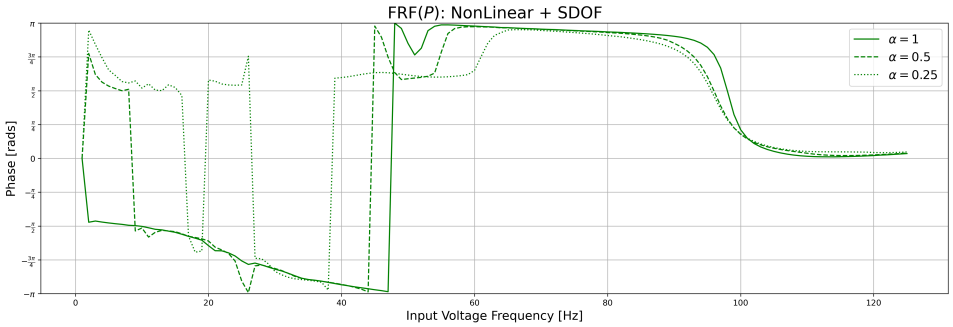

(b) Phase(P)

Figure 4.4: Comparison of FRF(P) for different values of α

The dynamics are similar to the velocity response, it is noteworthy to mention that the anti-resonance peak due to the resonance of the SDOF is still prominent over all other frequencies.

2D FRF comparison at different α

Whereas the FRF gives a general description of the dynamics, it was previously shown that it still obfuscates a lot of information, which is not the case in the FRF surface plot, therefore the plot showing the response of the system across all frequencies for all input frequencies is shown in the following figure

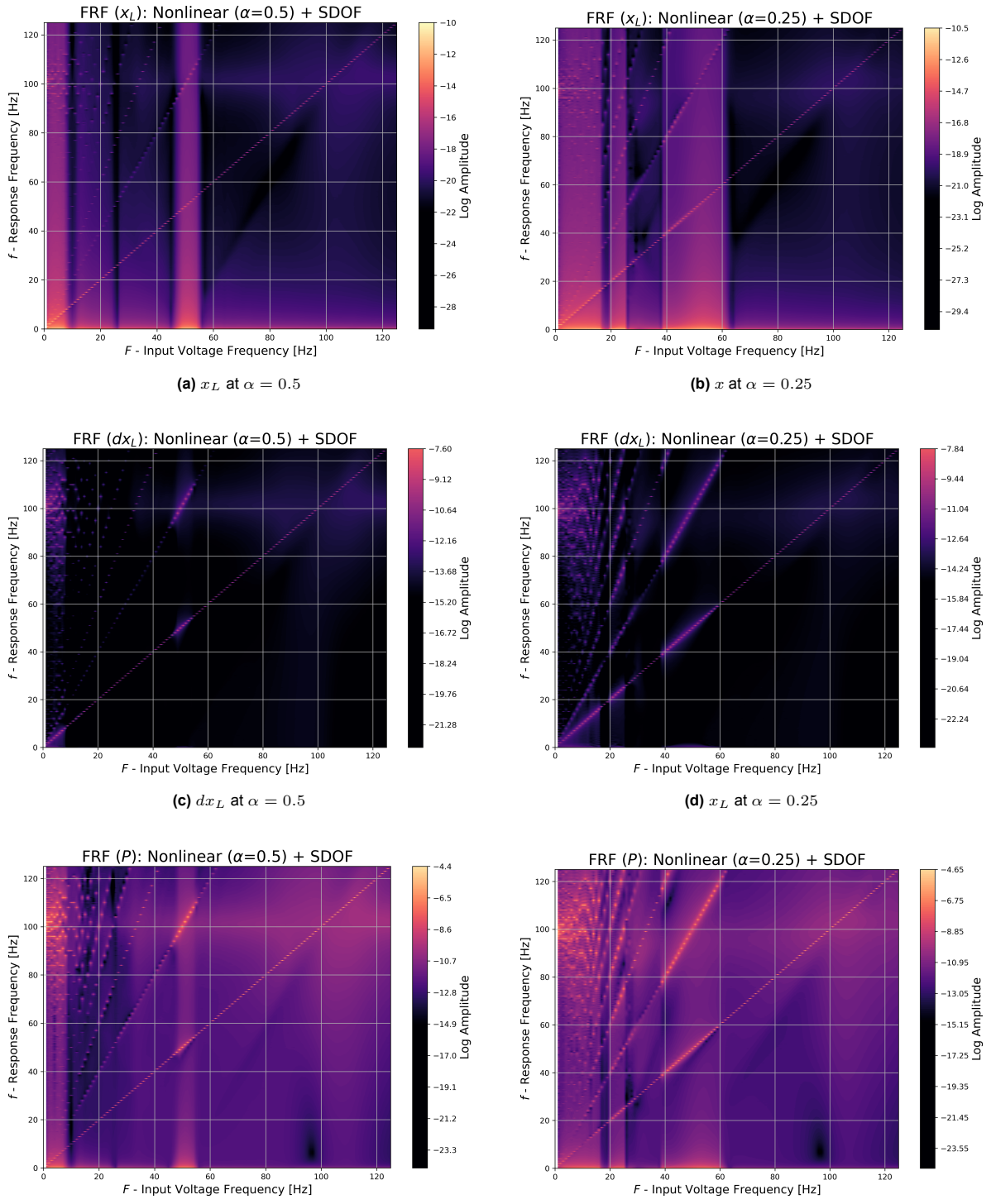

(a) x_L at $\alpha = 0.5$

(b) x at $\alpha = 0.25$

(c) dx_L at $\alpha = 0.5$

(d) x_L at $\alpha = 0.25$

(e) P at $\alpha = 0.5$

(f) P at $\alpha = 0.25$

Figure 4.5: 2D FRF plots for different α values: left column for $\alpha = 0.5$, right column for $\alpha = 0.25$

Figure 4.5 demonstrates that the nonlinear response intensifies as the supply pressure is reduced. Notably, at certain excitation frequencies, the amplitude of super-harmonics approaches that of the fundamental harmonic, meaning that the response is highly nonlinear.

The response is similar to the case of $\alpha = 1$, but a few patterns start to merge, particularly related to the vertical bands where the response is distinct from the rest.

Interested Bandwidths

Based on the 2D FRF, four relevant bandwidths can be determined for the system:

1. **Low Range Frequencies Band** ($F = 10$Hz)
   At low frequencies, the response is erratic, mainly due to effects related to the nonlinear behavior of the spool, such as backlash, which propagate and cause a nonlinear response in both position and pressure.

   Lets consider the time response, for both variables:

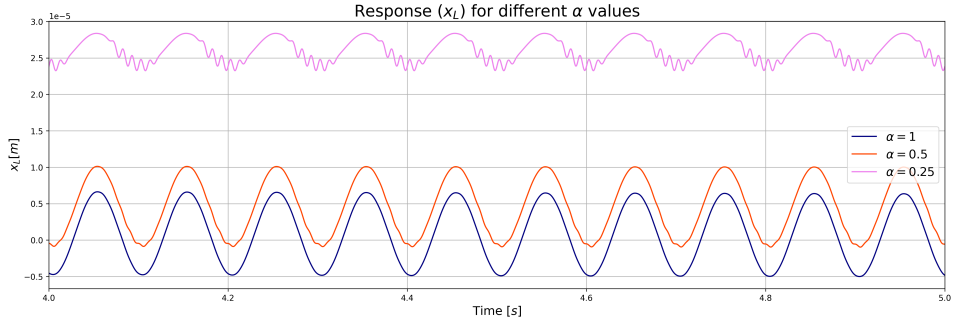

(a) x_L

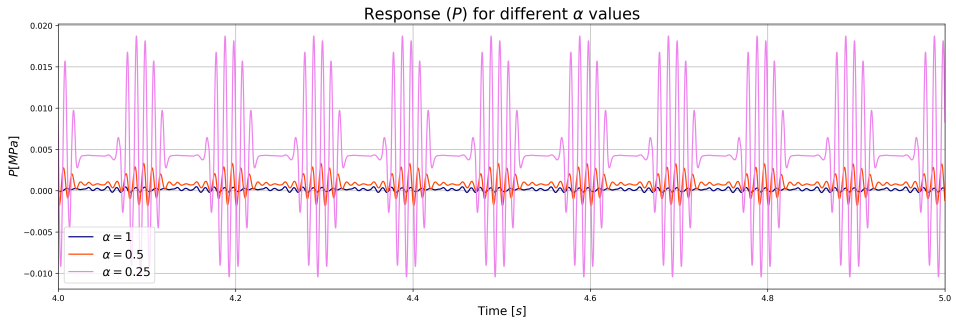

(b) P

Figure 4.6: Time response for varying α values at $F = 10$Hz

From the time-domain response, it is evident that the primary nonlinear behavior manifests in the pressure signal. To investigate this further, the frequency content is analyzed using the FFT, as shown in Figure 4.7.

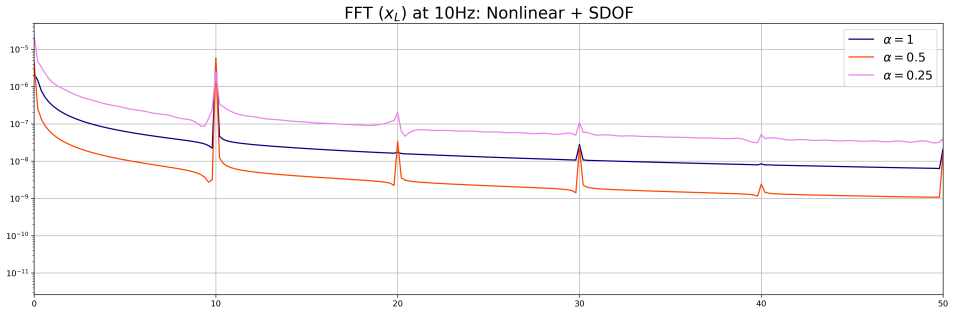

(a) x_L

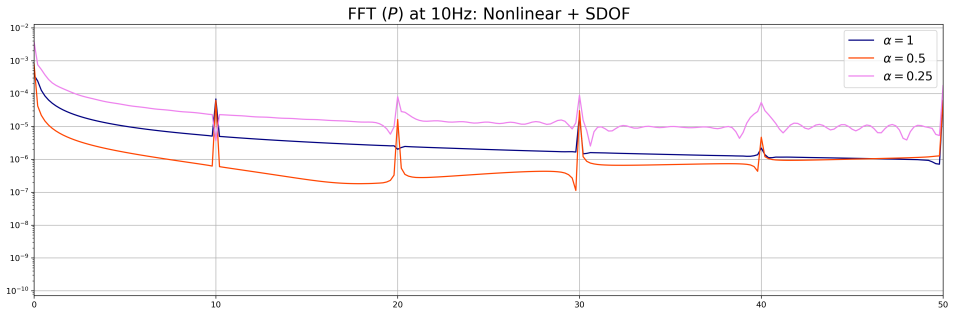

(b) P

Figure 4.7: Frequency response for varying α values

Given that the flow is main source of nonlinear behavior it is useful to plot the *Valve-Flow Characteristics*, as it was defined and explained in Section 3.1.2

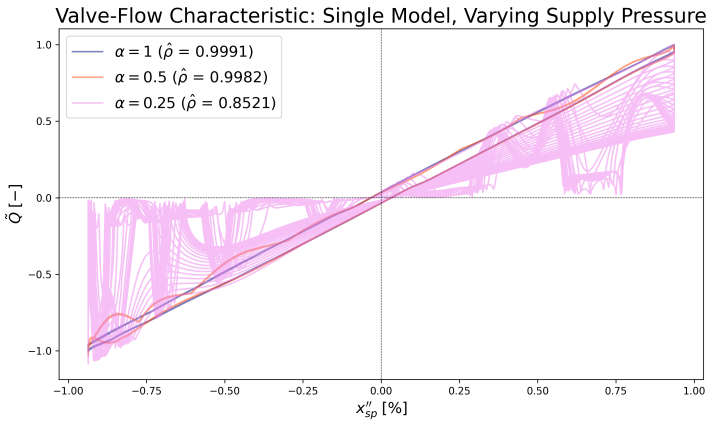

Figure 4.8: Flow characteristic for different values of α at $F = 10$Hz

The limitations of using the Pearson Correlation as a metric are evident in Figure 4.8. It can be seen that for a strong nonlinear response it is not a good metric, as it does not capture the hysteresis behavior of the flow. Nor does it capture the pressure transient that cause a near flow reversal.

Additionally, the difference in the metric for different α values alone is insufficient to quantify the nonlinearity, as the time and frequency responses clearly show a significant difference in the magnitude of the nonlinear behavior for $\alpha = 0.5$ and $\alpha = 0.25$, which is not readily apparent from the coefficient itself.

2. **Mid-range Frequencies Band**
   In the bandwidth defined around the frequency range of $F = 35$Hz, the manifestation of this non-

linear behavior is system-dependent. In our particular case, it corresponds to a range below the first oil-column subharmonic . Within this band, the response is primarily governed by nonlinear pressure signal, and a weakly nonlinear displacement response. .

Similarly as before, the time response is presented:

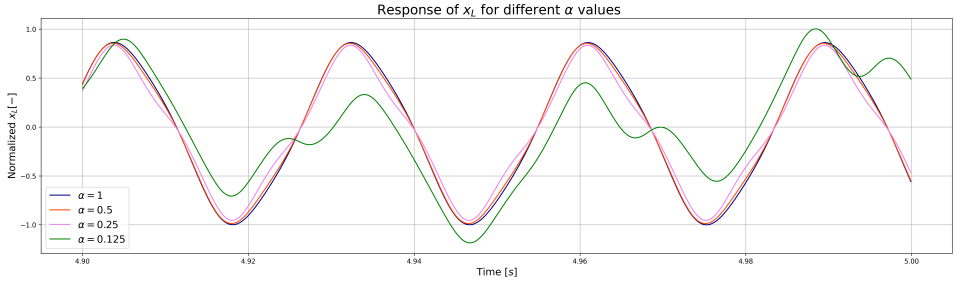

(a) x_L

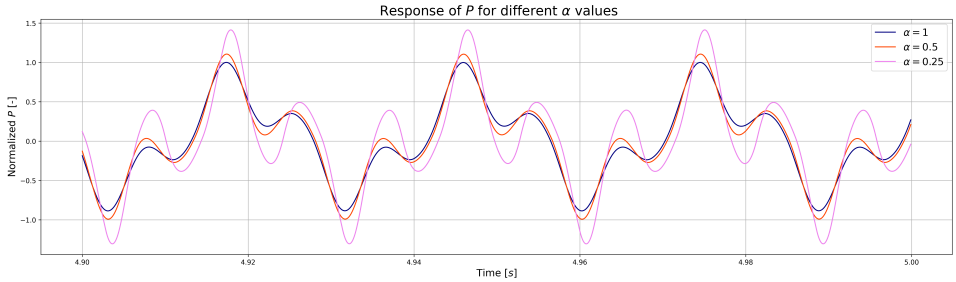

(b) P

Figure 4.9: Time response for varying α value at $F = 35$Hz

The FT for the response shown above is:

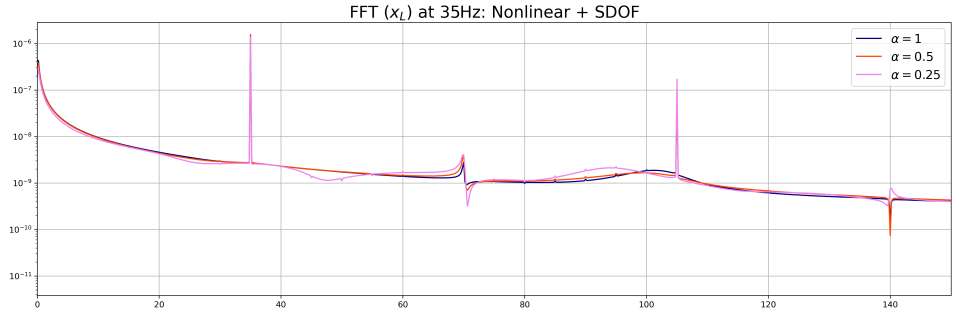

(a) x_L

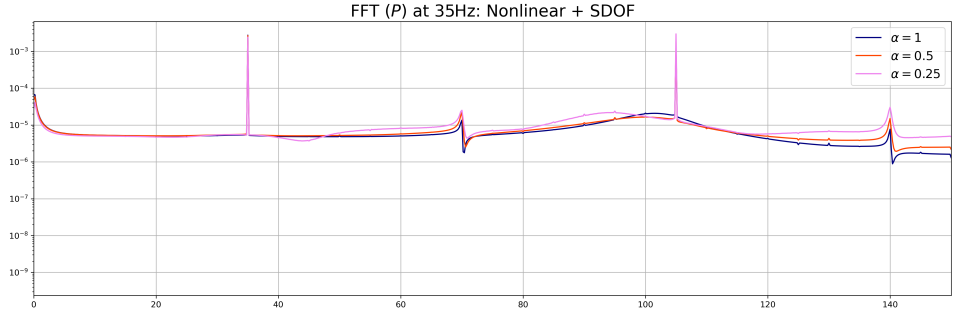

(b) P

Figure 4.10: Frequency response for varying α values

Figure 4.10 clearly shoes the effect of the oil-column resonance, which interacts with the third super-harmonic of the input. This interaction amplifies the third super-harmonics of the forcing such that the pressure response is greater than the response at the input frequency. This phenomena although important does not directly affect the displacement response, but it does it indirectly as the displacement is a function of the pressure.

Finally the flow characteristics,

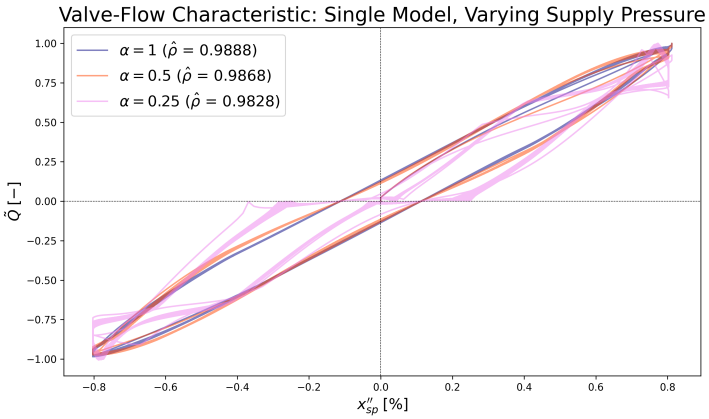

Figure 4.11: Flow characteristic for different values of α at F =35Hz

Figure 4.11 shows that, although the overall response is nonlinear, the flow signal predominantly responds at the same frequency as the valve opening, with only a slight phase lag. This behavior is desirable, as the valve opening is essentially the directly controllable input.

3. **Oil-Column Sub-harmonic Band**
   At the frequency band around half the oil column's natural frequency ($\approx 50Hz$), the system exhibits highly nonlinear behavior, as evidenced by the high-intensity band observed in Figure 4.5. This band becomes progressively wider as the pressure is reduced and the nonlinear content becomes more dominant, as evident from the time response shown in Figure 4.5

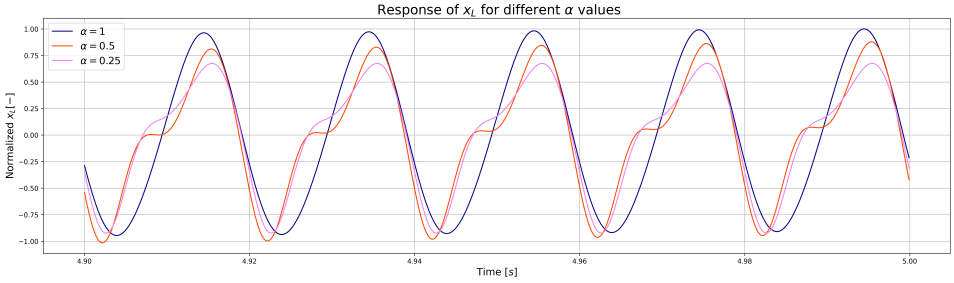

(a) x_L

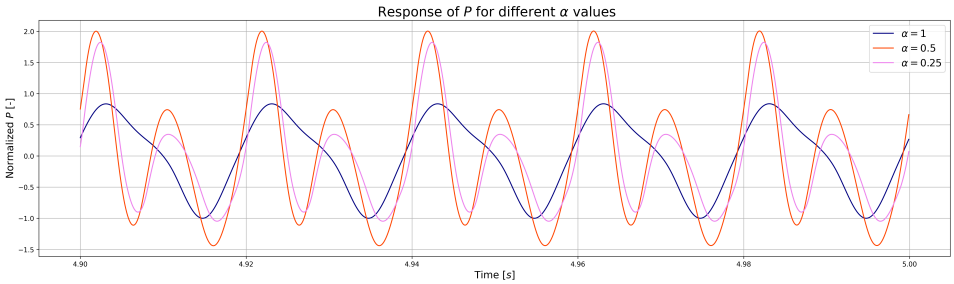

(b) P

Figure 4.12: Frequency response for varying α values

Not only does the pressure response exhibit multiple harmonics, but these harmonics are also out of phase with one another, which contributes to a stronger nonlinear displacement response.

The manifestation of this highly nonlinear behavior at half the oil column's natural frequency can be explained by the amplification of superharmonics. Although such components are present in other frequency bands, they usually have much lower amplitudes than the fundamental harmonic. At this specific band, however, they are amplified by the oil-column effect, which primarily affects the velocity and pressure responses. The effect can be observed in Figure 4.13, where the amplification due to oil column resonance is evident.

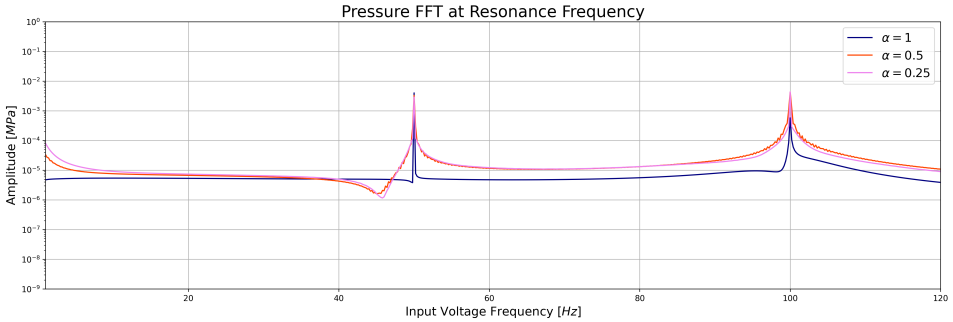

Figure 4.13: Pressure FT at 50Hz

4. **High Range Frequency Band**
This band corresponds to the frequency range between the first subharmonic and the main harmonic of the oil column. At these frequencies, the response amplitude naturally decrease, which leads to a weaker nonlinear response due to the amplitude-dependent nature of the nonlinearity. Additionally, the frequency content of the input does not significantly interact with the oil-column resonance, further limiting the amplification of nonlinear effects.

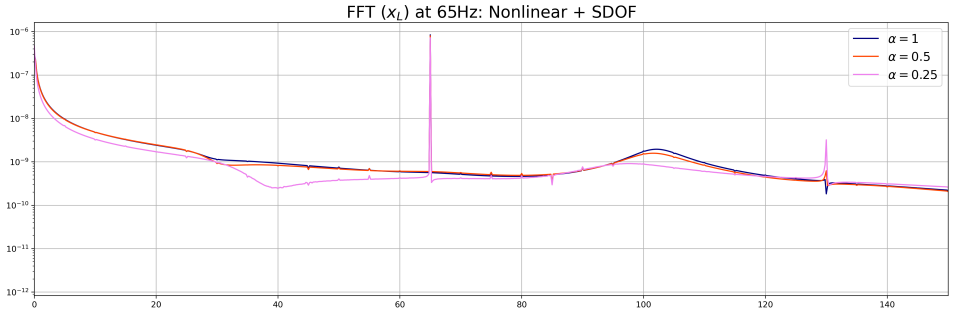

(a) x_L

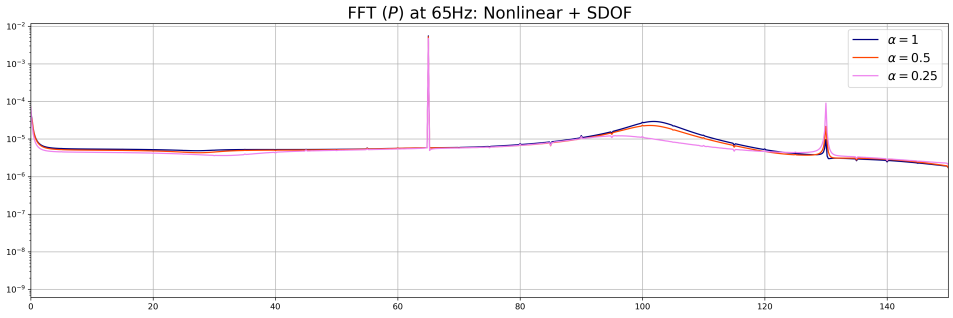

(b) P

Figure 4.14: Frequency response for varying α values

This can also be seen in the flow characteristics, with an almost elliptical response curve.

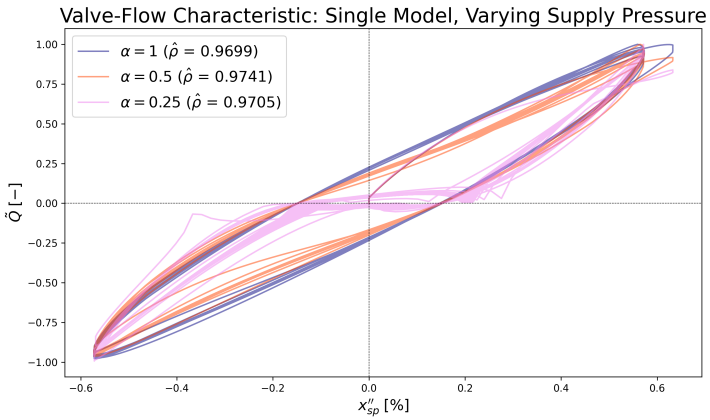

Figure 4.15: Flow characteristic for different values of α at $\Omega = 65Hz$

Total Harmonic Distortion

Evidently, the figures presented in the previous subsection demonstrates that the metric used to characterize the response becomes inadequate when the system diverges from the linear regime. This highlights the need for a more effective metric that characterizes the strength of the nonlinear response.

While the full 2D FRF plots contains all the relevant information, their complexity makes it difficult to convey the main effects clearly and concisely.

Therefore, a new metric is needed. To this end, the Total Harmonic Distortion (THD) is introduced and defined as:

$$\mathrm{THD} = \frac{\sqrt{\sum_{n=2}^{N} |X_n|^2}}{|X_1|}$$

where:

- X_1 is the amplitude of the fundamental harmonic,
- X_i for $i \geq 2$ are the amplitudes of the higher-order harmonics.

The THD serves as a frequency-domain metric that quantifies the relative energy content of the harmonics beyond the fundamental. This facilitates the comparison and estimation of nonlinear behavior across varying excitation frequencies and supplied pressure(αP_{max}).

This metric is particularly appropriate, as it allows us to quantify the nonlinear content of different variables and models within a single plot. Accordingly, Figure 4.18 presents the THD values for the main state variables under varying supplied pressures. It is important to note that a value of $n = 3$ was chosen for the computation of THD. This choice is supported by the previous FT plots, which show that superharmonic content beyond the third harmonic is mostly negligible.

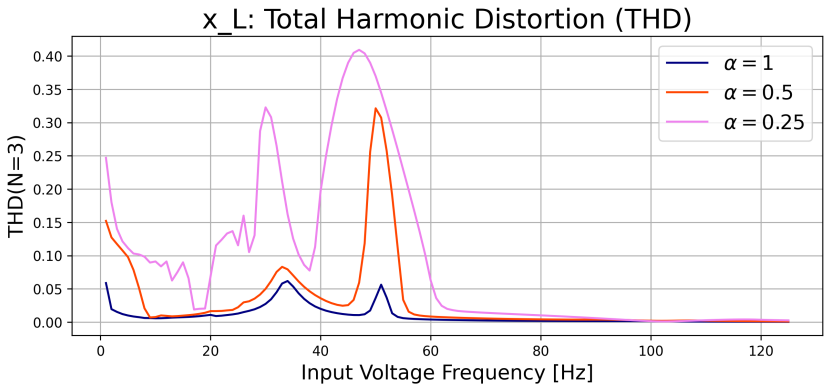

(a) THD(x_L)

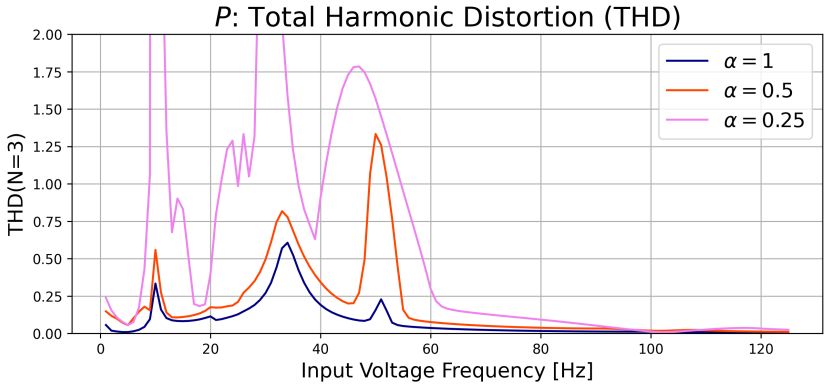

(b) THD(P)

Figure 4.16: Total Harmonic Response as a function of excitation frequency for different value of α

Figure 4.18 confirms the earlier analysis and highlights the key frequency bands of interest. Additionally, it clearly shows how these bands are affected and tend to shift or widen as the supplied pressure decreases. Although THD is a valuable metric, it remains a frequency-domain measure and does not account for phase information which is an important factor, as previously discussed, especially in the context of phase misalignment between superharmonics.

This limitation is particularly relevant given that the control scheme to be implemented operates in the time domain and aims to minimize residual errors, which does not necessarily correspond to a reduction in THD. Therefore, THD should be interpreted in conjunction with the 2D FRF plots and time-domain responses to fully capture the system's nonlinear behavior and control-relevant characteristics.

4.1.2. Control of SDOF System

Given the analysis for the nonlinear systems, two possible strategies arise in order to achieve a sinusoidal displacement response.

- **Alter Oil Column resonance**
  By altering the frequency band affected by this phenomenon, we can avoid amplifying unwanted frequencies. However, the oil-column frequency is determined by the compressibility of the hydraulic oil and the actuator properties, and therefore cannot be easily altered without significantly changing the system configuration.

  However, it is important to mention (as discussed in Subsection 2.2.4) that the hydraulic oil properties are thermally dependent and could slightly change during operation. A similar situation can occur with gases getting trapped in the line during operation. These effects are generally minor, and their influence on the value at which the oil frequency manifests is also minimal, so they are not of concern as long as the system is maintained accordingly.
- **Minimize nonlinear Flow**

As previously determined and discussed, the nonlinear flow is the main source of nonlinear behavior, which can be partially counteracted by feedback linearization. Additionally, if the reduction can be accomplished, the knock effect ensures that the superharmonics related to this behavior can no longer be amplified by oil-column subharmonics, thereby reducing the overall nonlinear behavior across the entire range, and especially in the critical band associated with the subharmonic behavior.

To this end, and considering the control system defined in Section 3.3.1, which is implemented for the SDOF system. Given that the dynamics of the system are frequency and amplitude-dependent, the effectiveness of the control is presented at frequencies corresponding to the previously defined representative bands, using a value of $\alpha = 0.25$, which corresponds to the minimum supply pressure and the highest nonlinear behavior considered.

As is common with PID-based controllers, because they are non-model based, the tuning is usually heuristic, as it was done in this case using the traditional tuning guidelines, in order to replicate the tuning practices utilized in industry [72].

To evaluate the performance of the control strategy, the **Integral of Absolute Error**(IAE) will be used. Mathematically, the IAE is defined as:

$$IAE = \int_{t_1}^{t_2} |y(t) - y(t)_{\text{setpoint}}| \, dt \tag{4.1}$$

Conceptually, it is defined as the integral of the residuals over a interval, in particularly the interval corresponds to N-times the period of the setpoint signal, with N=10 for the purposes of this work.

Performance of Displacement Control

The results for the displacement control at frequencies within the previously identified band are presented, considering $\alpha = 0.25$, which results in a significantly nonlinear response. In this analysis, the setpoint amplitude corresponds to the amplitudes of the open-loop response at $\alpha = 1$, allowing for the evaluation of the control system's performance in terms of the percentage of the original amplitude that can be achieved under the nonlinear response when utilizing only 25% of the maximum supply pressure (P_{max}).

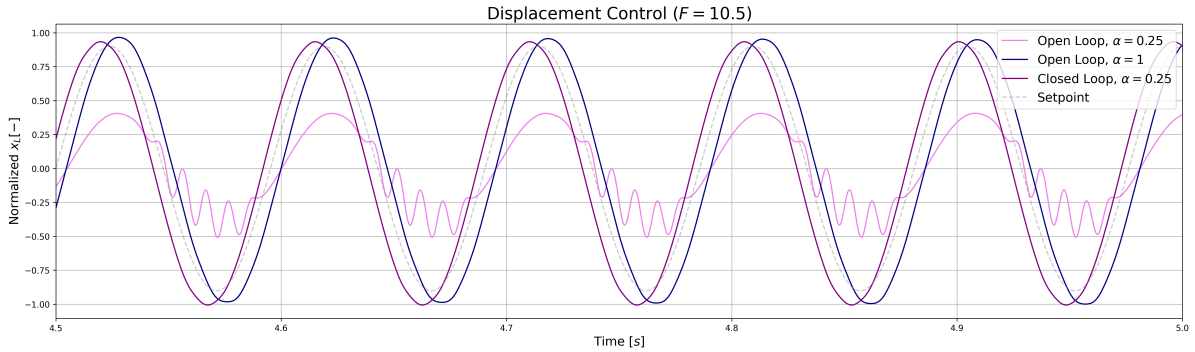

(a) Time Response

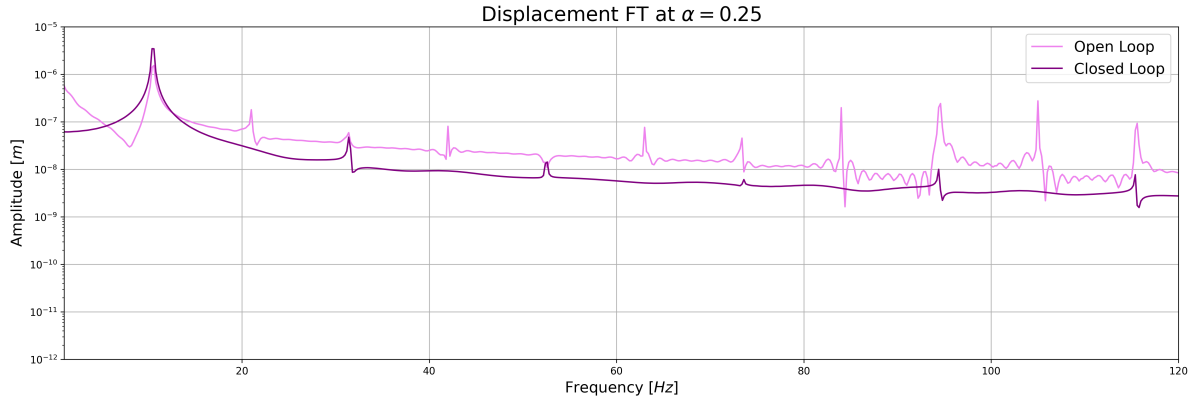

(b) Frequency Contents

Figure 4.17: Displacement control of SDOF at 10.5 Hz and $\alpha = 0.25$

Figure 4.17 shows that the signal is considerably less nonlinear. Specifically, a sinusoidal signal with the amplitude corresponding to the open loop at $\alpha = 1$ can be achieved using only 25% of the supply pressure. However, there is a non-negligible phase delay between the controlled signal and the setpoint. Although phase delay is important in some control scenarios, for the purpose of driving using GDP technology, the frequency content of the signal is of primary importance.

The lag delay is accounted for in the IAE, as it is a time-based metric; therefore, it is accompanied by the THD, which, as previously mentioned, does not account for phase delay.

The other frequency band with substantial nonlinear response corresponds to the one around the first oil-column subharmonic, around 50 Hz. Implementing and tuning the control system for this particular input yields the following results:

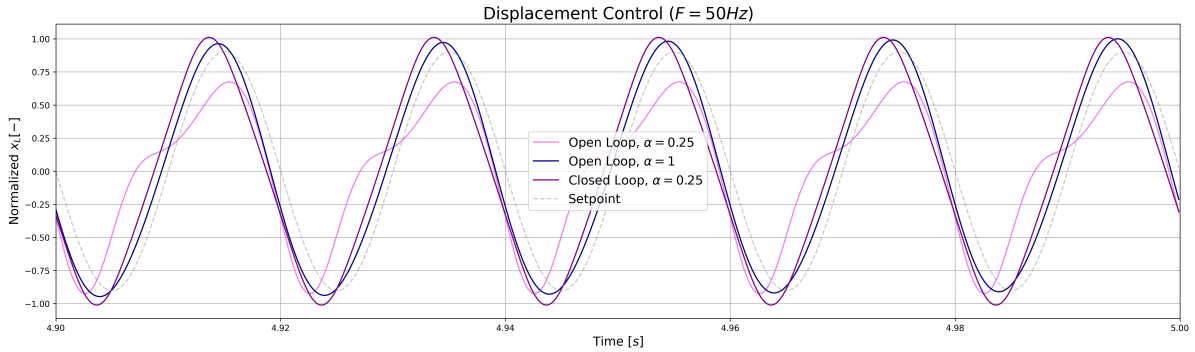

(a) Time Response

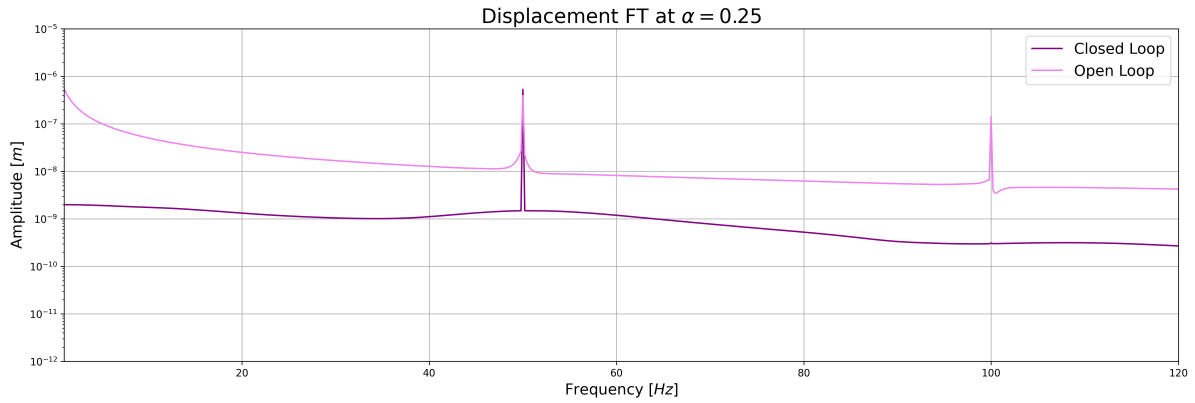

(b) Frequency Contents

Figure 4.18: Displacement control of SDOF at 50Hz and $\alpha = 0.25$

Table 4.1: Displacement control metrics for SDOF at critical bands $\alpha = 0.25$

Input Frequency[Hz]	IAE_{open}	IAE_{close}	IAE Change (%)	THD_{open}	THD_{close}	THD_{change}
10.5	0.17	0.08	-48	0.015	0.017	48.5
50	0.14	0.11	-19	0.36	0.0021	-99.4

Although the result presented in Table 4.1 are useful to characterize the performance of the control, the metrics need to be interpreted carefully. For example, at lower frequencies, since the main nonlinear component is associated with spool nonlinearity and not flow, the high-frequency content is not present in the super-harmonics of the forcing. Therefore, its reduction is not reflected in the THD. Consequently, neither the time metrics nor the frequency metrics fully capture the system's behavior. This is why examining the both time and Fourier Transform (FT) of the response is encourage.

4.2. MDOF

Considering the coupling defined between the structural subsystem and power hydraulic subsystem, as defined in 3.2.1, corresponding to the piston of the actuator rigidly coupled to the top of a cantilever EB beam.

Depending on the system properties, three distinct behaviors can be observed. Among all possible parameters, two primarily determine which scenario the system will apply.

1. **Structural Damping**
   The structural damping encompasses both internal damping mechanisms, in particular, Rayleigh damping, and other dissipative forces acting on the structure, such as soil friction. The amount of damping determines whether the internal dynamics of the structure will feed back into the hydraulic actuator through the rigid coupling and influence the global dynamics of the system.

2. **Mass ratio**
   The ratio between the inertia of the structure and that of the piston plays an important role in determining the extent to which the structural dynamics influence the behavior of the power-hydraulic system.

   Given that the structure is linear, it is convenient to express the ratio in terms of the modal mass. Considering the mode shapes and the location at which the actuator is coupled, it is natural to define the mass ratio as:

$$\mu_m = \frac{m}{\phi_1 \mathbf{M} \phi_1^T}$$

   with ϕ_1 the first mode shape

Possible Dynamics Response Scenarios
The scenario or cases that the system can fall under, depending on the system configuration are

- **Scenario 1**: Strong Power Hydraulic - Weak Structure

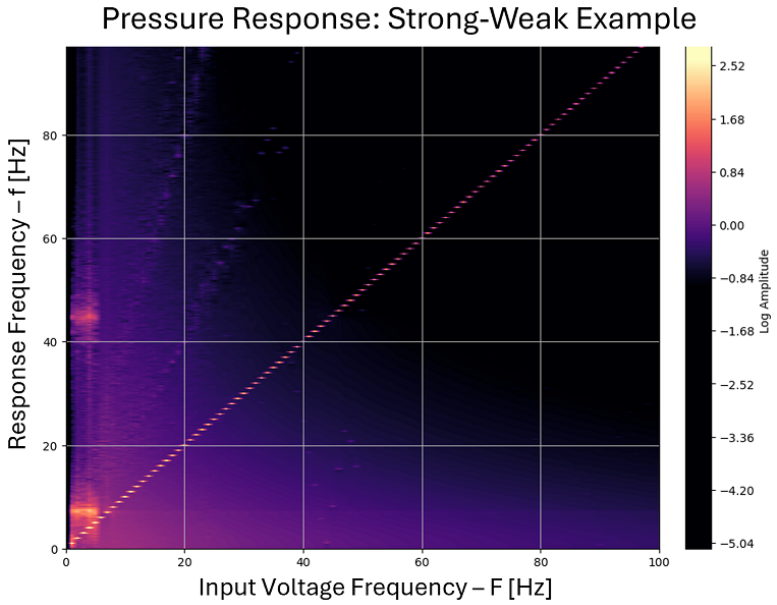

Figure 4.19: 2D FRF of 'Strong-Weak' scenario

   In this scenario, the power hydraulic system is considerably stronger than the structure, such that the structure does not impart significant feedback into the power hydraulic system. As a result, the pressure signal is primarily determined by the input voltage.

   Besides the main response at the input frequency, represented by the diagonal line, small amplitude super-harmonics can be observed as sloped lines with an angle different than 45°. Some interaction between structure-actuator can be observed, particularly in the response at lower frequencies, around the first natural frequency of the structure (f_n^1 = 7.16 Hz). However, the response is still predominantly dominated by the input voltage.

   This case corresponds to the majority of setups used in civil engineering, where the systems are typically designed to avoid coupling. Therefore, it is not of particular interest to this body of work, as the objective is to study the coupling between the power hydraulic and structural subsystems.

- **Scenario 2**: Strong Power Hydraulic - Strong Structure
  Alternatively, this configuration, will also be referred to as *Equal*, it represents a system where there is clear interaction between the subsystems, such that features from both subsystem can be observed in the overall response.

In particular, Figure 4.20 shows that the system responds at the forcing frequency (input voltage frequency), and that the system imparts feedback onto the actuator, manifesting as a response at the first two natural frequencies of the structure (represented by horizontal lines at 7.16 Hz and 44.8 Hz).

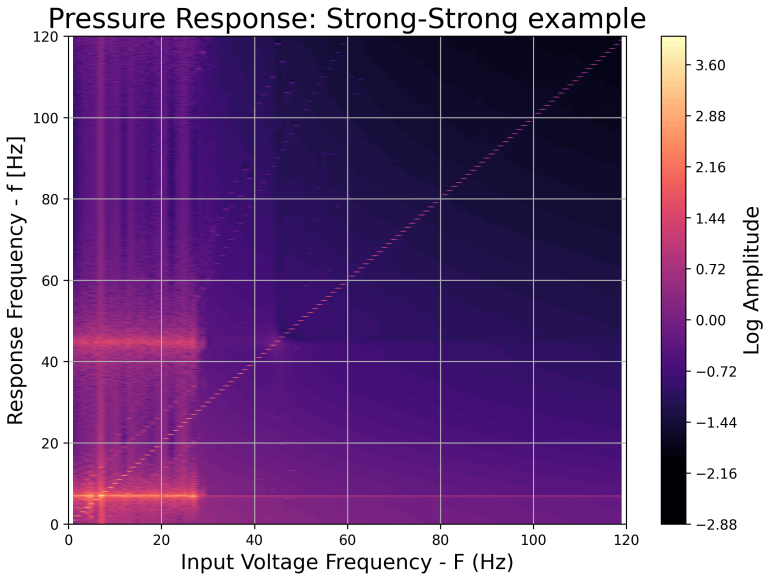

Figure 4.20: 2D FRF of 'Strong-Strong' scenario

- **Scenario 3**: Weak Power Hydraulic - Strong Structure
  The configuration denominated as *Weak-Strong* refers to a setup where the power-hydraulic system is considerably weaker than the flexible structure. Under these conditions, and considering the coupling between both systems, the structure responds at its first natural frequency, which in turn forces the power-hydraulic system to do the same, despite the input signal being different. This synchronization between the two systems must be avoided, as it makes the system uncontrollable.

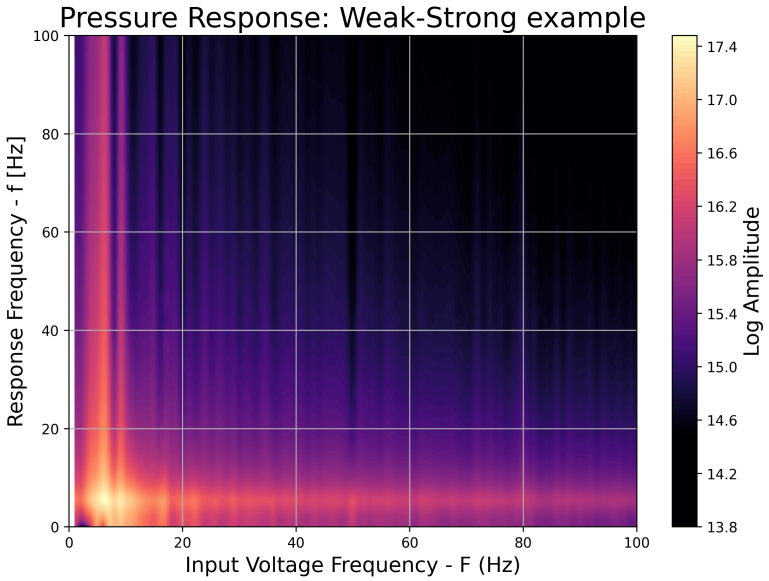

Figure 4.21: 2D FRF of 'Weak-Strong' scenario

4.2.1. Transitioning between cases

Given that Scenario 3 must be avoided, and that Scenario 1 corresponds to an oversized system, it is important to understand how to alter system properties in order to transition between the scenarios outlined above.

Effects of mass ratio

An increase in the mass ratio contributes to a transition from Scenario 3 to Scenario 2. For example , lets consider the system under a input voltage frequency of 20Hz, as illustrated in Figure 4.22.

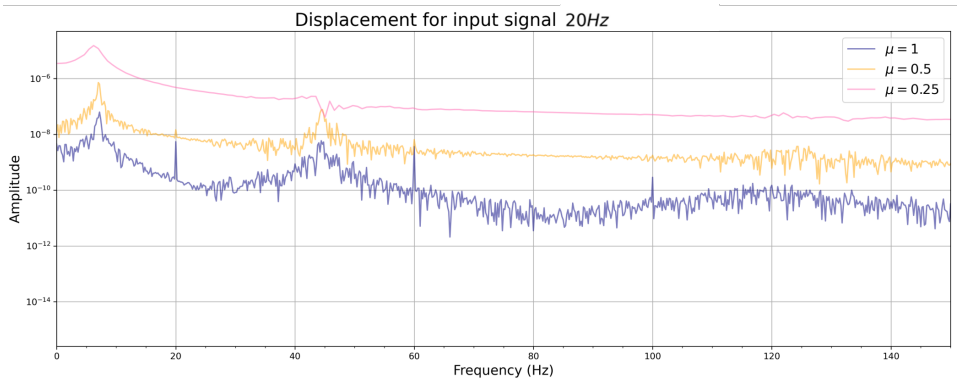

(a) Frequency content of coupled degree of freedom

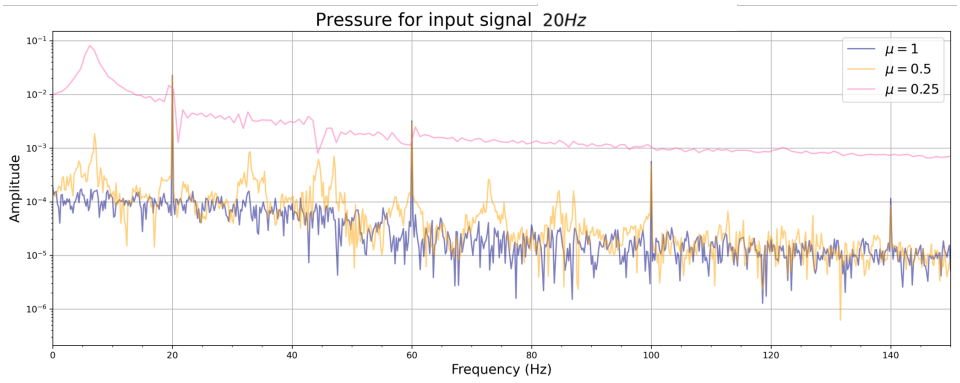

(b) Frequency Contents of pressure response

Figure 4.22: Effect of mass ratio (μ) in dynamic regime

It is evident, particularly in Figure 4.22a, that at low mass ratios, the dynamics of the structural subsystem dominate the overall response. As the mass ratio increases, the influence of the hydraulic system becomes more significant, such that the displacement response of the piston (and the top node of the structure, due to rigid coupling) reflects both the forcing frequency and the first two natural modes of the structure. This indicates a transition from the *Weak-Strong* scenario to an *Equal* scenario.

Effects of structural damping

Adding damping to the structural system decreases the feedback it exerts back onto the hydraulic system. Let us consider again the case of a 20 Hz input, and analyze the system with two different levels of friction damping, defined by expression (2.57), considering embedded length ratios of $\varrho = 0.2$ and $\varrho = 0.8$, corresponding to the percentage of the pile exposed to soil friction.

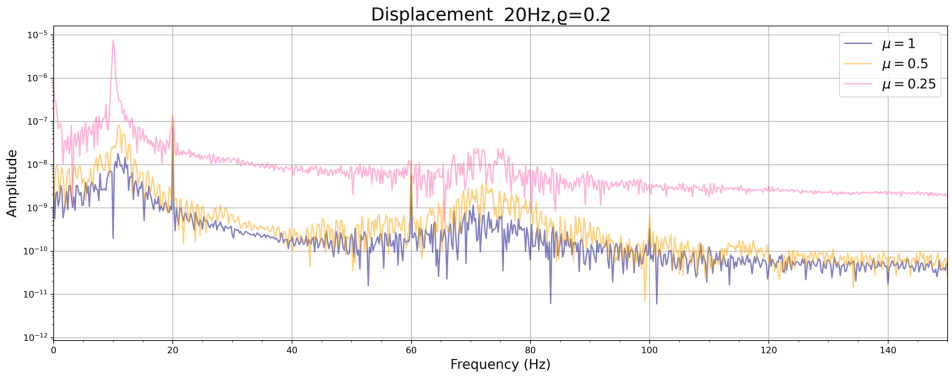

(a) $\varrho = 0.2$

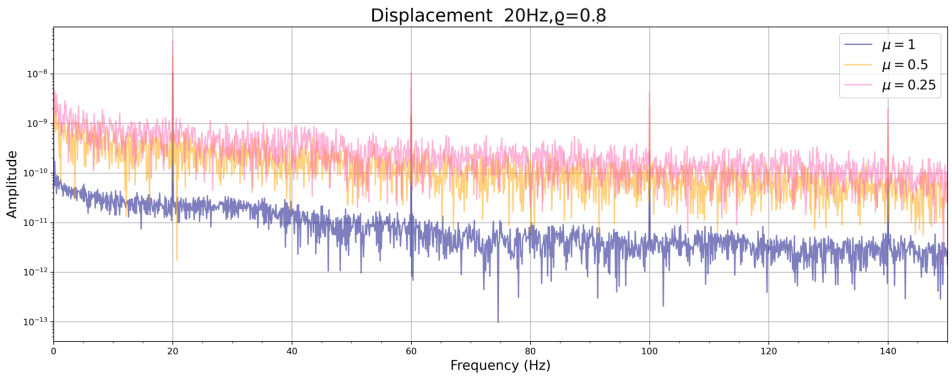

(b) $\varrho = 0.8$

Figure 4.23: Effect of damping ratio in dynamic regime

Increasing the damping in the structure is effective in transitioning the system from a *Weak-Strong* scenario to an *Equal* one, as shown in the previous figure. Notably, this transition out of the *Weak-Strong* configuration is possible even at very low mass ratios, although the response remains strongly influenced by the first mode of the structure.

Similarly, further increasing the damping can transition the system into the *Strong-Weak* regime, where the response depends almost exclusively on the power-hydraulic subsystem as it is shown in Figure 4.23

4.2.2. Control of MDOF System

The control strategy utilized for the system corresponding to the MDOF structure rigidly coupled to the piston of a Power-Hydraulic system is identical to that used in the SDOF cases.

Although the strategy remains the same, several differences arise, primarily in three aspects:

1. **Controllability is not possible in all scenarios**
   Among the various scenarios and dynamic behaviors that the coupled system can exhibit, the case corresponding to the *Weak-Strong* configuration cannot be effectively controlled using the implemented scheme. This is due to the dynamics of the structure dominating the response, which causes the actuator pressure to follow the motion of the structure.

   As a result, the pressure becomes decoupled from the valve, and subsequently limiting the pressure transfer (by mean of a flow rate) to the actuator. Without a sufficient pressure gradient, there is no effective flow through the actuator, and therefore, no *control authority* over the displacement, phenomena shown in figure 4.24

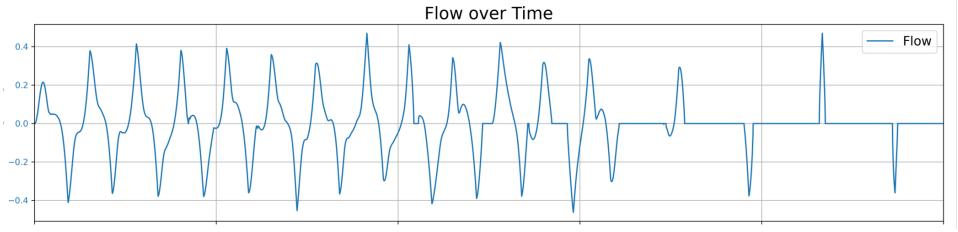

Figure 4.24: Flow response for *Weak-Strong* system

2. **Multimodal Response**
   Given the coupling configuration, the first mode is primarily excited. However, depending on the spacing and frequency of higher modes, these could potentially interact with either the super-harmonics of the input excitation or the oil-column resonance frequencies. This increases the number of frequencies at which the system can exhibit a meaningful dynamic response could increase the required control complexity, due to highly nonlinear dynamics. However, for the purposes of our structure, although evident, the higher harmonic of the beam do not meaningfully interact with other dynamic effects.
3. **Linear Structure**
   Although the structure responds at multiple frequencies, it behaves linearly. Thus, the assumption that the primary source of nonlinearity arises from flow through the servo-valve remains valid. Consequently, the control scheme requires no significant modifications for application to multi-degree-of-freedom (MDOF) systems.

Therefore, the focus is placed on controlling non-lightly damped ($\xi_{eq}^{\omega_1} > 5$) systems at resonance, in this situation the implemented control scheme demonstrates successful displacement control, as illustrated in Figure

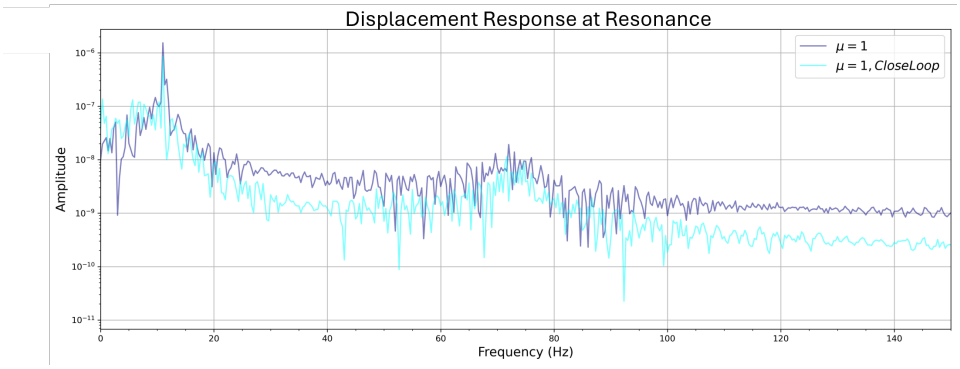

(a) Close Loop Response:$\mu = 1$

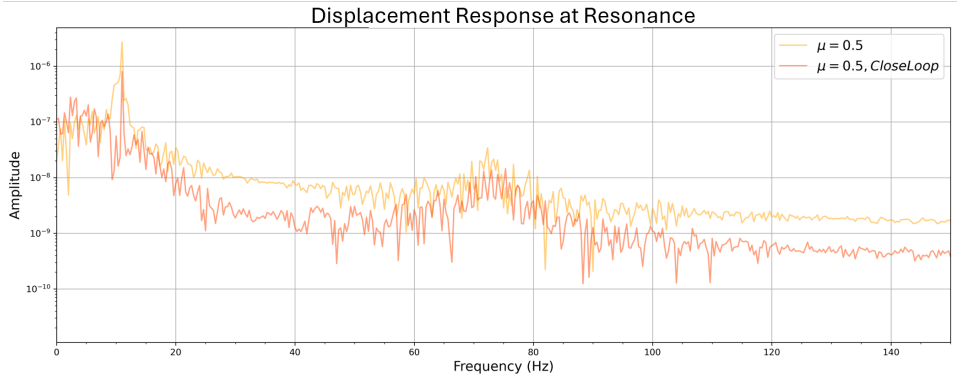

(b) Close Loop Response :$\mu = 0.5$

Figure 4.25: Close Loop at $\varrho = 0.2$

As shown in the previous figure, when exciting the system at its first natural frequency, the response is primarily at the same frequency. Therefore, the demands on the control system are minimal. Additionally, given the characteristics of the considered system, the structural response at higher modes always excites the first mode, which, due to its coupling with the hydraulic system through a velocity coupling, inherently reduces the response at higher modes.

For lower mass ratios, the effect of the control system are clearer, reducing the frequency content across most of the spectrum, yet unable to fully suppress the response at the second mode, which again, although measurable, it is minor in comparison with the main harmonic.

When the structure encounters high dissipative forces, as is the case with soil damping ($30\% < \xi_{eq}^{\omega_1} < \varrho = 0.8$), the system's response behaves similarly to that of a single-degree-of-freedom (SDOF) system, and the conclusions and extensive analysis done for that case apply.

A clear example is considering the response of the system with $\varrho = 0.8$ at $F = 30$ Hz.

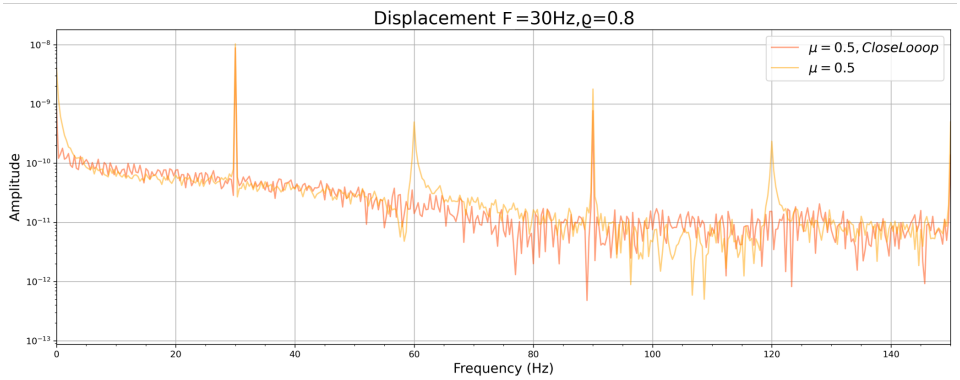

Figure 4.26: Displacement control with high damping

In Figure 4.26, it is evident that when exciting the system with high damping, the response is primarily at the voltage (input) frequency and their corresponding super-harmonics. Therefore, the control systems can successfully suppress the higher harmonics, similar to the behavior observed in the SDOF case.

5

Conclusion

This thesis investigates the modeling and control of a power-hydraulic system rigidly coupled to a flexible structure. A nonlinear model was developed that integrates electrical, hydraulic, and structural subsystems, explicitly taking into account actuator dynamics. Unlike common approaches that assume decoupling between power-hydraulic and structure subsystems, this work accounts for the velocity-pressure coupling, and nonlinear flow by means of a fully integrated modeling framework.

A parametric study varying the normalized supply pressure (αP_{max}) was conducted to determine the minimum hydraulic power and system size required for effective controllability, particularly for sinusoidal displacement control in both SDOF and MDOF structures.

Despite multiple nonlinearities, nonlinear flow behavior was identified as the dominant factor influencing system dynamics. The implemented PID-based controller effectively mitigated these effects. In particular, the control systems achieved sinusoidal displacement control across a wide range of excitation frequencies and supply pressures, successfully operating at only 25% of the original supply pressure.

Additionally, it was found that in weakly damped systems, and at low mass ratios, the hydraulic system can experience forced-synchronization. This can induce pressure transients that can be detrimental to the system and potentially invalidate the controller's ability to command the structure effectively. Conversely, in highly damped systems, the influence of the internal dynamics of the structure play a minimal role in the overall system dynamics. Under this assumption, the structural system can be approximated by a SDOF system.

Although careful consideration was given to selecting a representative system and implementing a control strategy that is practical and readily deployable, experimental validation remains essential to confirm its performance. In particular, the robustness of the control system needs to be fully evaluated, considering the uncertainties associated with soil conditions and modeling assumptions that a pile when driving experiences

Furthermore, it is expected that the control system's performance will degrade when coupled with a nonlinear structure, as the control is not fully effective in suppressing higher and pressure super-harmonics simultaneously. Consequently, the controllability in the presence of different nonlinear structures must be investigated.

This work contributes to the development of a minimal, PID-based controllers suitable for industrial implementation in structure–power-hydraulic systems. It is particularly relevant to offshore applications such as GDP (Gentle Driving of Pile), where coupling effects arise during vibratory pile driving. As offshore technologies progress toward more compact and power-efficient designs, this thesis supports the development of control strategies that maintain performance despite strong coupling and nonlinear dynamics. The approach prioritizes simplicity, minimal hardware, and straightforward implementation, key considerations for successful deployment in challenging offshore environments.

References

[1] Giacomo Di Foggia and Massimo Beccarello. “European roadmaps to achieving 2030 renewable energy targets”. In: *Utilities Policy* 88 (2024), p. 101729. ISSN: 0957-1787. DOI: https://doi.org/10.1016/j.jup.2024.101729. URL: https://www.sciencedirect.com/science/article/pii/S0957178724000225.

[2] European Commission. *Action Plan for Grids. COM/2023/669 final*. European Commission Communication. Nov. 2023. URL: https://eur-lex.europa.eu/legal-content/EN/TXT/?uri=CELEX:52023DC0669.

[3] Vicente Negro et al. “Monopiles in offshore wind: Preliminary estimate of main dimensions”. In: *Ocean Engineering* 133 (2017), pp. 253–261. ISSN: 0029-8018. DOI: https://doi.org/10.1016/j.oceaneng.2017.02.011. URL: https://www.sciencedirect.com/science/article/pii/S0029801817300690.

[4] Yaohua Guo, Haijun Wang, and Jijian Lian. “Review of integrated installation technologies for offshore wind turbines: Current progress and future development trends”. In: *Energy Conversion and Management* 255 (2022). DOI: 10.1016/j.enconman.2022.115319.

[5] European Wind Energy Association. *The European Offshore Wind Industry – Key Trends and Statistics*. Accessed July 2025. Jan. 2014. URL: https://www.ewea.org/fileadmin/files/library/publications/statistics/EWEA-European-Offshore-Statistics-2013.pdf.

[6] K. Vázquez, R.R. Rodríguez, and M.D. Esteban. “Inventory proposal for monopiles in offshore wind farms”. In: *Ocean Engineering* 247 (2022), p. 110741. ISSN: 0029-8018. DOI: https://doi.org/10.1016/j.oceaneng.2022.110741. URL: https://www.sciencedirect.com/science/article/pii/S0029801822001925.

[7] Chuan Ma, James Ban, and Goangseup Zi. “Comparative study on the dynamic responses of monopile and jacket-supported offshore wind turbines considering the pile-soil interaction in transitional waters”. In: *Ocean Engineering* 292 (2024), p. 116564. ISSN: 0029-8018. DOI: https://doi.org/10.1016/j.oceaneng.2023.116564. URL: https://www.sciencedirect.com/science/article/pii/S0029801823029487.

[8] Mehmet Bilgili and Hakan Alphan. “Global growth in offshore wind turbine technology”. In: *Clean Technologies and Environmental Policy* 24.7 (2022), pp. 2215–2227. ISSN: 1618-9558. DOI: 10.1007/s10098-022-02314-0. URL: https://doi.org/10.1007/s10098-022-02314-0.

[9] Apostolos Tsouvalas. “Underwater Noise Emission Due to Offshore Pile Installation: A Review”. In: *Energies* 13.12 (2020). DOI: 10.3390/en13123037. URL: https://www.mdpi.com/1996-1073/13/12/3037.

[10] Helen Bailey et al. “Assessing underwater noise levels during pile-driving at an offshore windfarm and its potential effects on marine mammals”. In: *Marine Pollution Bulletin* 60.6 (2010), pp. 888–897. ISSN: 0025-326X. DOI: https://doi.org/10.1016/j.marpolbul.2010.01.003. URL: https://www.sciencedirect.com/science/article/pii/S0025326X10000044.

[11] Ryunosuke Kikuchi. “Risk formulation for the sonic effects of offshore wind farms on fish in the EU region”. In: *Marine Pollution Bulletin* 60.2 (2010), pp. 172–177. ISSN: 0025-326X. DOI: https://doi.org/10.1016/j.marpolbul.2009.09.023. URL: https://www.sciencedirect.com/science/article/pii/S0025326X09004056.

[12] A. Tsouvalas and A.V. Metrikine. “Noise reduction by the application of an air-bubble curtain in offshore pile driving”. In: *Journal of Sound and Vibration* 371 (2016), pp. 150–170. ISSN: 0022-460X. DOI: https://doi.org/10.1016/j.jsv.2016.02.025. URL: https://www.sciencedirect.com/science/article/pii/S0022460X16001681.

[13] Sven Koschinski and Karin Lüdemann. *Development of Noise Mitigation Measures in Offshore Wind Farm Construction*. Tech. rep. Original report published in German (July 2011), updated February 2013. Federal Agency for Nature Conservation (Bundesamt für Naturschutz, BfN), 2013. URL: https://www.bfn.de/sites/default/files/BfN/service/Dokumente/skripten/skript362.pdf.

[14] Peter H. Dahl, David R. Dall'Osto, and Donald M. Farrell. "The underwater sound field from vibratory pile driving". In: *The Journal of the Acoustical Society of America* 137.6 (June 2015), pp. 3544–3554. DOI: 10.1121/1.4921288.

[15] T. Molenkamp and A. Tsouvalas. "Underwater Noise from Gentle Driving of Piles". In: *Proceedings of the 30th International Congress on Sound and Vibration*. Ed. by W. van Keulen and J. Kok. Proceedings of the International Congress on Sound and Vibration. Article 682. Society of Acoustics, 2024. URL: https://iiav.org/content/archives_icsv_last/2024_icsv30/content/papers/papers/full_paper_682_20240327130517459.pdf.

[16] P. Staubach et al. "Vibratory pile driving in water-saturated sand: Back-analysis of model tests using a hydro-mechanically coupled CEL method". In: *Soils and Foundations* 61.1 (2021), pp. 144–159. ISSN: 0038-0806. DOI: https://doi.org/10.1016/j.sandf.2020.11.005. URL: https://www.sciencedirect.com/science/article/pii/S0038080620337586.

[17] Amir M. Kaynia et al. "Numerical model for dynamic installation of large diameter monopiles". In: *Soil Dynamics and Earthquake Engineering* 161 (2022), p. 107393. ISSN: 0267-7261. DOI: https://doi.org/10.1016/j.soildyn.2022.107393. URL: https://www.sciencedirect.com/science/article/pii/S0267726122002421.

[18] Nicolás Moscoso del Prado Mazza and Alain E. Holeyman. "Frequency-Penetration Response Spectrum on Vibratory Amplitude Matching of Monopiles". In: *10th International Conference on Stress Wave Theory and Testing Methods for Deep Foundations*. ASTM International, July 2019. ISBN: 978-0-8031-7667-6.

[19] Andrei Metrikine et al. "GDP: A New Technology for Gentle Driving of (Mono)Piles". In: Aug. 2020.

[20] Finn B Jensen et al. *Computational ocean acoustics*. Vol. 2011. Springer, 2011.

[21] Athanasios Tsetas, Apostolos Tsouvalas, and Andrei V. Metrikine. "The mechanics of the Gentle Driving of Piles". In: *International Journal of Solids and Structures* 282 (2023), p. 112466. ISSN: 0020-7683. DOI: https://doi.org/10.1016/j.ijsolstr.2023.112466. URL: https://www.sciencedirect.com/science/article/pii/S0020768323003633.

[22] Athanasios Tsetas et al. "Gentle Driving of Piles (GDP) at a sandy site combining axial and torsional vibrations: Part I - installation tests". In: *Ocean Engineering* 270 (2023), p. 113453. ISSN: 0029-8018. DOI: https://doi.org/10.1016/j.oceaneng.2022.113453. URL: https://www.sciencedirect.com/science/article/pii/S0029801822027366.

[23] Evangelos Kementzetzidis et al. "Gentle Driving of Piles (GDP) at a sandy site combining axial and torsional vibrations: Part II - cyclic/dynamic lateral loading tests". In: *Ocean Engineering* 270 (2023), p. 113452. ISSN: 0029-8018. DOI: https://doi.org/10.1016/j.oceaneng.2022.113452. URL: https://www.sciencedirect.com/science/article/pii/S0029801822027354.

[24] Valerie Whenham and Alain Holeyman. "Load Transfers During Vibratory Driving". In: *Geotechnical and Geological Engineering* 30.5 (2012), pp. 1119–1135. DOI: 10.1007/s10706-012-9527-0. URL: https://doi.org/10.1007/s10706-012-9527-0.

[25] Sergio S. Gómez et al. "Experimental investigation of frequency–amplitude decoupling in axial-torsional vibratory pile driving by means of laboratory-scale testing". In: *Ocean Engineering* 316 (2025), p. 119788. ISSN: 0029-8018. DOI: https://doi.org/10.1016/j.oceaneng.2024.119788. URL: https://www.sciencedirect.com/science/article/pii/S0029801824031263.

[26] *SciPy Documentation: scipy.integrate.solve_ivp*. https://docs.scipy.org/doc/scipy/reference/generated/scipy.integrate.solve_ivp.html.

[27] James W. Cooley and John W. Tukey. "An Algorithm for the Machine Calculation of Complex Fourier Series". In: *Mathematics of Computation* 19.90 (1965), pp. 297–301. DOI: 10.2307/2003354.

[28] Noah D Manring and Roger C Fales. *Hydraulic control systems*. John Wiley & Sons, 2019.

[29] James A. Cripe Herbert H. Tackett and Gary Dyson. *Positive Displacement Reciprocating Pump Fundamentals—Power and Direct Acting Types*. Tech. rep. College Station, Texas: Texas A&M University, Turbomachinery Laboratories, 2008.

[30] Ryszard Dindorf, Jakub Takosoglu, and Piotr Wos. "Review of Hydro-Pneumatic Accumulator Models for the Study of the Energy Efficiency of Hydraulic Systems". In: *Energies* 16.18 (2023). ISSN: 1996-1073. DOI: 10.3390/en16186472. URL: https://www.mdpi.com/1996-1073/16/18/6472.

[31] R. Amirante, P.G. Moscatelli, and L.A. Catalano. "Evaluation of the flow forces on a direct (single stage) proportional valve by means of a computational fluid dynamic analysis". In: *Energy Conversion and Management* 48.3 (2007), pp. 942–953. ISSN: 0196-8904. DOI: https://doi.org/10.1016/j.enconman.2006.08.024. URL: https://www.sciencedirect.com/science/article/pii/S0196890406002949.

[32] Philip M Gerhart, Andrew L Gerhart, and John I Hochstein. *Munson, Young and Okiishi's fundamentals of fluid mechanics*. John Wiley & Sons, 2016.

[33] Philip L. Skousen. *Control Valve Handbook*. 6th. St. Louis, MO: Emerson Process Management, 2016.

[34] Domin Fluid Power Ltd. *Domin Valves — Product Specifications*. https://domin.com/products/valves/. Accessed 12 June 2025. 2025.

[35] J. P. Conte and T. L. Trombetti. "Linear dynamic modeling of a uni-axial servo-hydraulic shaking table system". In: *Earthquake Engineering & Structural Dynamics* 29.9 (2000), pp. 1375–1404. DOI: 10.1002/1096-9845(200009)29:9<1375::AID-EQE975>3.0.CO;2-3. URL: https://doi.org/10.1002/1096-9845(200009)29:9%3C1375::AID-EQE975%3E3.0.CO;2-3.

[36] Martin Inderelst and Hubertus Murrenhoff. *Hydraulic Proportional and Servo Valves*. Ed. by Richard L. Shubkin. Springer, 2014.

[37] Paolo Tamburrano et al. "A Review of Direct Drive Proportional Electrohydraulic Spool Valves: Industrial State-of-the-Art and Research Advancements". In: *Journal of Dynamic Systems, Measurement, and Control* 141.2 (Oct. 2018), p. 020801. DOI: 10.1115/1.4041063.

[38] Jack L. Johnson. *What's the Difference Between a Servo Valve and a Proportional Valve?* Apr. 2024. URL: https://www.powermotiontech.com/hydraulics/hydraulic-valves/article/21882788/whats-the-difference-between-a-servo-valve-and-a-proportional-valve.

[39] G. K. Nikas. *Eighty years of research on hydraulic reciprocating seals: Review of tribological studies and related topics since the 1930s*. Accessed 3 September 2025. 2010. DOI: 10.1243/13506501JET607. URL: https://doi.org/10.1243/13506501JET607.

[40] Narutoshi Nakata and Erin Krug. "Computational framework for effective force testing and a compensation technique for nonlinear actuator dynamics". In: *Journal/Conference Name (if known)* (). Department of Civil Engineering, Johns Hopkins University, Baltimore, MD, USA.

[41] Yutaka Tanaka, Sayako Sakama, and Ryushi Suzuki. "Bubble Elimination from Working Oil for Environmentally Friendly Hydraulic System Design". In: *International Journal of Fluid Power Systems* (2012). Technical paper, Hosei University and Opus System Inc.

[42] J. Ruan and R. Burton. "Bulk Modulus of Air Content Oil in a Hydraulic Cylinder". In: *Proceedings of the ASME 2006 International Mechanical Engineering Congress and Exposition*. Fluid Power Systems and Technology, November 5–10, 2006. Chicago, Illinois, USA: ASME, 2006, pp. 259–269. DOI: 10.1115/IMECE2006-14914. URL: https://asmedigitalcollection.asme.org/IMECE/proceedings-abstract/IMECE2006/47713/259/320685.

[43] Hossein Gholizadeh. "Modeling and Experimental Evaluation of the Effective Bulk Modulus for a Mixture of Hydraulic Oil and Air". Doctor of Philosophy in Mechanical Engineering. PhD Thesis. Saskatoon, Canada: University of Saskatchewan, 2014. URL: https://www.collectionscanada.gc.ca/obj/thesescanada/vol2/002/MQ42907.pdf.

[44] C. A. F. de Jong. "Analysis of pulsations and vibrations in fluid-filled pipe systems". PhD Thesis. Technische Universiteit Eindhoven, 1994. URL: https://doi.org/10.6100/IR42364.

[45] Jan Łuczko and Andrzej Czerwiński. “Parametric vibrations of flexible hoses excited by a pulsating fluid flow, Part I: Modelling, solution method and simulation”. In: *Journal of Fluids and Structures* 55 (2015), pp. 155–173. ISSN: 0889-9746. DOI: https://doi.org/10.1016/j.jfluidstructs.2015.02.011. URL: https://www.sciencedirect.com/science/article/pii/S0889974615000547.

[46] Charles K. Alexander and Matthew N.O. Sadiku. *Fundamentals of Electric Circuits*. 6th. New York, NY: McGraw-Hill Education, 2016.

[47] D. C. Karnopp, D. L. Margolis, and R. C. Rosenberg. *System Dynamics: Modeling, Simulation, and Control of Mechatronic Systems*. 5th ed. Wiley, 2012.

[48] Anil K. Chopra. *Dynamics of Structures: Theory and Applications to Earthquake Engineering*. 4th. Upper Saddle River, NJ: Prentice Hall, 2012. ISBN: 978-0132858034.

[49] Kenneth G. Gavin and Brendan C. O’Kelly. “Effect of friction fatigue on pile capacity in dense sand”. In: *Journal of Geotechnical and Geoenvironmental Engineering* 133.1 (2007), pp. 63–71. DOI: 10.1061/(ASCE)1090-0241(2007)133:1(63).

[50] D. J. White and B. M. Lehane. “Friction fatigue on displacement piles in sand”. In: *Géotechnique* 54.10 (2004), pp. 645–658. DOI: 10.1680/geot.2004.54.10.645.

[51] Alán Tapia, Miguel Bernal, and Leonid Fridman. “Nonlinear sliding mode control design: An LMI approach”. In: *Systems Control Letters* 104 (2017), pp. 38–44. ISSN: 0167-6911. DOI: https://doi.org/10.1016/j.sysconle.2017.03.011. URL: https://www.sciencedirect.com/science/article/pii/S0167691117300646.

[52] M. B. D. Mohd, M. H. M. Hossain, and M. R. M. Zain. “Nonlinear Control of Hydraulic Systems: A Survey of Methods and Applications”. In: *Journal of Dynamic Systems, Measurement, and Control* 140.6 (2020). DOI: 10.1115/1.4048021. URL: https://asmedigitalcollection.asme.org/dynamicsystems/article/140/6/060801/1048152.

[53] Karl J. Åström and Tore Hägglund. *Advanced PID Control*. Research Triangle Park, NC: ISA - The Instrumentation, Systems, and Automation Society, 2006. ISBN: 978-1-55617-942-6.

[54] Gene F. Franklin, J. David Powell, and Abbas Emami-Naeini. *Feedback Control of Dynamic Systems*. 8th. Pearson, 2018. ISBN: 9780134685717.

[55] Dan Simon. *Optimal State Estimation: Kalman, H∞, and Nonlinear Approaches*. 1st. Hoboken, NJ: John Wiley & Sons, 2006. ISBN: 978-0-471-72132-5.

[56] Eric A. Wan and Rudolph van der Merwe. *The Unscented Kalman Filter for Nonlinear Estimation*. Tech. rep. Beaverton, Oregon, USA: Oregon Graduate Institute of Science & Technology, 2000.

[57] Dean H. Kim and Tsu-Chin Tsao. “A Linearized Electrohydraulic Servovalve Model for Valve Dynamics Sensitivity Analysis and Control System Design”. In: *Journal of Dynamic Systems, Measurement, and Control* ().

[58] James C. Akers, Michael T. Hale, and Joel W. Sills Jr. “Challenges and Considerations When Using Hydraulic Modal Shaking in Large-Scale Modal Testing”. In: *Advances in Modal Analysis and Testing*. Ed. by John Doe and Jane Smith. Springer, 2023, pp. 123–145. DOI: 10.1007/978-3-031-05415-0_13.

[59] Wenzhong Gao. “Modeling and control of nonlinear systems with deadzone and backlash”. In: *Automatica* 32.5 (1996), pp. 755–762.

[60] Giacomo Galuppini, Lalo Magni, and Davide Martino Raimondo. “Model predictive control of systems with deadzone and saturation”. In: *Control Engineering Practice* 78 (2018), pp. 56–64. ISSN: 0967-0661. DOI: https://doi.org/10.1016/j.conengprac.2018.06.010. URL: https://www.sciencedirect.com/science/article/pii/S0967066118301710.

[61] Jozef Vörös. “Modeling and identification of systems with backlash”. In: *Automatica* 46.2 (2010), pp. 369–374. ISSN: 0005-1098. DOI: https://doi.org/10.1016/j.automatica.2009.11.005. URL: https://www.sciencedirect.com/science/article/pii/S0005109809005299.

[62] Brian Armstrong-Hélouvry, Pierre Dupont, and Carlos Canudas De Wit. “A survey of models, analysis tools and compensation methods for the control of machines with friction”. In: *Automatica* 30.7 (1994), pp. 1083–1138. ISSN: 0005-1098. DOI: https://doi.org/10.1016/0005-1098(94)90209-7. URL: https://www.sciencedirect.com/science/article/pii/0005109894902097.

[63] Cross Hydraulics Pty. Ltd. *Electronic Devices – Electronics Manual (Revision 0.4)*. Cross Hydraulics Pty. Ltd. Aug. 2021. URL: https://www.crosshydraulics.com.au/wp-content/uploads/2021/08/Electronics-Manual-Rev-04.pdf.

[64] Klaudiusz Klarecki, Dominik Rabsztyn, and Mariusz Piotr Hetmańczyk. "Multi-criteria optimization of the dither current intensity in the case of proportional valve". In: *Journal of Vibroengineering* 17.5 (2015), pp. 2611–2621. DOI: 10.21595/jve.2015.15393. URL: https://www.extrica.com/article/15393.

[65] F. H. Hsiao and J. D. Hwang. "Optimal Controller for Dithered Systems with Backlash or Hysteresis". In: *Journal of Optimization Theory and Applications* 94.1 (July 1997), pp. 87–113. ISSN: 1573-2878. DOI: 10.1023/A:1022607619198. URL: https://doi.org/10.1023/A:1022607619198.

[66] R.S.O. Dias, M. Martarelli, and P. Chiariotti. "On the use of Lagrange Multiplier State-Space Substructuring in dynamic substructuring analysis". In: *Mechanical Systems and Signal Processing* 180 (2022), p. 109419. ISSN: 0888-3270. DOI: https://doi.org/10.1016/j.ymssp.2022.109419. URL: https://www.sciencedirect.com/science/article/pii/S0888327022005416.

[67] K. E. Brenan, S. L. Campbell, and L. R. Petzold. *Numerical Solution of Initial-Value Problems in Differential-Algebraic Equations*. Society for Industrial and Applied Mathematics (SIAM), 1996.

[68] R. E. Skelton. *Dynamic Systems Control*. New York: John Wiley & Sons, 1997. ISBN: 978-0-471-14595-4.

[69] *NI 9202 Analog Input Module Datasheet*. https://www.ni.com/en-us/support/documentation/supplemental/06/ni-9202-analog-input-module.html.

[70] *Measuring Vibration with Accelerometers — ni.com*. https://www.ni.com/en/shop/data-acquisition/sensor-fundamentals/measuring-vibration-with-accelerometers.html.

[71] Dan Simon. *Optimal State Estimation: Kalman, H Infinity, and Nonlinear Approaches*. John Wiley & Sons, 2006. ISBN: 9780471708582.

[72] Katsuhiko Ogata. *Modern Control Engineering*. 5th. Upper Saddle River, NJ: Prentice Hall, 2010. ISBN: 0136156738.